Transparent Graphene Neural Electrodes and Field-Effect Transistors for Bio Applications

by

Dong-Wook Park

A dissertation submitted in partial fulfillment of

the requirements for the degree of

Doctor of Philosophy

(Electrical and Computer Engineering)

at the

University of Wisconsin-Madison

2016

Date of final oral examination: 07/13/2016

The dissertation is approved by the following members of the Final Oral Committee:

Zhenqiang (Jack) Ma, Professor, Electrical and Computer Engineering

Justin C. Williams, Professor, Biomedical Engineering

Mikhail Kats, Assistant Professor, Electrical and Computer Engineering

Zongfu Yu, Assistant Professor, Electrical and Computer Engineering

M. Elizabeth Meyerand, Professor, Biomedical Engineering and Medical Physics

To Selim

Acknowledgements

It has been a wonderful journey the last five years at the University of Wisconsin-Madison. First of all, I would like to thank my advisor Professor Zhenqiang Ma for his support and advice. His passion for research and active endeavor inspired me to pursue innovative research. I also thank Professor Justin Williams for his insightful perspective and guidance. The lessons from Prof. Ma and Prof. Williams are invaluable for my future career and life. I would like to thank my committee members, Professor Mikhail Kats, Professor Zongfu Yu, and Professor Elizabeth Meyerand for meaningful questions and discussion. I hope I can have opportunities in the future to further discuss interesting research directions with them. I was also able to learn and perform a variety of interesting research topics with my collaborators. I thank Prof. Bijan Pesaran (New York University), Prof. John Hetling (Univ. of Illinois-Chicago), Prof. Ramin Pashaie (Univ. of Wisconsin-Milwaukee), Prof. Jonathan Viventi (Duke University), Prof. Kendall Lee (Mayo Clinic), Dr. Kip Ludwig (Mayo Clinic), Prof. David Schwartz (Univ. of Wisconsin-Madison), and Prof. Jeremy Levy (Univ. of Pittsburgh) for the collaboration opportunities.

Special thanks to my colleagues and friends in my research group: Hyungsoo Kim, Jihye Bong, Yei Hwan Jung, Dr. Dong Liu, Dr. Tzu-Hsuan Chang, Dr. Jaeseong Lee, Sang June Cho, Namki Cho, Firat Yasar, Tong June Kim, Kwangeun Kim, Huilong Zhang, Zhenyang Xia, Juhwan Lee, Jae Ha Ryu, Jeongpil Park, Jisoo Kim, Dr. Jung-hun Seo, Dr. Munho Kim, Dr. Solomon Mikael, Dr. Minkyu Cho, Dr. Hongyi Mi, and Dr. Gui Gui. Luckily I was also able to have wonderful colleagues in Prof. Williams' lab: Sarah Brodnick, Jared Ness, Joey Novello, Dr. Lisa Krugner-Higby, Dr. Corinne Esquibel, Dr. Dong-Hyun Baek, Dr. Kyle Swanson, Dr. Aaron Dingle, Dr. Abhishek Bhat, Kevin Cheng, Dr. Amelia Sandburg, Dr. Thomas Richner, and Dr. Sanitta Thongpang. I would like to express my gratitude to the Wisconsin Center for

Applied Microelectronics staff for their help.

Finally, I would like to thank my family and friends for their unconditional support and love. My mother has always on my side and she has been my inspiration for my achievements. I am sure my father in heaven will be proud of me. My sister, brother-in-law, niece and nephew have been my source of happiness. My dearest wife Selim and my son Jay are the reason of my existence. I appreciate Selim's support, understanding, and love.

I thank the following funding agencies for their financial support: ONR, NIH, DARPA and ARO.

TABLE OF CONTENTS

Abstracts

Graphene, a novel material made of carbon atoms, has broad wavelength transparency from ultraviolet (UV) to infrared (IR). In addition, the electrical conductivity, mechanical flexibility, and biocompatibility of graphene make it a promising material for next-generation biomedical devices and biosensors. Among various applications of graphene, transparent graphene neural electrodes and graphene field-effect transistors have been studied.

A transparent, flexible, and implantable graphene neural electrode array (or simply graphene brain sensor) that is capable of advanced *in vivo* neural imaging, electrophysiological recordings, optogenetics, and electrical stimulation has been demonstrated. Previous *in vivo* studies with conventional metal-based electrodes were limited to monitoring the tissue surrounding the electrode sites due to the opaqueness of the metal. Optical stimuli through the electrode sites and traces were also impossible with metal electrodes. The transparent graphene brain sensor implanted over the cerebral cortex in laboratory rodents allowed for chronic investigation of the underlying neural tissue while simultaneously performing electrophysiology. *In vivo* imaging of the cortical vasculature through the transparent brain sensor has been shown via fluorescence microscopy and 3D optical coherence tomography. Optogenetic activation of focal cortical areas directly beneath the electrode sites has been demonstrated in transgenic Thy1::ChR2 mice. The graphene remains electrically viable for chronic recording for extended time periods (up to 70 days). In order to understand the working mechanism of the graphene electrodes and to expand their utility, the electrochemical impedance of the graphene electrode arrays and their demonstration to the electrical stimulation in GCaMP6 mice have been studied.

In addition, graphene field-effect transistors (FETs) with a bottom-gate structure either

on a rigid or flexible substrate (Parylene C) have been demonstrated. First, for the purpose of minimizing process-induced mobility degradation of graphene, graphene radio frequency (RF) transistors with buried bottom gates have been fabricated and characterized. In this process, graphene is transferred to the top of finished gates and source/drains near the end of the entire fabrication process. The graphene RF transistor with a channel length of 600 nm shows a maximum oscillation frequency (f_{max}) of 13 GHz and a cut-off frequency (f_T) of 2 GHz after de-embedding. Also, a method to improve the graphene adhesion on atomic layer deposition (ALD) Al_2O_3 has been reported. Second, the fabrication, characterization, and performance improvement of flexible bottom-gate graphene transistors on Parylene C have been discussed. The low-temperature fabrication process and the performance improvement using a current annealing method could be utilized in other two-dimensional (2D) material-based electronics. For all of the graphene FETs introduced here, the graphene transferred on top of the devices could be used as a bio sensing material. This study demonstrates an array of abilities of graphene neural electrodes and graphene FETs.

List of figures

Chapter	Adapted / taken from papers
Chapter 1	Manuscript in preparation: "Review of micro-electrocorticography"
Chapter 2	"Graphene-based carbon-layered electrode array technology for neural imaging and optogenetic applications," D.-W. Park, A. A. Schendel, S. Mikael, S. K. Brodnick, T. J. Richner, J. P. Ness, M. R. Hayat, F. Atry, S. T. Frye, R. Pashaie, S. Thongpang, Z. Ma, and J. C. Williams, *Nature Communications*, 5, 6258, October 2014. "Fabrication and utility of a transparent graphene neural electrode array for electrophysiology, in vivo imaging, and optogenetics," D.-W. Park, S. K. Brodnick, J. P. Ness, L. Krugner-Higby, A. Sandberg, S. Mikael, T. J. Richner, J. Novello, H. Kim, D.-H. Baek, F. Atry, S. T. Frye, R. Pashaie, S. Thongpang, J. C. Williams, and Z. Ma, *Nature Protocols*, In press.
Chapter 3	"Evaluation of transparent graphene electrode array and its usage to electrical stimulation in GCaMP6f mice," D.-W. Park, S. K Brodnick, J. P Ness, C. Esquibel, D.-H. Baek, F. Atry, H. Kim, J. Bong, K. I Swanson, R. Pashaie, Z. Ma, J. C Williams, in preparation for *Journal of Neural Engineering* submission.
Chapter 4	"Transparent graphene contact lens electrode array for early diagnosis of eye disease," D.-W. Park, Z. H. Derafshi, H. Kim, D.-H. Baek, S. K. Brodnick, J. P. Ness, J. Novello, A. Sandberg, S. Mikael, S. Thongpang, J. C. Williams, J. R. Hetling, Z. Ma, in preparation for *Advanced Materials* submission.
Chapter 5	"Bottom-gate coplanar graphene transistors with enhanced graphene adhesion on atomic layer deposition Al_2O_3," D.-W. Park, S. Mikael, T.-H. Chang, S. Gong, and Z. Ma, *Applied Physics Letter*, Vol. 106, pp. 102106, March 2015. "Graphene RF transistors with buried bottom gate," D.-W. Park, T.-H. Chang, S. Mikael, J.-H. Seo, P.F. Nealey and Z. Ma, 13th Topical Meeting on Silicon Monolithic Integrated Circuits in RF Systems (SiRF'13), Austin, TX, USA, January 21-23, 2013.
Chapter 6	"Flexible bottom-gate graphene transistors on Parylene C substrate and its current annealing effect," D.-W. Park, H. Kim, J. Bong, S. Mikael, T. J. Kim, J. C. Williams and Z. Ma, under review in *Applied Physics Letter*.

Chapter 1. Introduction

1.1 Graphene material characteristics and applications

Graphene which was coined as a combination of graphite and the affix –ene has attracted researchers for its superior properties such as giant intrinsic mobility, high current densities, high thermal conductivity, transparency, and the thinnest but strongest nature[1-7]. These characteristics have been considered promising properties for next-generation electronics such as graphene electrodes and graphene transistors. In addition, graphene's biocompatibility, biostability, and large surface-to-volume ratio have drawn much attention from biological science and engineering fields[8-12]. These stunning merits of graphene have led to the rapidly increasing exploration of electronic devices and circuits, as well as various biomedical devices and biosensors, using graphene.

Figure 1.1 shows the representative characteristics of graphene. Graphene consists of mono-layer carbon atoms arranged in a two-dimensional (2D) honeycomb array. The atoms are about 1.42 Å apart in the same plane and tightly bound by sp^2 hybridization[13]. The distance between two graphene monolayers (similar to thickness in bulk materials) is about 3.35 Å. Monolayer graphene absorbs about 2.3-2.6% of light, giving a transmittance of about 97.4%[5]. The maximum intrinsic room temperature mobility is 200,000 cm^2/Vs, but on SiO_2 substrate the limit mobility is 40,000 cm^2/Vs[14]. Graphene has the lowest resistivity of all known materials at room temperature of 10^{-6} Ω·cm. The thermal conductivity of suspended graphene is 1500 – 2500 W/mK[15-17], and the value is reduced to 500 – 600 W/mK for graphene on an amorphous material[18]. In addition, graphene is stretchable showing stable resistance change at 11% stretching, and one order of resistance change at 25% stretching[3].

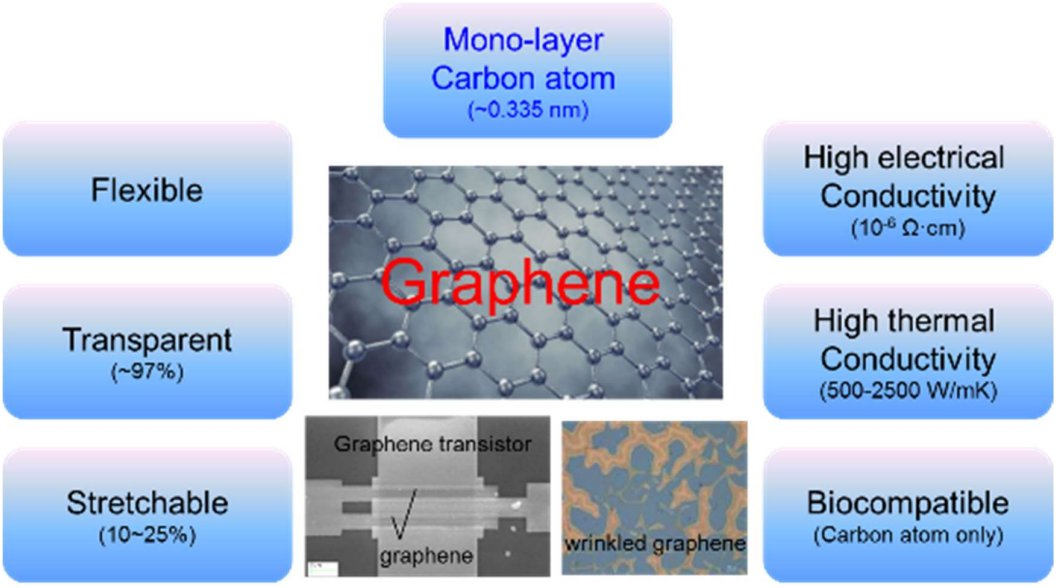

Figure 1.1 Representative characteristics of graphene

Transparent graphene electrodes

The ultra-flexibility and biocompatibility of transparent graphene electrodes can potentially provide an optimal platform for various applications including photovoltaic cells[19-22] and neural electrodes. Especially, neural electrode arrays with broad-wavelength transparency from the ultraviolet (UV) to infrared (IR) spectra are desirable, and provide unique opportunities to advance these techniques that would otherwise be impeded or impossible with conventional opaque metal electrodes. Transparent neural electrodes allow simultaneous observation of cells beneath electrode sites during optical or electrical stimulation. Graphene is one of the most promising candidates for transparent neural electrodes, because the material has a UV to IR transparency of over 90% in addition to its high electrical and thermal conductivity, flexibility, and biocompatibility.

Indium tin oxide (ITO) or ultra-thin metals can be used alternatively for transparent

neural electrode array[23-28]. However, the transmittance of ITO (~80 %) and ultra-thin metals (~60 %) are inferior to that of graphene (~90 %). ITO also does not have a flat transmittance across the visible spectrum. Even if it may be adequate in the visible spectrum for some applications, it has a steep roll-off in the IR region. Graphene has a very flat transmittance spectrum, which makes it equally sufficient for both optogenetic experiments in the blue spectrum as well as multiphoton imaging in the IR. It is important to use a material that allows for optimal transmittance in order to capture the clearest image or allow for the least light loss during optogenetic stimulation. Also, the brittleness of ITO may limit the conformability of the device on the brain surface[29]. In practice, ITO's high-temperature processing is not suitable for use with the low-glass-transition-temperature Parylene substrate of the micro-ECoG array[30, 31].

In this study, transparent graphene neural electrode arrays and their applications are presented in chapters 2, 3, and 4. Detailed introduction and background can be found in the next subsection, "1.2 Micro-Electrocorticography (μECoG)".

Graphene field-effect transistors

Field-effect transistors (FETs) have been one of the most researched device concepts since it is used in widespread applications including integrated logic circuits and radio frequency (RF) circuits. Although graphene is beneficial for the transparent electrodes, FET has been a major research field for graphene electronics. Among various possible FET applications, graphene is rather suitable for RF applications[32-36]. This is because graphene has extremely high carrier transport characteristics but limited I_{on}/I_{off} current ratio due to the zero bandgap nature. The high off-current may not be a serious problem in RF applications but

it could be problematic to demonstrate complex circuit systems. For example, in small-signal amplifiers, graphene RF transistors can be operated in the on-state and small RF is amplified at a certain DC bias state. However, if graphene transistors are used as logic transistors, the low on/off current ratio (typically 1~10) makes it difficult to distinguish between the on and off signals. Another possible application of graphene transistors could be biosensors that do not require a high on/off ratio. Recently, graphene transistors have shown their ability to detect chemicals, molecules, and cells[8-10].

In this study, graphene transistors with a bottom-gate structure are presented for the use of RF applications and future bio applications. In chapter 5, a graphene RF transistor with a buried bottom-gate and atomic layer deposition (ALD) Al_2O_3 is discussed. In chapter 6, a flexible graphene transistor with a bottom-gate coplanar structure on a Parylene C substrate is presented.

1.2 Micro-Electrocorticography (μECoG)

Among various applications of graphene, a transparent, flexible, and implantable neural electrode array is a pioneered device concept in this study. In this section, various types of neural interface devices are introduced focusing on μECoG which was adopted in our graphene neural electrode array. However, it is worth noting that our technology is readily amenable to other types of neural interfaces.

Types of neural interface device

Neural interface devices connect the nervous system and external devices and systems. These front-end devices have been a critical tool for the development of the brain-computer interface (BCI) also known as the brain machine interface (BMI) [37-40]. The methods of

interfacing with the nervous system and their corresponding electrodes can be mainly divided into four categories: external scalp recordings from electroencephalography (EEG), intracortical recordings from electrocorticography (ECoG), micro-electrocorticography (μECoG), and recordings from within the brain with penetrating electrode arrays (Figure 1.2). Each method and electrode has their own advantages and disadvantages. EEG records a collection of neural signals called local field potentials (LFPs) through the scalp, soft tissues below the scalp, and the skull. EEG is a relatively well-known and commonly used method because of its relative ease of use and non-invasive nature. However, the information acquired from EEG is quite limited because the neural signal quality diminishes with distance between the neurons and the EEG electrodes. ECoG and μECoG are methods which utilize electrode arrays which are placed directly onto the cerebral cortex. They measure neural signals directly from the cerebral cortex, eliminating the filtering of signals through the skull and scalp, creating a more information-rich signal than would be recorded from EEG. A typical, clinically available ECoG array has electrode size of around 1 cm in diameter. The μECoG array utilizes micro-scale electrodes with electrode site diameters that are orders of magnitude smaller than ECoG electrode sites and decreased inter-electrode spacing, allowing for greater spatial resolution of the neural signal and less invasive implantation techniques. Depending on the application, a μECoG device could have hundreds or thousands of electrode sites. Lastly, penetrating electrodes record neural signals from deep brain regions. They give the most information rich signal but also have the highest degree of invasiveness. Among these device types, the μECoG provides an appealing balance of information acquisition and spatial resolution with the degree of invasiveness (Figure 1.2).

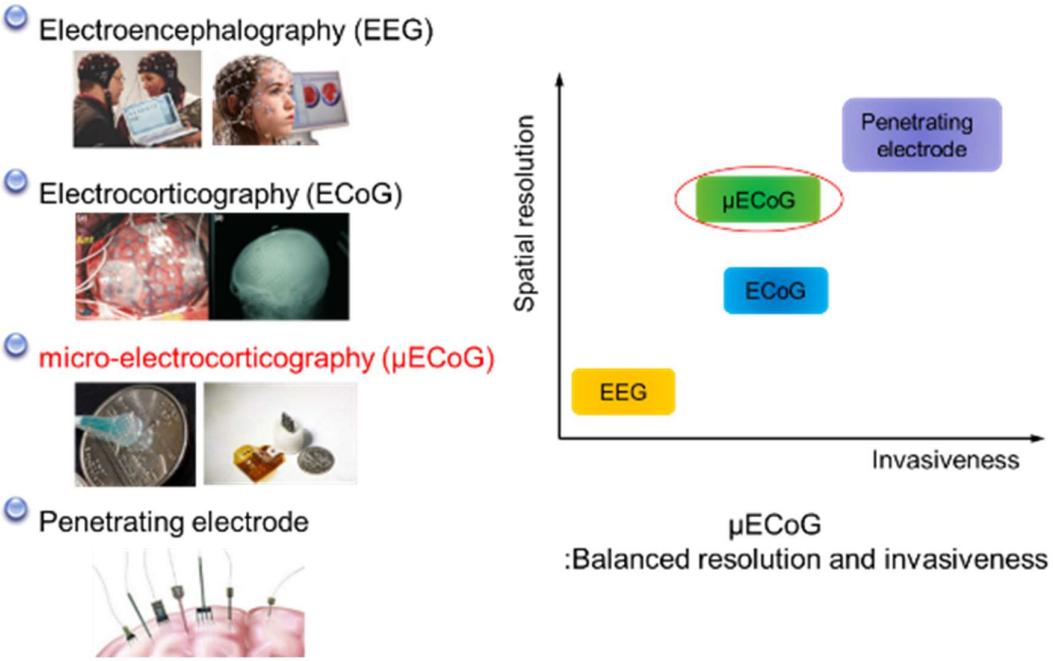

Figure 1.2 Types of neural electrodes and their comparison. μECoG is beneficial due to their balanced spatial resolution and invasiveness.

Electrode materials of μECoG

Platinum (Pt) is a common material used in various applications of neural stimulation and recording due to its ability to resist corrosion and large charge carrying capacity[37, 38, 41-44]. This allows for long term reliability of electrodes in chronic studies. Also platinum is common in general microfabrication due to its ease of use. Iridium oxides are an emerging material in neural stimulation electrodes because of the large injection charge via reversible reduction and oxidation between Ir3+/Ir4+ valence states within the oxide film[43, 45, 46]. Poly(3,4-ethylenedioxythiophene) (PEDOT) is also known for their large charge carrying capacity with lower impedance[47-49]. However, these materials are optically opaque so *in vivo* studies have been limited to the vicinity of the electrode sites (Figure 1.3).

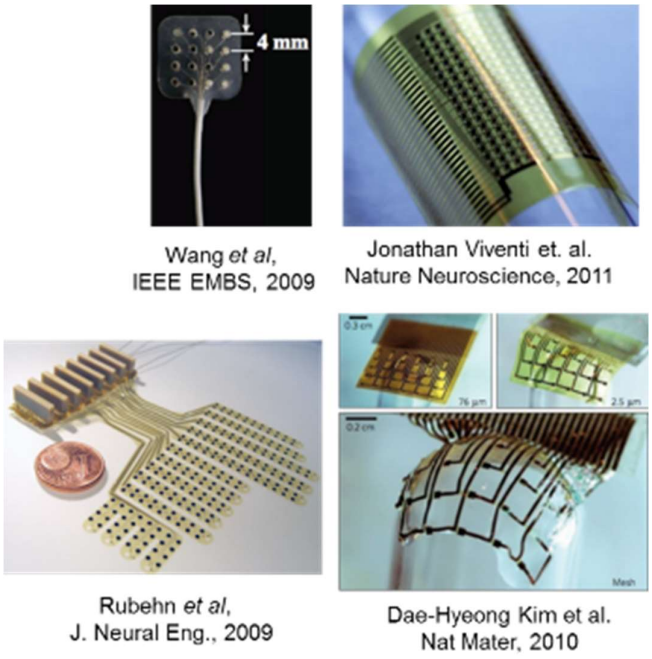

Figure 1.3 Previously demonstrated metal-based opaque neural electrodes. In vivo monitoring directly underneath the electrode sites has been limited.

In contrast, optical imaging of the cortical areas of the brain while recording the electrical activity through surface electrodes is possible with graphene. Unlike the conventional metal-based materials, graphene's optically transparent nature and electrically conductive properties make it a favorable material for neural electrode implementation. In this study, transparent graphene neural electrode arrays that can provide a unique opportunity for electrophysiology, *in vivo* monitoring, and optogenetics are discussed in chapter 2. In chapter 3, detailed evaluation results of the graphene neural electrodes are presented along with the electrical stimulation in GCaMP6f mice. In chapter 4, utility of the graphene electrodes in multi-electrode electroretinography (meERG) is discussed.

Chapter 2. Graphene-based Carbon Layered Electrode Array (CLEAR) technology for electrophysiology, neural imaging, and optogenetic applications

2.1 Introduction

Graphene, a novel two dimensional carbon-based material, is one of the most promising candidates for transparent neural electrodes, because the material has a UV to IR transparency of over 90 % in addition to its high electrical and thermal conductivity, flexibility, and biocompatibility[1, 2, 4, 7, 10, 50-52]. In this chapter, the fabrication of the transparent graphene neural electrode array and its utility to electrophysiology, fluorescent microscopy, optical coherence tomography (OCT), and optogenetics are presented. The technology we developed is name as Carbon Layered Electrode Array (CLEAR) technology. The CLEAR device is fabricated from graphene monolayers, which results in an optically transparent, ultra-flexible and conformal micro-electrocorticography array that is suitable for *in vivo* optical imaging and optogenetic cortical neural modulation experiments in rodents. The fabrication methods and the surgical protocols described herein are based on the graphene microelectrocorticography (μECoG) electrode array that can be implanted on the surface of the cerebral cortex[52]. However, the methods may be amenable to fabrication and testing of a multitude of other electrode arrays used in biological research such as penetrating neural electrode arrays to study deep brain, nerve cuffs used to interface with the peripheral nervous system or devices that interface with the muscular system. Further possible applications such as transparent penetrating electrode arrays and multi-electrode electroretinography are also described.

2.2 Fabrication of CLEAR μECoG

Fabrication process in brief

The CLEAR μECoG was fabricated on a 4-inch silicon wafer. Figure 2.1 and 2.2 show schematic illustrations of the fabrication process. Briefly, wafers were coated with Parylene C films using a chemical vapor deposition process. Next, the connection pads and initial portions of the traces were patterned with gold via electron beam evaporation and lift-off techniques. The use of gold for the traces and pads was necessary to ensure a good mechanical connection to the zero insertion force (ZIF) printed circuit board (PCB) connectors used for reading the brain signals into the computer. The electrode sites and portions of the traces that were to be in contact with the brain were left for the subsequent graphene transfer and patterning, such that the brain contact area of the electrode would be transparent. Following metallization, four graphene monolayers were transferred and stacked sequentially onto the wafer surface, using the wet transfer technique described in the subsection "graphene wet transfer and stacking method" in the next page. A sacrificial layer of SiO_2 was then deposited to protect the graphene layers from being etched in the reactive ion etching (RIE) steps to follow. After that, the graphene was patterned to form the electrode sites using RIE, and another insulating layer of Parylene C was deposited. RIE was then employed to expose the electrode sites and pads, and form the array outlines. Finally, the devices were peeled from the wafer, the SiO_2 protection layer was removed by wet etching, and the arrays were inserted into the PCB connectors. The

detailed fabrication protocols are described in appendix A1.

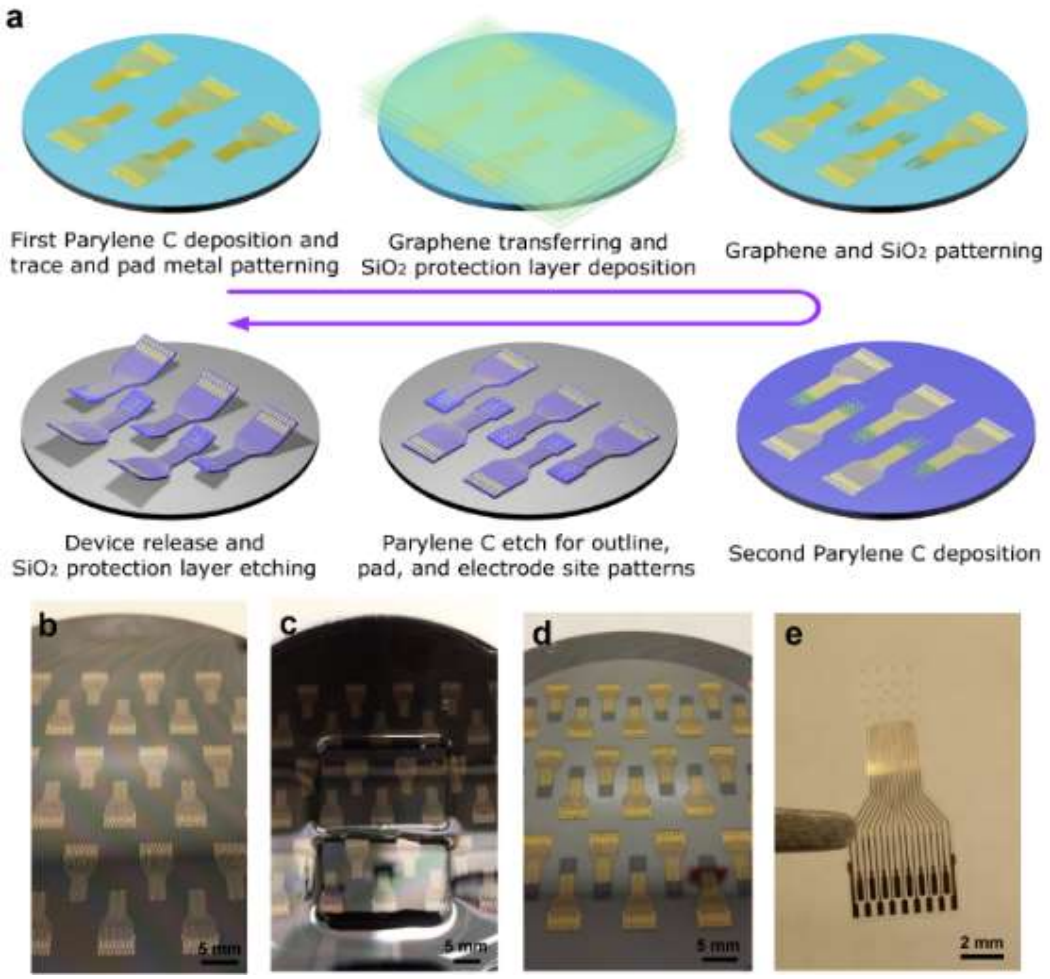

Figure 2.1 Fabrication procedure for transparent graphene electrode array. (a) Fabrication process on a silicon substrate. Large-scale fabrication is possible depending on the size of graphene. (b) After metal trace and pad patterning. (c) After the graphene was transferred, water was poured to verify the existence of graphene. The hydrophobic characteristic of graphene makes clear water edges. Two graphene sheets of size ~2×3 cm were transferred onto the substrate. The graphene portion can be increased by using larger graphene sheets or by transferring multiple graphene sheets. (d) After Parylene C patterning. (e) After device releasing and SiO_2 protection layer etching.

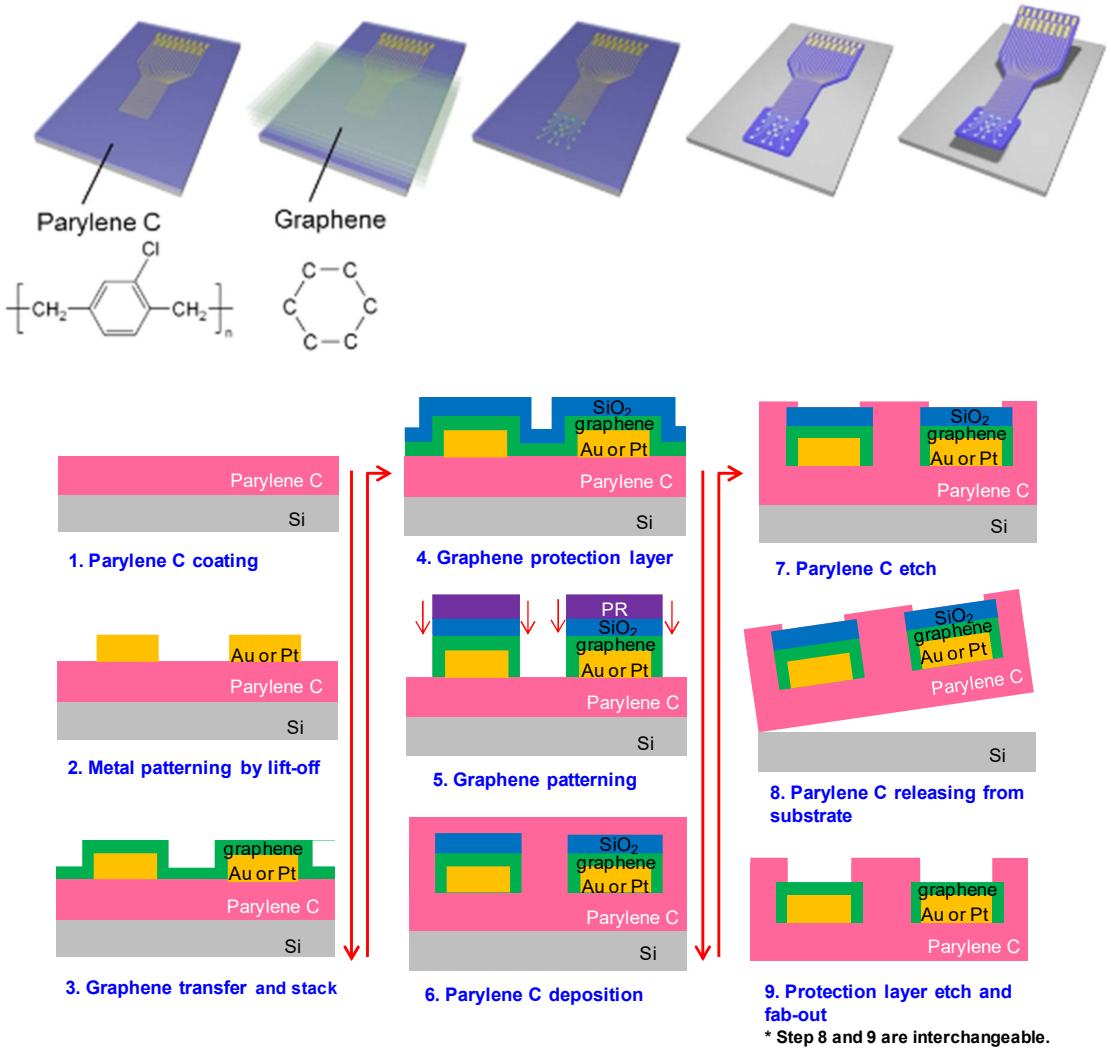

Figure 2.2 Detailed, cross-sectional fabrication process flow.

Figure 2.3 shows fabricated CLEAR μECoG device. The device is fully transparent in the electrodes area due to the transparency of the graphene. Optical and electrical characterization can be found in the following sections. The protocols of PCB connection and reference/ground wiring are described in appendix A1.

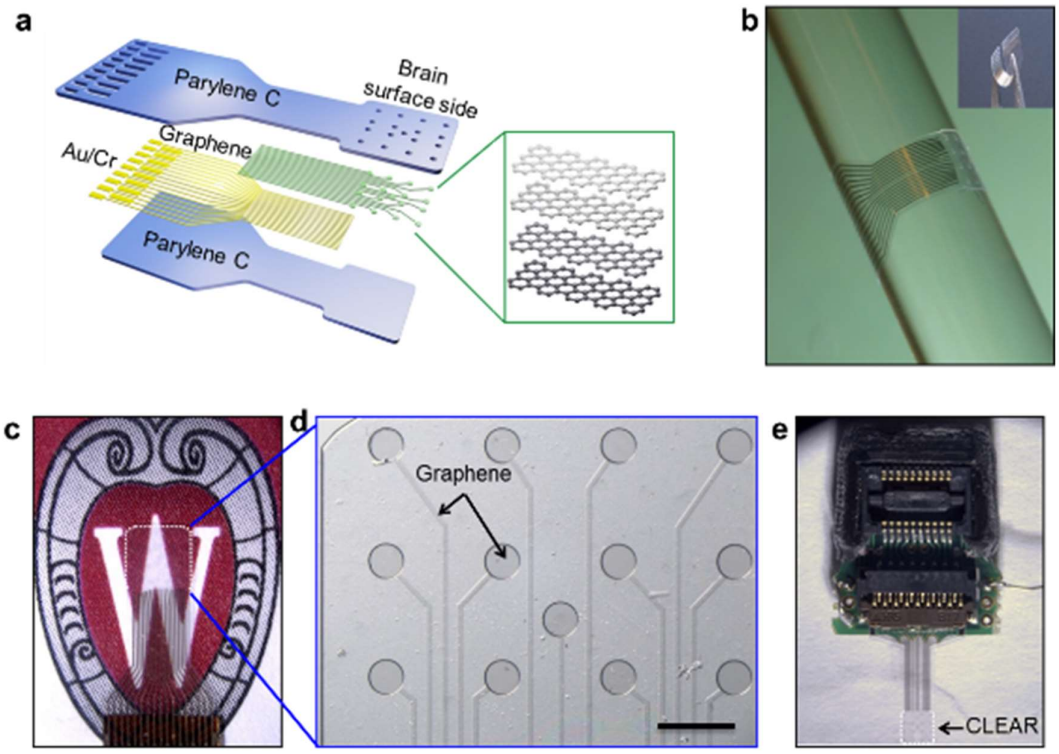

Figure 2.3 Fabricated CLEAR micro-ECoG device. (a) Diagram of CLEAR device construction showing the layered structures. (b) Demonstration of CLEAR device flexibility. The device is wrapped around of glass bar with a radius of 2.9 mm. (c) Rat-brain sized CLEAR device: outlined by white dashed line (electrode area of 3.1×3.1 mm^2). (d) Close-up of rat-sized device showing transparent graphene electrode sites and traces on a Parylene C substrate. This side touches brain surface. Scale bar represents 500 μm. (e) Mouse-brain sized CLEAR device with ZIF PCB connector (electrode area of 1.9×1.9 mm^2).

Preparation of graphene

Mono-layer graphene synthesized by chemical vapor deposition (CVD) was used in the CLEAR technology. However, any graphene synthesis method that can make uniform graphene would work if the synthesized graphene is transferable to a foreign substrate. In the CLEAR technology, four-layer graphene has been determined to have a transmittance of over 90 %[52]. The total number of graphene layers can vary from one to several layers, but there

is a relationship between transmittance and resistance as additional layers of graphene are added[52]. For instance, one or two layers of graphene has higher transmittance and lower resistance. More details about the optical and electrical properties can be found in the "Electrical and optical properties of CLEAR μECoG" section. Another trade-off is the mechanical/electrical reliability and cost/time effectiveness. Lower numbers of graphene layers are more cost- and time-effective but might be more vulnerable to damage during the fabrication and the implantation processes. Further study of the effects of varying graphene layers would be valuable. Synthesized multi-layer graphene is a possible alternative to stacking mono-layer graphene. Currently, commercial CVD graphene is available and can be used for this protocol. Commercial mono-layer CVD graphene grown on copper (Cu) foil can be also utilized.

Graphene wet transfer and stacking method

Schematic illustration of the process is depicted in figure 2.4. The graphene stacking began with CVD graphene growth on a copper (Cu) foil. Mono-layer graphene was grown on both the top and bottom sides of the Cu foil. To utilize the top side graphene, back side graphene was etched using oxygen (O_2) plasma (50W, 10 sccm O_2, 10 mTorr, for 1 minute). The top side graphene was coated by 950k PMMA (polymethyl methacrylate) C4 (MicroChem) to protect the one-atom thick graphene layer. The Cu was etched in 0.25 M ferric chloride ($FeCl_3$) for 3 hours and rinsed in de-ionized (DI) water. Figure 2.5 shows the CVD graphene before and after Cu etch. The graphene was cleaned in 1:10 hydrofluoric (HF) acid for 1 hour to remove the copper composite residues and rinsed in DI water. The first graphene transfer was then performed on the desired substrate. After drying the PMMA/graphene sample in a N_2 atmosphere dry box, the PMMA was removed using acetone and the sample was rinsed in DI

water. Following the above procedure, the graphene stacking was performed on the previously graphene-transferred substrate. Multiple layers of graphene could be stacked using this method.

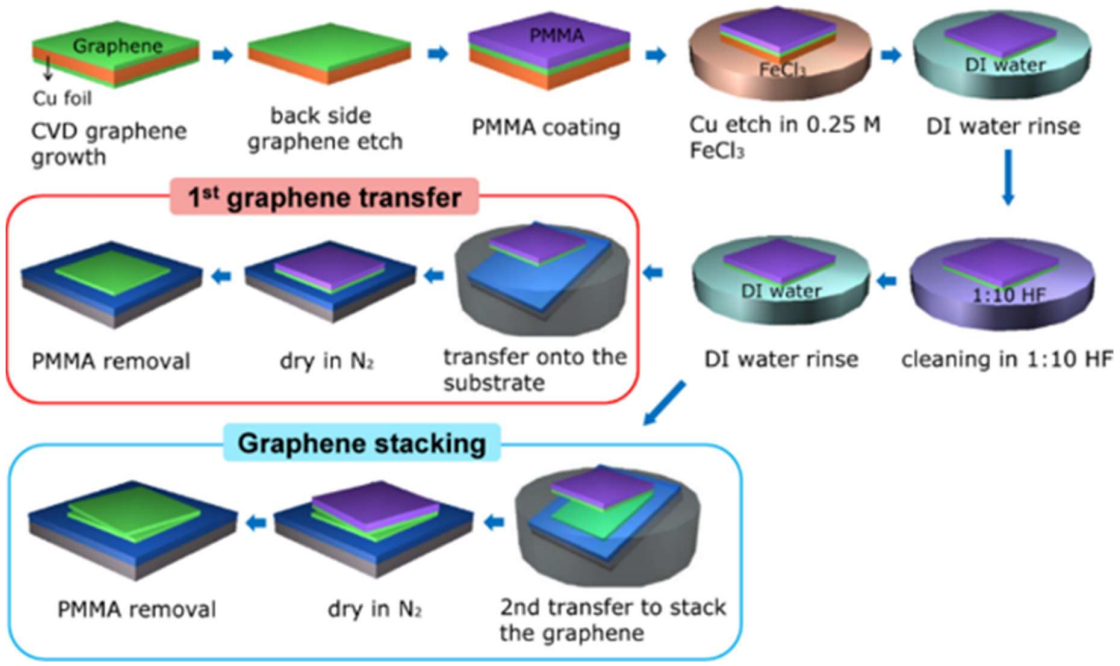

Figure 2.4 Schematic illustration of graphene wet transfer and stacking process

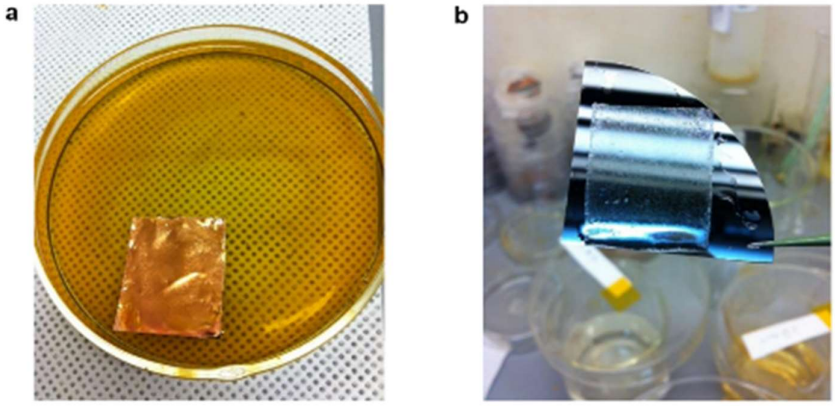

Figure 2.5 The CVD graphene was grown on a 2 cm x 3 cm piece of copper (Cu) foil. (a) PMMA/graphene/Cu on Cu etchant ($FeCl_3$). (b) After the Cu was completely etched, the PMMA/graphene sheet was moved to DI water using a piece of silicon wafer.

Wetting property control of Parylene C

Prior to graphene transfer on Parylene C substrate, the Parylene C surface was changed from hydrophobic to hydrophilic for favorable graphene transfer. The inherent hydrophobic surface of Parylene C needs to be modified to have hydrophilic surface by adding hydroxyl (OH) group. Figure 2.6 shows two methods to change the wetting properties of Parylene C. The first method is depositing thin layer of SiO_2 (2 nm). The second is oxygen plasma treatment. In real device, the oxygen plasma treatment was adopted not adding any addition layer.

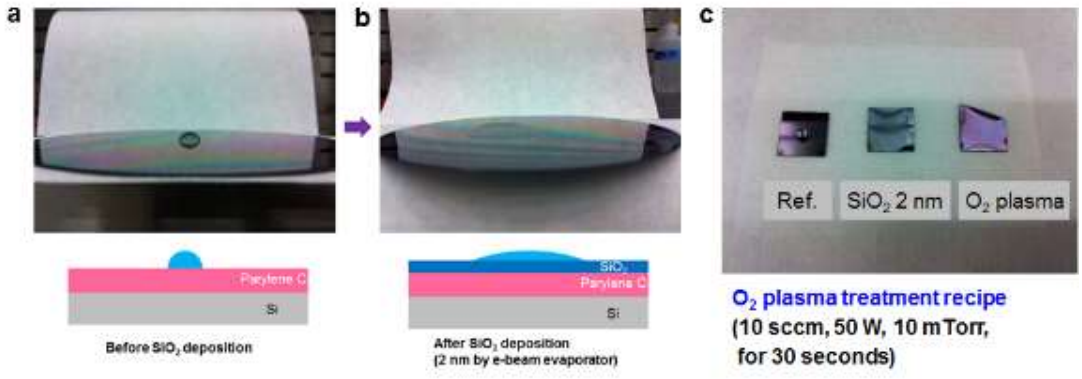

Figure 2.6 Wetting property changes of Parylene C after oxygen plasma treatment and SiO2 deposition. (a) Water droplet on hydrophobic Parylene C substrate prior to SiO_2 deposition. (b) Water droplet on hydrophilic Parylene C substrate post SiO_2 deposition. (c) Comparison of wetting properties for bare Parylene C, Parylene C with 2 nm of e-beam evaporated SiO_2, and oxygen plasma-treated (10 sccm, 50 W, 10 mTorr, 30 sec) Parylene C. Plasma treatment was used in this study.

Graphene sheet transfer onto Parylene C coated wafer

Transferring graphene onto a substrate is a critical step in the fabrication of the graphene neural electrode array. Stacking multiple mono-layer graphene grown on copper (Cu) foil is preferred for better uniformity and tunable transmittance. Each mono-layer graphene layer degrades the transmittance by ~2.3 % and increases conductance. Synthesized multi-layer

graphene grown on nickel (Ni) foil can be used, but normally is not uniform because of having different number of graphene layers over the Ni foil. This protocol is based on stacking mono-layers of graphene onto a metal-patterned substrate. However, alternatively, graphene stacking can be done first followed by metal deposition and patterning on the graphene. Figure 2.7 shows the images of graphene transferring on a pre-patterned wafer.

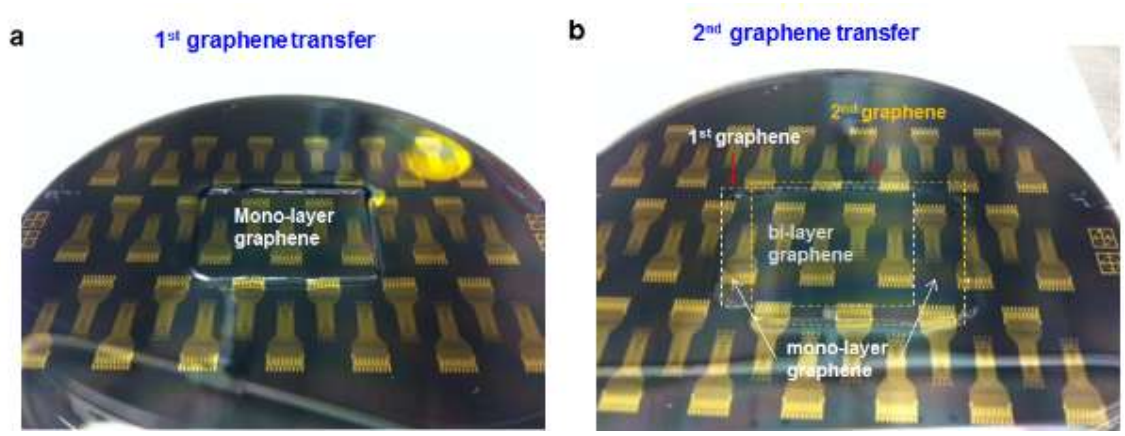

Figure 2.7 Graphene sheets after transfer onto pre-processed wafer surfaces. (a) Monolayer graphene sheet after transfer onto a pre-processed Parylene-coated silicon wafer. DI water was poured onto the surface of the wafer for verification of the existence of the graphene sheet. Since graphene is intrinsically hydrophobic, due to the coherent bonding of carbon atoms, water does not spread onto the sheet, but instead flows onto the surrounding hydrophilic, plasma treated, Parylene C. (b) The same wafer after transferring the second graphene sheet. The second graphene sheet was intentionally misaligned in this case to make both monolayer and bilayer regions, for comparison tests.

Graphene Characterization using Raman spectroscopy

The mono-layer graphene and multi-layer graphene samples were characterized using Raman spectroscopy. Raman spectroscopy has been used as a fundamental method to investigate phonon characteristics of graphene, and can aid in identifying the existence of graphene on a particular substrate and the number of graphene layers present[53-56]. The intensity ratio changes of the 2D and G peaks for 1, 2, and 3-layer graphene verified the

viability of the graphene stacking process, showing the unique phonon characteristics of graphene layers (Figure 2.8). The single sharp G peak is characteristic of the two-dimensional sp^2 bonded carbon atoms of graphene. For the 1-layer graphene, the G peak was located at 1572.5 cm^{-1}, and for the 3-layer graphene, the G peak was at 1563.3 cm^{-1}. Therefore, as the number of graphene layers increased, the G peak showed a left shift (redshift). The 2D peaks were at 2633 cm^{-1} for the 1-layer graphene and at 2640.7 cm^{-1} for 3-layer graphene, showing that the 2D peak experienced a right shift (blueshift) with increasing graphene layers. These peak shift trends are consistent with the previous Raman study for multilayer graphene[54, 55].

The 2D to G peak intensity ratio (I_{2D}/I_G) trend shown in Figure 2.8(d) demonstrates the changes occurring with the addition of each graphene layer. For the 1-layer graphene, the G peak intensity was the lowest, while the 2D peak intensity was the highest with $I_{2D}/I_G = 3.63$. As the number of graphene layer was increased, the G peak intensity was increased and the 2D peak intensity was decreased, resulting in I_{2D}/I_G ratios for 2-layer and 3-layer graphene were 1.43 and 0.91, respectively. This decreasing I_{2D}/I_G ratio is characteristic of multilayer graphene samples. It is also important to note that the D peak near 1350 cm^{-1}, which is generally a result of sample defects, was not significant for the graphene layers. This proves that the CVD graphene grown for this study did not have a significant number of defects before and after stacking.

The intensity ratio changes of the 2D and G peaks for mono- and multi-layer graphene can be utilized to verify the number of graphene layers. A Raman spectroscopy of the 4-layer graphene on Parylene C is presented in figure 2.8(h). The peaks are in correspondence with earlier reports on the Raman spectroscopy of graphene and Parylene C[55, 57, 58].

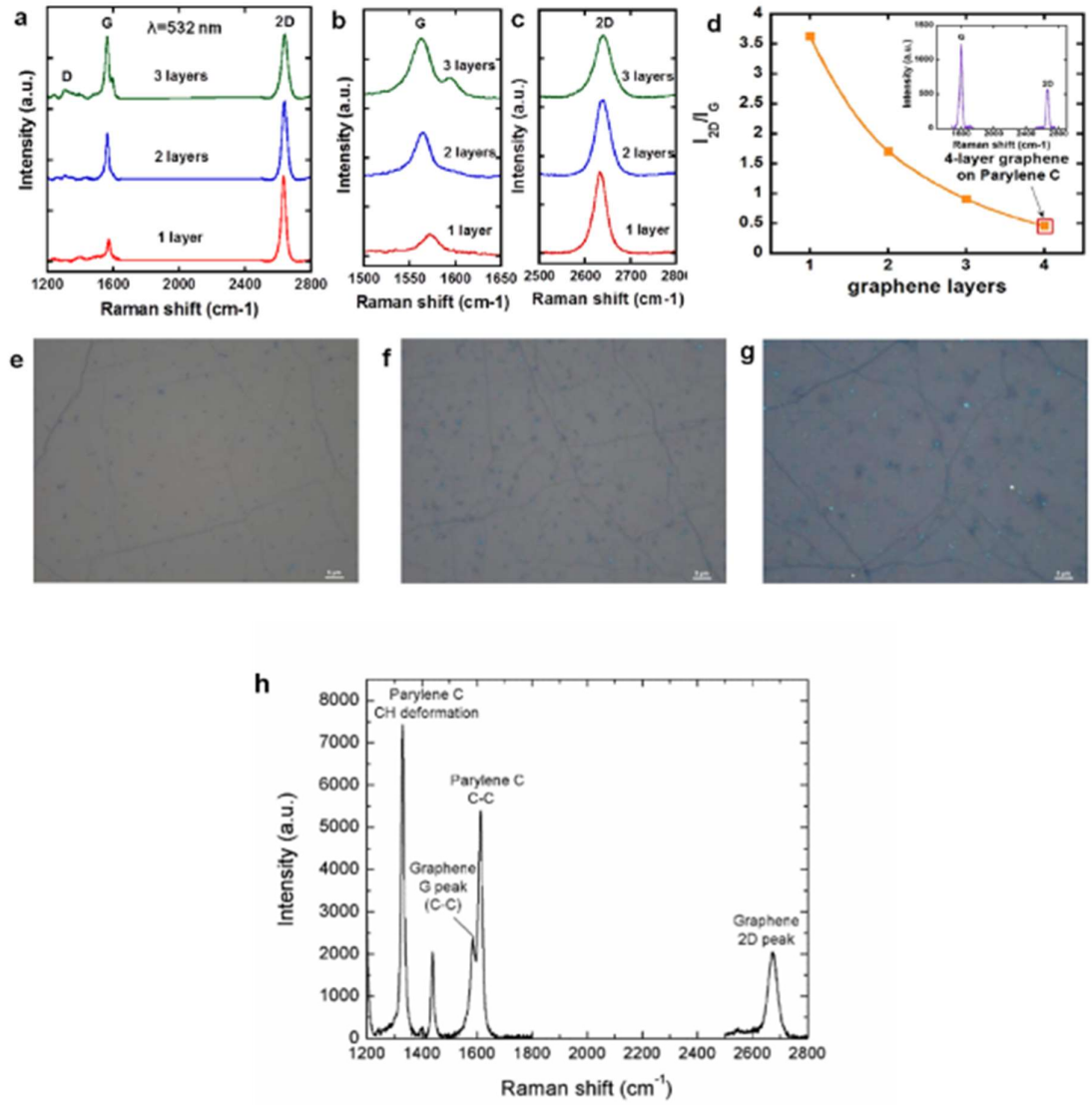

Figure 2.8 Raman spectroscopy of stacked graphene. (a) G and 2D peaks for 1, 2, and 3-layer graphene. (b) and (c) Enlarged G and 2D peak regions, respectively. (d) G and 2D peak ratio (I_{2D}/I_G) trend versus number of graphene layers. The Raman spectroscopy was carried out with a Horiba LabRAM ARAMIS Raman system using a 532 nm green laser and a 100x objective. Microscope images of (e) 1 layer, (f) 2 layers, and (g) 3 layers of graphene. (h) Raman spectroscopy of 4-layer graphene on Parylene C. Graphene shows a G peak near 1580 cm^{-1}, which is characteristic of the two-dimensional sp^2 bonded carbon atoms, and a 2D peak near 2670 cm^{-1}, which is the second order of D peak. The peaks near 1330, 1438, and 1610 cm^{-1} are attributed to the Parylene C[57].

2.3 Electrical and optical properties of CLEAR μECoG

Characterization of methods in brief

Evaluation of a transparent electrode material in terms of transmittance and resistance provides a prediction of the feasibility of experimental methods such as electrophysiology, neural imaging modalities, and optogenetics. The transmittance and the sheet resistance of CVD graphene were measured using a spectrometer and transmission line method (TLM)[59], respectively. Sheet resistance is widely used to evaluate and compare conducting materials[5, 23, 24, 27, 28]. Other optical measurement systems and resistance measurement methods such as a four-point probe could be utilized as well.

It is also important to test the fabricated transparent graphene electrode array using Electrochemical impedance spectroscopy (EIS) and cyclic voltammetry (CV). The in vitro testing ensures the performance of the device and is useful to check the yield of the electrode array. The EIS and CV are the fundamental tools used to estimate the ability of the electrodes for recording and stimulation purposes[45, 60].

Transmittance measurement results

For both imaging and optogenetic application of the CLEAR device, the amount of light transmitted through the graphene electrode sites and Parylene substrate is critical. Since the intention for the transparent device is that one can both image and project light onto the underlying brain tissue, it is important that a large percentage of the light impinging on the array is transmitted through the device. A plot of the light transmittance versus wavelength for Parylene, 4-layer graphene, CLEAR (4-layer graphene/parylene), and ITO/PET films is shown in Figure 2.9. The measurements were taken for light wavelengths from 300 to 1500 nm using a UV/Vis Spectrometer. The sinusoidal shape of the transmittance curve is common for the

Parylene C material[61]. For the CLEAR device, an average of about 90% of the light impinging on the substrate is transmitted at the desired wavelengths (470 nm for excitation of channelrhodopsin and 570 nm for halorhodopsin). This is similar to previously reported results, and is sufficient for numerous optogenetic and imaging applications[3, 25]. To compare the CLEAR and ITO films, commercial ITO/PET films with similar sheet resistance values (60 Ω/□ and 100 Ω/□) were measured using the same instrument. For both films, an average of around 80 % transmittance in the visible-IR range and dramatically reduced transmittance near the UV range are shown. In addition, a transmittance difference of ~10 % is shown in the 420-440 nm range which is attributed to the different properties of the ITO films.

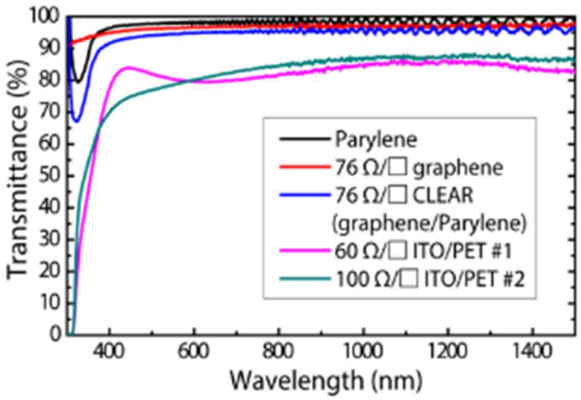

Figure 2.9 Light transmittance test results for 76 Ω/□ four graphene monolayers on a 15 μm Parylene C film (CLEAR), 76 Ω/□ four graphene monolayers only (Graphene), Parylene C film only (Parylene), 60 Ω/□ ITO/PET, and 100 76 Ω/□ ITO/PET film.

Graphene sheet resistance measurement

In a material, inherent tradeoffs exist between transparency and conductivity. Generally, by increasing the thickness of a material, the conductivity is increased but the transparency is decreased. This tradeoff also exists in the graphene case. Bae et al. reported an increase in conductance (i.e. sheet resistance decrease) and a decrease in transmittance when

going from one to four graphene monolayers[5]. To measure the sheet resistance of the graphene, transmission line method (TLM) was performed. Figure 2.10 shows the fabricated TLM pattern with graphene channel lengths from 10 μm to 50 μm. For etch length, five samples were measured and the average values are plotted. Figure S7b shows the total resistance (R_T) versus the length (L) plot for monolayer graphene. Using the TLM theory, the sheet resistance can be extracted from the following equation:

$$R_T = \frac{R_s}{W} \cdot L + 2R_c = slope \cdot L + 2R_c$$

Where R_T is the measured total resistance, R_S is the sheet resistance, R_C is the contact resistance, W and L are the width and length of the TLM pattern, respectively.

From the equation, the slope of the graph is as follows:

$$slope = \frac{R_s}{W}$$

Now, the sheet resistance can be extracted from the slope of the linear fit line as below:

$$R_s = slope \cdot W = 1.5177 \times 100 = 151.77\ \Omega/\square$$

Similarly, sheet resistance of the stacked graphene can be extracted using the TLM.

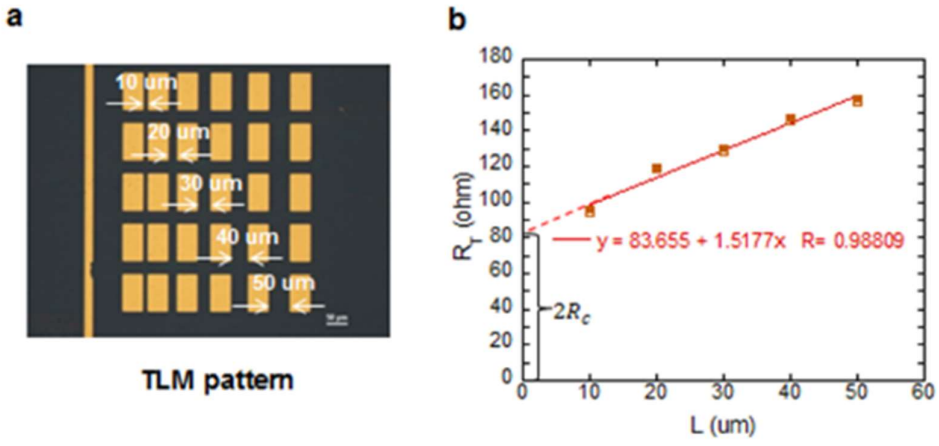

Figure 2.10 Transmission line method (TLM) for sheet resistance extraction. (a) Fabricated

TLM pattern with graphene channel length from 10 to 50 μm, the channel width is 100 μm. (b) Total resistance versus channel length for monolayer graphene.

Figure 2.11 shows the sheet resistance decrease from 152 Ω/□ to 76 Ω/□ for 1-layer and 4-layer graphene. This shows a similar sheet resistance trend to the previous report. For the CLEAR device, 4-layer graphene was chosen to have the minimum sheet resistance while maintaining around 90 % transmittance[5].

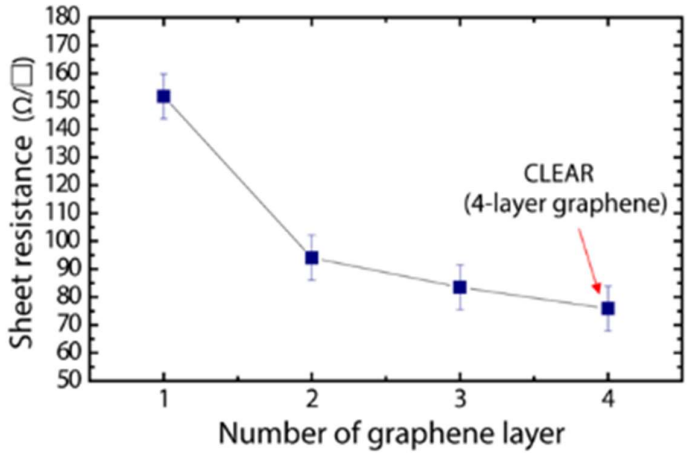

Figure 2.11 Trend of sheet resistance as a function of the number of graphene layer. The error bar represents the standard deviation of sheet resistance extracted from 5-sample measurement.

Comparison between transparent materials

For a more quantitative comparison between the graphene, ITO, and ultrathin metal films, the measured transmittance and sheet resistance values are plotted in Figure 2.12, along with various values reported in the literature. It is meaningful to compare transparent materials with a similar resistance range. The four-layer graphene (~1.3 nm) on 25 μm Parylene C (CLEAR device) showed the best transmittance at ~90 %, outperforming the indium tin oxide (ITO) on polyethylene terephthalate (PET) (127 μm, Sigma Aldrich) which had ~80 % transmittance, and the ultrathin metal film (9 nm silver, 5 nm aluminum, 3 nm palladium),

which had ~60 % transmittance in the range of 10 to 100 Ω per square sheet resistance. Also, the graphene showed broad-wavelength transparency in the wavelength range from 300 nm (ultraviolet, UV) to 1500 nm (infrared, IR).

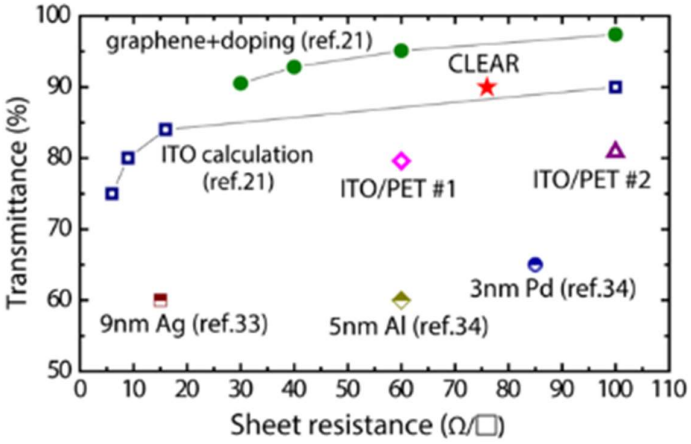

Figure 2.12 Transmittance versus sheet resistance graph for various conducting materials (graphene, ITO, ultrathin metals). The reference number in the figures is correspondent in the previous paper (Park, D.-W. et al., Nat. Commun, 2014).

Electrochemical impedance spectroscopy (EIS)

The patency of the completed devices was verified via electrical impedance spectroscopy. Impedance spectra were obtained for each electrode site using an Autolab PGSTAT12 potentiostat. Devices were connected to the Autolab machine via the PCB connectors, which were connected to a passive 32-channel Tucker-Davis Technologies (TDT) head stage. Impedances were evaluated at 30 different frequencies, ranging from 10 Hz to 30,937 Hz. If electrode sites had impedance values less than 600 kOhms at 1 kHz frequency, they were considered to be viable for implantation. 1 kHz frequency was selected for evaluation because it is known to be a common benchmark for neural impedance analysis[62, 63]. Figure 2.13 shows representative electrochemical impedance spectra for CLEAR and traditional platinum micro-ECoG devices tested in saline. It is apparent from the plot that the phase angle

is higher in the case of the CLEAR device. This means that the value of the reactance is higher for the graphene sites than for the platinum. However, the average magnitude of the impedance at 1 kHz frequency was only slightly higher for the CLEAR device than for the platinum array (243.5 ± 5.9 kΩ for graphene vs 188.8 ± 92.9 kΩ for platinum). Since the signal recording apparatus involves the use of a high input impedance amplifier, the reactance difference is not expected to have adverse effects on the signal recordings. It is worth noting that the impedance is dependent on physical dimensions of the electrodes and measurement setup (e.g. input wave form and frequency range). More impedance study results are described in Chapter 3.

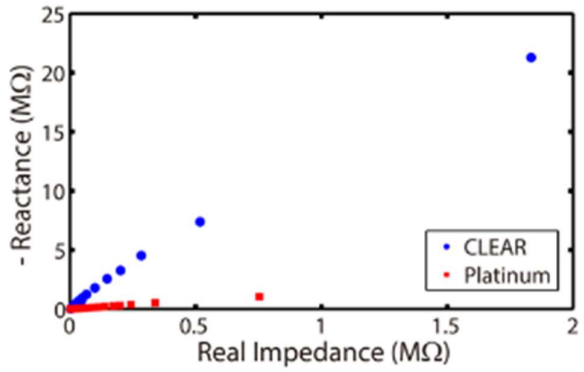

Figure 2.13 Electrical impedance spectra for CLEAR and platinum micro-ECoG devices in saline. X-axis represents real impedance; y-axis represents imaginary impedance. Each point was taken at a different frequency, between 10 Hz and 31 kHz.

Cyclic voltammetry (CV)

Cyclic voltammetry (CV) was performed on select CLEAR devices, and on devices with gold and platinum electrode sites, for comparison purposes. CV was also performed using the Autolab system. CV scans were taken from -0.6 V to 0.8 V with a step potential of 0.0105 V and a scan rate of 0.0500 V/s[64, 65]. The voltage range was chosen so as to stay within the water window. However, the voltage range and the scan rate can be changed for different purpose of stud. Average CV curves for gold, platinum, and CLEAR devices are shown in

Figure 2.14. The CV results for the platinum device were drastically different than those for either the gold or the CLEAR devices. Although this demonstrates that the platinum electrode sites have a greater charge carrying capacity, it does not rule out the use of CLEAR devices for neural interfacing applications. In fact, the average CV curves for the CLEAR and gold electrode sites were similar. As gold has proven itself as a reliable material for recording electrode sites[66, 67], this suggests that the graphene electrodes will also be sufficient.

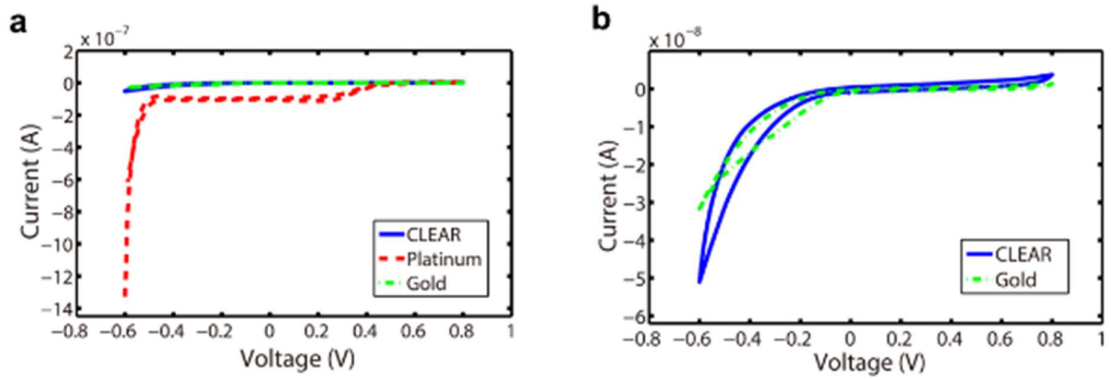

Figure 2.14 (a) Average cyclic voltammetry results over 16 electrode sites on CLEAR, gold, and platinum micro-ECoG arrays. (b) Average cyclic voltammetry results for 16 electrode sites on CLEAR and gold micro-ECoG arrays.

Electrochemical artifact

The construction of completely transparent neural surface electrode arrays enables unique research capabilities in combining optogenetics with electrophysiology, by allowing for delivery of light stimuli through the array, directly to the brain region from which the recordings are obtained. Even though the electrodes are optically transparent, an artifact is still present when high intensity light is applied directly onto an electrode site. The artifact is generally smaller in amplitude and temporally different than the optogenetically evoked neural signal. The artifact is reproducible and can be characterized by testing the electrode site in saline,

implanting into wildtype animals or testing in cadaver experiments. To test the artifact, the devices were placed face-down in saline solution and a 200 μm optical fiber connected to a 100 mW, 473 nm diode laser, was used to shine light onto the backs of the electrode sites. The light pulses were delivered by applying 3 V to the laser for 3 ms (up to 63.7 mW/mm^2). Figure 2.15 shows the electrical pulses elicited by the light impingent on graphene and platinum sites. From the plot, it appears that the amplitude of the artifact is similar for both the graphene and the platinum sites, although the platinum electrode returns to baseline more quickly. We expect the main mechanism of the artifact is similar to when light is applied to a conventional metal electrode, which is known as Becquerel effect, a classical photoelectrochemical effect first demonstrated by Becquerel in 1839[68, 69].

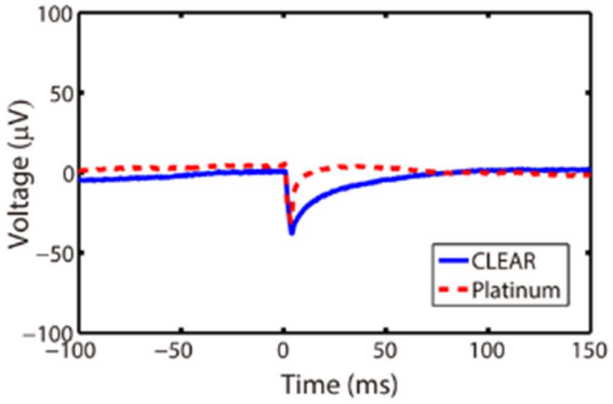

Figure 2.15 Average artifact effect test results for CLEAR and platinum micro-ECoG devices, with light applied to a single electrode site on each device via an optical fiber attached to a blue laser, with an application of 63.7mW/mm^2 power for 3 ms.

Additional experiments also showed similar dependency on the light stimulation time and power as to the metal electrode case (Figure 2.16)[70]. The amplitude of the artifact increased as the stimulation time was increased from 3 to 25 ms, which is similar to what has been reported previously in varying metal electrodes [http://www.openoptogenetics.org/index.php?title=Light-Induced_Artifact]. The peak of the artifact also increased temporally as stimulation duration increased. Additionally, the light power dependency was similar to that of

the metal electrode[70], where the artifact decreased with decreasing stimulation power (Figure 2.16(b)). It is interesting to note that the artifact is significantly lowered when the stimulus power is reduced, which is expected from traditional metal electrode behavior. It is therefore important to note that the stimulus artifact may be reduced or eliminated with lower level light stimulus, such as would be subjected during traditional imaging paradigms. Other strategies can also be employed to further characterize and reduce the stimulus artifact, as have been proposed in other optogenetic studies[71], and ones that have been similarly successful in dealing with electrical stimulation artifacts[72]. Further study will be necessary to fully characterize the overall performance of the graphene devices and source of potential artifacts.

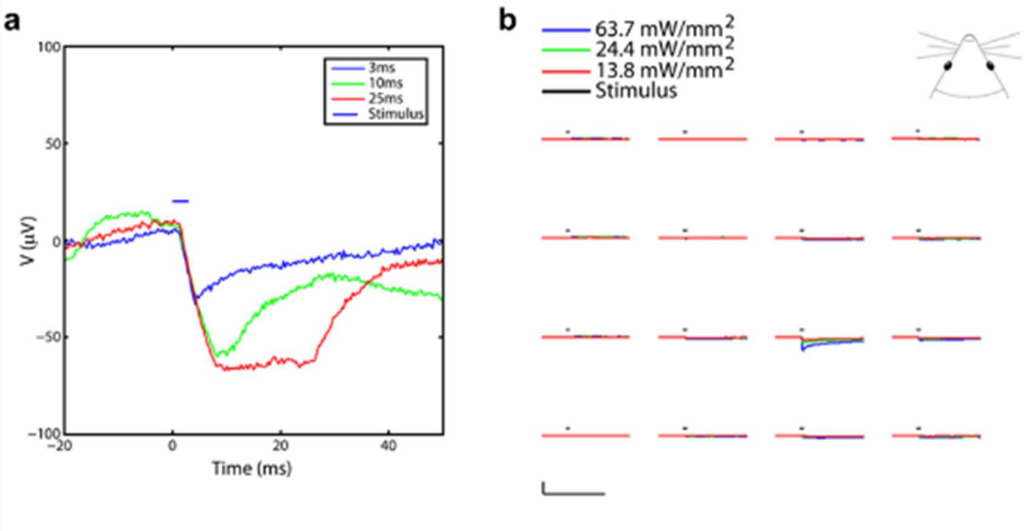

Figure 2.16 (a) Artifact experimental results dependent on light stimulus time duration varying from 3 ms to 25 ms tested in a wild type chronically implanted rat with graphene electrode site. (b) Artifact experimental results dependent on the light stimulus power ranging from 13.8 mW/mm^2 to 63.7 mW/mm^2 done in cadaver ChR2 mouse.

2.4 Electrophysiology

Surgical implantation

To demonstrate the in vivo performance of the CLEAR devices, the arrays were implanted in four rats and five mice, one wild-type mouse for imaging and four Thy1::ChR2 mice for imaging and optogenetic testing. Table 1 describes the type of implantation performed in each case and the type of data collected from each animal. Three of the rat implantations were bilateral, with CLEAR and the platinum devices implanted within the same animal for a fair comparison and to reduce overall animal numbers. Surgical procedures and in vivo imaging sessions were performed under anesthesia, and all efforts were made to minimize animal discomfort. CLEAR and platinum MicroECoG arrays were implanted in male Sprague-Dawley rats approximately two months old, and male and female Thy1::ChR2/H134R-YFP (Jackson Labs 012350) and wildtype mice approximately 6 to 16 weeks old. After receiving pre-operative injections of buprenorphine (for pain management) and dexamethasone (to prevent brain swelling), animals were anesthetized with isoflurane gas and their heads immobilized. Incisions were made over the top of the skull and craniotomies were made with a surgical drill. Electrodes were stereotactically placed on the surface of the brain, over somatosensory cortex, and circular glass coverslips were applied over the top of the array, forming the cranial window. The edges of the coverslips were sealed to the skull using dental acrylic. Ground and reference wires were attached to stainless steel screws, drilled into (rats) or glued to (mice) the skull. After everything was in place, the exposed screws were covered with dental acrylic to form a smooth cephalic implant. The skin was then sutured around the implant in rats and the animals were recovered. Animals received injections of buprenorphine post-surgery, as well as

ampicillin antibiotic for one week following the implantation.

Subjects

The device in this work has been designed and fabricated for both rats and mice. However, the protocols and technology may be amenable to various other species ranging from zebrafish to non-human primates. The optogenetic experiments can be performed on either transgenic or viral vector-injected subjects. All animal procedures described here were approved by the Institutional Animal Care and Use Committee (IACUC) at the University of Wisconsin-Madison and conform to US National Institutes of Health guidelines. The detailed surgical implantation protocols are described in appendix A2.

Impedance spectra and baseline signal recordings *in vivo*

Neural signals can be recorded from the chronically implanted electrode array at any

Table 1 | Number of *in vivo* experiments for each purpose

Implant description	*In vivo* vascular imaging	Impedance spectroscopy	Baseline signal recordings	Electrical evoked potentials	Optogenetic experiments
Rat CLEAR device (chronic)	3	4	4	4	—
Rat Pt micro ECoG device (chronic)	3	3	3	3	—
Mouse CLEAR device (terminal)	3	—	3	—	3
Mouse Pt micro ECoG device (terminal)	2	—	2	—	2

CLEAR, Carbon-layered Electrode Array; ECoG, electrocorticography.
Table 1 describes the number of devices that were implanted during this study and the experiments they were used for. Multiple rats were implanted bilaterally: one device on each brain hemisphere, to serve as better within-animal comparisons and to reduce total animals numbers used. Three rats were implanted bilaterally with one CLEAR micro-ECoG device and one platinum micro ECoG device and one rat was implanted with a single CLEAR device. All rats were chronic studies. Five mice were implanted during terminal procedures. Three animals had CLEAR and platinum micro ECoG devices implanted, and two had only the CLEAR device.

time with a corresponding electrophysiology recording system. Measuring the impedance of the implanted electrode array before recording neural signals is recommended, and can ensure credible electrophysiological data by allowing data collected from dead channels to be discarded. The implanted graphene neural electrode array has shown reliable impedance and recording ability for the entire period of implantation (up to 70 days)[52]. It is recommended that baseline neural signal data (awake or anesthetized) be recorded for at least three to five

minutes during each session, in order to average signals post-processing, and remove unwanted movement artifacts and external noise. Recordings can be taken from awake, sedated or anesthetized animals. Use of different sedatives and anesthetics can be an important tool for immobilization of the animal for testing, testing the electrode itself, and studying the impact of different conscious altering substances on neural signal activity. Isoflurane ablates almost all cortical neural activity at surgical levels, but at lower concentration levels allows for recording of deeper brain structures. Dexmeditomadine and ketamine allow for cortical recordings, albeit usually with frequency, amplitude, and latency shifts from awake signals. We obtain neural signal recordings using a Tucker-Davis Technologies (TDT) neurophysiology work system. Signals are recorded via a 32-channel active TDT headstage, plugged into a printed circuit board (PCB) connector. The signals are amplified via the headstage and TDT PZ2 amplifier before sending it to the TDT RZ2 system and the computer. We use custom TDT software to visualize neural signals in real-time as well as send out TTL pulses to the electrical stimulator and laser for cortical sensory evoked potential recordings.

Figure 2.17 shows recorded impedance and baseline power spectra, along with the recorded evoked potential.

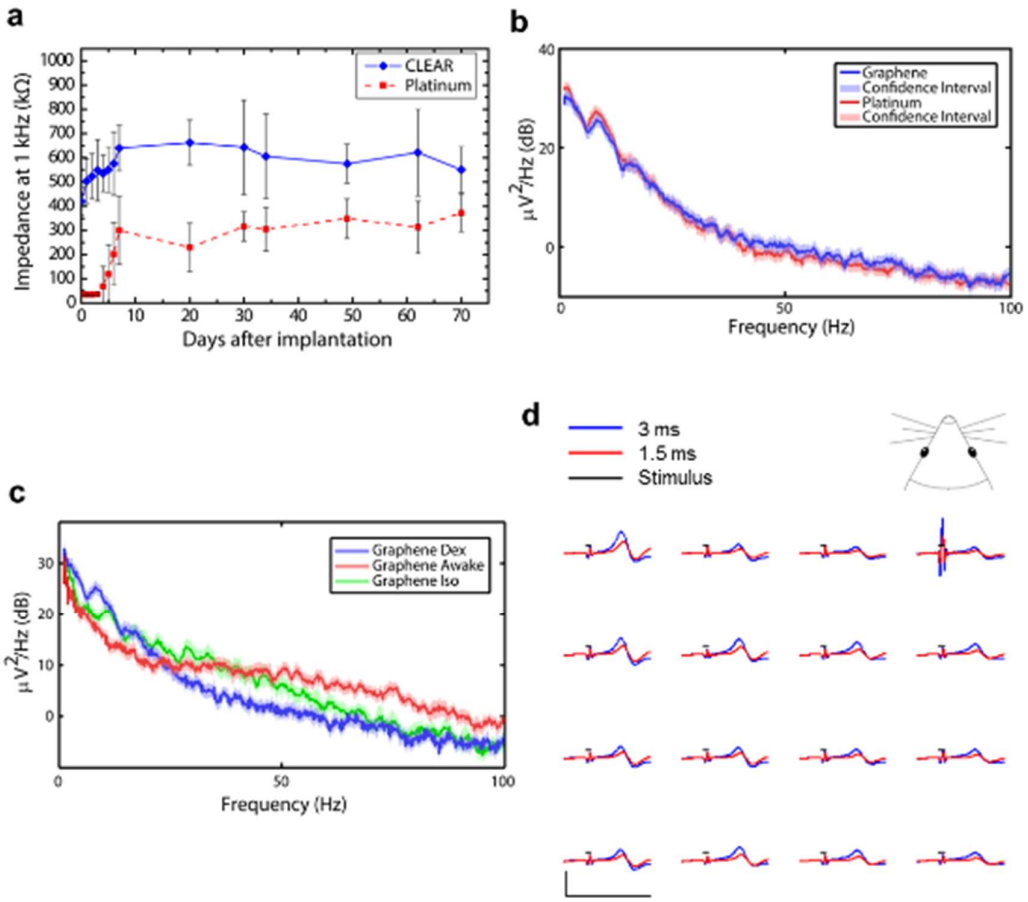

Figure 2.17 In vivo recorded signal characterizations. (a) Average longitudinal 1 kHz impedance values for CLEAR and platinum micro-ECoG devices implanted in the same animal. The error bar represents the standard deviation of impedance extracted from 16-channel measurement. (b) Baseline signal power spectra for the CLEAR and platinum devices under Dexmedetomidine with 95 % confidence interval using jackknife resampling. (c) Baseline signal power spectra for a CLEAR device under two analgesic conditions, Dexmedetomidine and Isoflurane, compared to an awake condition. (d) Sensory evoked potentials recorded by the CLEAR device, via electrical stimulation of the sciatic nerve on the hind leg of the rat, contralateral to the array. The device was implanted over somatosensory cortex. Stimuli were applied for 1 ms at 3 mA and 1.5 mA current levels. X-scale bar represents 50 ms, y-scale bar represents 100 μV.

In figure 2.17(a), both CLEAR and Pt devices experienced a steep rise in impedance

within the first 10 days after implantation, most likely due to the initial tissue response to the implanted arrays[62]. After this initial sharp increase, the impedances appear to have plateaued, with some minor day-to-day fluctuations. The shape of these impedance curves is characteristic of epidurally implanted micro-ECoG devices[41]. There was no statistically significant difference between the impedance changes for the CLEAR and platinum micro-ECoG devices over the entire implantation period, suggesting that the CLEAR device will perform as well as the platinum device over the explored time period.

Figure 2.17(b) shows power spectra for the baseline local field potentials recorded by single channels on the CLEAR and platinum micro-ECoG devices in the 1-100 Hz frequency range. As with the longitudinal impedance data, there is little difference between the signals recorded by the two different arrays. The 95 % confidence intervals for the CLEAR and platinum devices overlap suggesting little difference between the signals recorded by the different devices. This similarity is shown in the high frequency range (1-600 Hz) as well (Figure 2.18). Additionally, Figure 2.17(c) shows the baseline spectra obtained with the animals anesthetized using two different anesthetics, dexmedetomidine and isoflurane. Dexmedetomidine induces sleep-like rhythms, with more low frequency oscillations, while isoflurane suppresses general signal power, as shown in the figure. Both dexmedetomidine and isoflurane suppress high gamma -6 dB at 80 Hz, a 75 % reduction in amplitude compared to the awake condition. This suggests that clear electrodes are able to pick up the high-gamma signals that have been found to be useful for ECoG based brain-computer interface applications[73, 74].

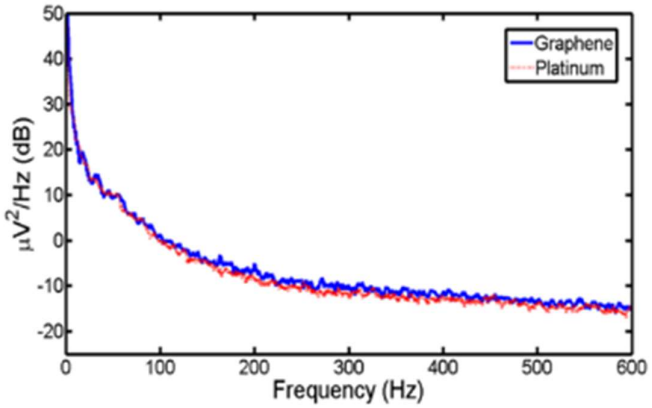

Figure 2.18 Power spectra for the baseline signals recorded by single channels on the CLEAR and platinum micro-ECoG devices in the 1-600 Hz frequency range (in vivo).

Electrically evoked potential

Electrically evoked local field potentials (LFPs) can be recorded using the graphene electrode array. The hindlimb (sciatic nerve) or forelimb (median nerve) of the animal can be electrically stimulated on the surface of the skin with stimuli containing various pulses. Sensory evoked potentials are expected to occur on the contralateral hemisphere from where the sciatic stimulation occurred due to the crossing of the neural pathways in the brainstem and spinal cord. Visual, barrel, and auditory cortex could all be recorded from as well. More experiments can be designed with the graphene electrode array, based on the capability of recording both spontaneous baseline activity and evoked neural signals over time.

In this experiment, the hindlimbs of the animals were stimulated with surface electrodes placed above and below the sciatic nerve. Stimuli consisted of 1 ms biphasic electrical pulses, with amplitudes varying from 1-3 mA. In specific, animals were anesthetized with dexmedetomidine hydrochloride (0.05 mg/kg, Orion Pharma), and their hindlimbs shaved. Two adhesive surface electrodes were attached to one leg at a time and held in place with tape. These electrodes were hooked up to a stimulation box (A-M Systems Isolated Pulse Stimulator,

Model 2100) linked to the TDT RZ2 system via a BNC cable. The animal's electrodes were plugged into the RZ2 system via the TDT headstage and PZ2 amplifier. In this way, an electrical stimulus was sent to the animal's sciatic nerve from the RZ2 system, and the response in the somatosensory cortex was recorded through the CLEAR device and sent back to the computer. After completion, the animals were recovered with an injection of atipamezole hydrochloride (0.3 mg/kg, Orion Pharma).

Figure 2.18(d) shows a summary of the evoked potential results for the contralateral implanted CLEAR device at two stimulation levels. The results show a clear neural response with approximately 100 μV evoked potentials. Signals recorded in the device with ipsilateral leg stimulation lacked the neural evoked potential that was found on the contralateral side (Figure 2.19). In general, the results displayed in Figure 2.18 and 2.19 show that the graphene electrode sites are capable of recording both spontaneous baseline activity and evoked neural signals with the same level of clarity as the platinum sites, and generally similar impedance behavior and stability over time.

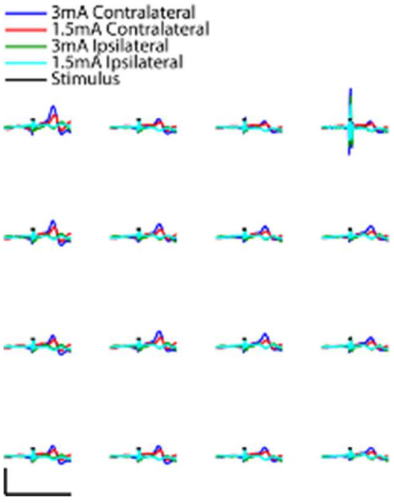

Figure 2.19 Sensory evoked potentials recorded by a CLEAR device, via electrical stimulation of the sciatic nerve on the hind leg of the rat, both contralateral and ipsilateral to the array. The device was implanted over somatosensory cortex. Stimuli were applied for 1 ms at 3 mA and 1.5 mA current levels. X-scale bar represents 50 ms, y-scale bar represents 100 μV.

2.5 Neural imaging: fluorescence imaging and optical coherent tomography

Various in vivo imaging methods can be combined to observe real time responses to optical or electrical stimuli, and to monitor corresponding tissue responses or vasculature changes through the transparent graphene electrode array. We have used fluorescent stereo microscopy and optical coherence tomography (OCT) to demonstrate the broad-wavelength transparency of the graphene neural electrode array[52]. Other in vivo imaging methods such as two-photon microscopy and confocal microscopy could potentially be combined with the graphene electrode technology. It is worth noting that differences in the refractive index may cause distortions and boundary artifacts depending on the imaging modality.

Fluorescence imaging

Imaging took place on a Leica MZ 16F stereoscope. Animals were anesthetized with a combination of isoflurane gas and dexmedetomidine hydrochloride (0.05 mg/kg, Orion Pharma), and kept on a heated water blanket. The animals' heads were stabilized to prevent breathing artifacts. Animals were injected with 12 mg/ml fluoresceine-isothiocyanate labeled dextran dissolved in phosphate-buffered saline to make the blood vessels fluorescent under blue light. Bright-field and fluorescent images were taken of the electrode arrays and surrounding brain tissue. Additionally, blood flow movie recordings were acquired using the light path of the Leica MZ 16F stereoscope in combination with the Sony HDR-SR11 high definition camcorder.

Representative images of the cortical vasculature through the CLEAR micro-ECoG device are shown in Figure 2.20. Images in the top row were taken in bright-field, while those on the bottom were taken under blue (470 nm) light with the aid of a tail vein injection of FITC-Dextran to fluorescently label the vasculature. These images demonstrate the clarity of the

graphene electrode sites and the ability to view the underlying cortex and cerebral vasculature through the CLEAR device. The electrode sites and traces are clearly visible in the images of a platinum micro-ECoG array.

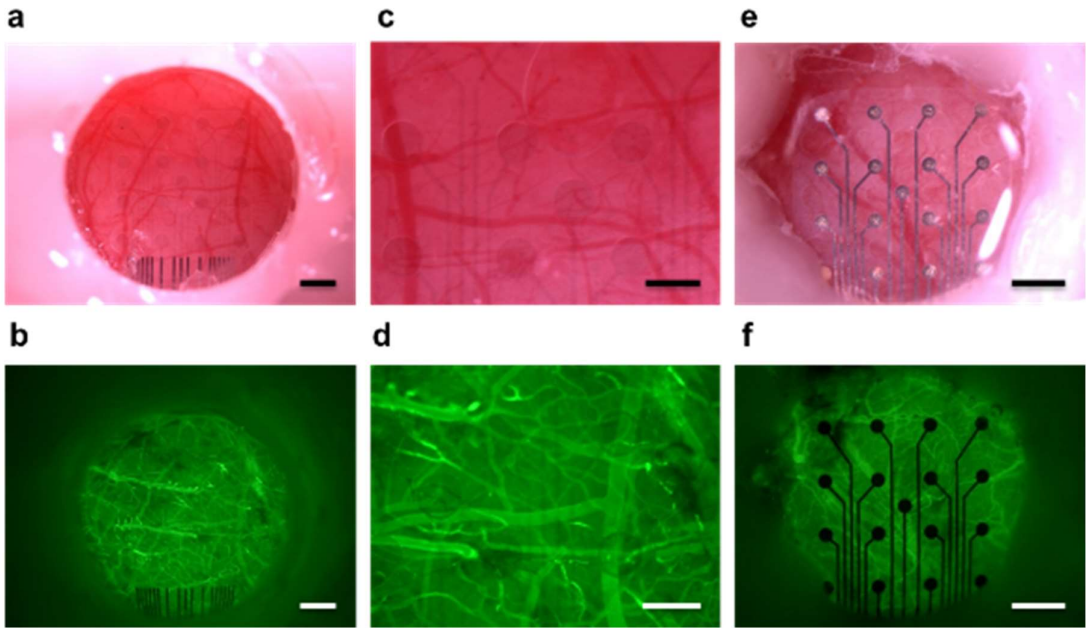

Figure 2.20 Representative in vivo images of the cortical vasculature seen. (a) Bright-field image of CLEAR device implanted on the cerebral cortex of a mouse beneath a cranial window. (b) Fluorescence image of same device shown in a. Mouse was given an intravenous injection of FITC-Dextran to fluorescently label the vasculature. (c) and (d) Higher magnification bright-field and fluorescence images of same device shown in a and b, respectively. (e) and (f) Bright-field and fluorescence images of standard rat-sized micro-ECoG arrays with platinum electrode sites, respectively. Scale bars in a-d represent 250 μm, while scale bars in e and f represent 750 μm. In vivo vasculature imaging was repeated in three rats, each with a CLEAR and platinum microECoG array.

Optical coherence tomography (OCT)

This work was done with a collaboration with Prof. Ramin Pashaie, Farid Atry, Seth T. Frye at the University of Wisconsin-Milwaukee. A custom Spectral Domain Optical Coherence Tomography (SD-OCT) system was used to obtain 3D OCT angiograms and velocity profiles.

The SD-OCT system utilized a light source at the central wavelength of 1300 nm and spectral bandwidth of 200 nm, delivering 10 mW of optical power at the tip of a single mode fiber. The system provides 5 μm axial and 4 μm lateral resolution with a 10x telecentric lens[75].

The cross-sectional OCT angiograms were obtained by recording 10 OCT B-scans at each cross section and employing a phase sensitive angiography technique to the OCT data[75]. For the field of view of 2.8×2.8 mm^2 650 cross-sectional angiograms were obtained while each one consisted of 650 lateral positions. For the field of view of 1.1×1.1 mm^2 the number of cross sections and the number of lateral positions were 500. After stacking all cross-sectional angiograms to form the volume angiogram, a 3D blurring kernel was applied to reduce the noise, and then the 2D maximum intensity projection (MIP) of the angiograms was obtained. Adaptive histogram equalization (MATLAB and Image processing toolbox Release 2012b, The MathWorks, Inc., Natick, Massachusetts, United States) was applied to improve the contrast of MIP images. For 3D visualization purposes, contrast enhancement and vessel de-shadowing was performed by applying a biased sigmoid nonlinear transform to the intensity of 3D angiography data. The bias of the sigmoid function was defined to value at which this function has a value of 0.5. At each point the bias of the sigmoid function was determined according to the angiogram values above it.

For blood velocity measurement, the tissue was scanned at 3500 (FOV=2.8×2.8 mm^2) or 2000 (FOV=1.1×1.1 mm^2) A-scans per cross section. The scans were performed at 500 tissue cross sections and rate of 40,000 A-scans per second. At each position the Doppler shift introduced by the moving particles was estimated by calculating the average power spectrum density of a signal consisting of 7 consecutive OCT signals at that position (ω_a). Axial velocity at that depth was then calculated by v=(4×10^4*ω_a⁄2π)[75].

The OCT imaging demonstrates the ability of the CLEAR device based on its high

transparency in the IR spectral range. Figure 2.21 shows the structure of the cerebral vasculature captured as a 3D OCT angiogram[76-78] through the device. Furthermore, two typical velocity profiles[79-82] of blood flow below the CLEAR device are demonstrated in Figure 2.21(b) and (d). In these images, dark lines produced by the gold traces are visible on the right side, however, the center of the array is clear with no dark lines and vessels are easily visible. Figure 2.21(e) shows a typical cross-sectional angiogram after contrast enhancement under the CLEAR device. The OCT system is able to detect the vessels under electrode sites and electrode traces. The 3D visualization of the angiography data is presented in Figure 2.21(f). The structural data is shown with gray and vessels with red. Similar data for the platinum device is shown in Figures 2.21(g)-(j) indicating the opaqueness of the platinum electrode sites. The comparison shows the advantage of the CLEAR device over the conventional platinum device. It is important to note that OCT utilizes infrared light wavelengths, which may create artifacts with ITO-based devices, depending on the fabrication process.

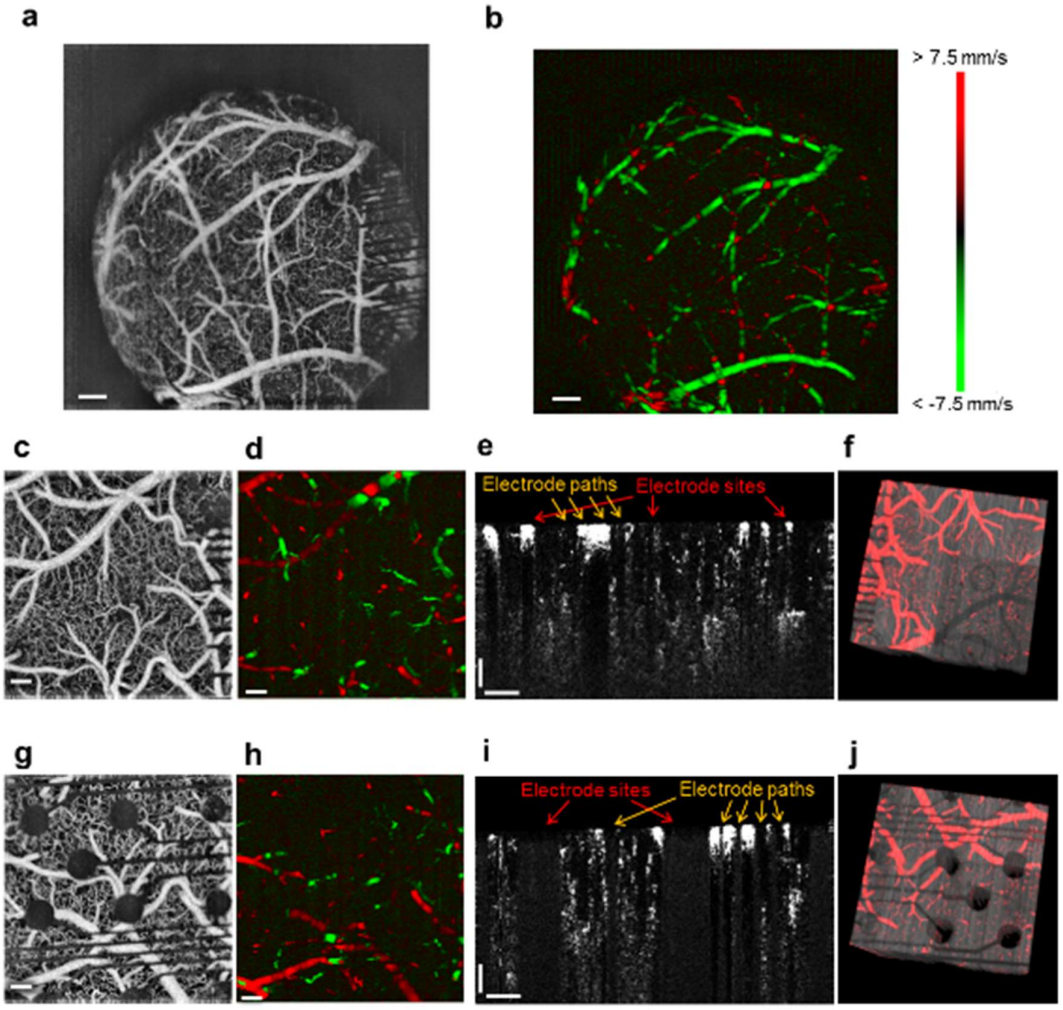

Figure 2.21 Optical coherence tomography through CLEAR and platinum devices. (a) and (c) Maximum intensity projection (MIP) of OCT angiogram showing cortical vasculature visible through the CLEAR micro-ECoG device (FOV 2.8×2.8 mm^2 and 1.1×1.1 mm^2, respectively). (b) and (d) Doppler blood flow velocity image showing the directionality of blood flowing through the vasculature below the CLEAR device (FOV 2.8×2.8 mm^2 and 1.1×1.1 mm^2). Red color represents blood flowing towards the lens and green color represents blood flowing away. (e) Cross-sectional angiogram after contrast enhancement and de-shadowing (CLEAR device) (f) 3D visualization of the vasculature (red color) overlaid on the structural data (gray) (CLEAR device). (g) MIP of angiogram through a platinum micro-ECoG device, (h) Corresponding Doppler blood flow velocity measurements, (i) Corresponding cross-sectional angiogram, and (j) Corresponding 3D visualization of vessel structure for a micro-ECoG array with platinum electrode sites.

2.6 Optogenetic experiment

Optogenetics with CLEAR

Previously impossible optogenetic experiments can be performed with the transparent graphene neural electrode array, including optical stimulation directly under the electrode sites. Observation of biological responses to light stimuli such as vascular diameter, blood flow, morphological changes, microglia and astrocyte reactions, and collagen formation, through the transparent electrode site, while recording the neural response could give us new insight on the brain's complex immune system function. An optical stimulus can be applied with an external light source (optical fiber with laser) or with an integrated light source (light emitting diode, LED).

We used an optical fiber attached to a laser to activate neurons in transgenic Thy1::ChR2 mice. These mice have neurons expressing the Channelrhodopsin-2 protein, making them susceptible to excitation when exposed to blue (460-470 nm) light. The anesthesia was switched from isoflurane, which inhibits neural signaling, to a combination of ketamine (75 mg/kg) and dexmedetomidine (25 μg/kg). High intensity blue light, with a maximum power of 63.7 mW/mm^2, was then directed onto various regions of the brain, through the CLEAR device (Figure 2.22), while simultaneously recording the neural response to the optical stimulation. Once experimentation was complete, the animals were euthanized with an intraperitoneal injection of Fatal PLUS pentobarbitol solution, and a control experiment was conducted.

The average evoked response is shown for three different light intensity stimulation levels in Figure 2.22(c). The stimulus time was 3 ms. The initial peak corresponds to the expected stimulus artifact, and the second, longer peak is the evoked neural response. The stimulus artifact peak is detected approximately 3 ms after the stimulus onset, while the evoked

neural response peak has latency approximately 7.7 ms following the stimulus onset. These latencies are highly dependent on the details of the eventual intended experimental requirements (i.e. light intensity, stimulus duration, interstimulus interval). This leads to the logical consequence that in many experimental paradigms the stimulus artifact will be completely distinguishable from the evoked neural response, and in others there may be considerable overlap.

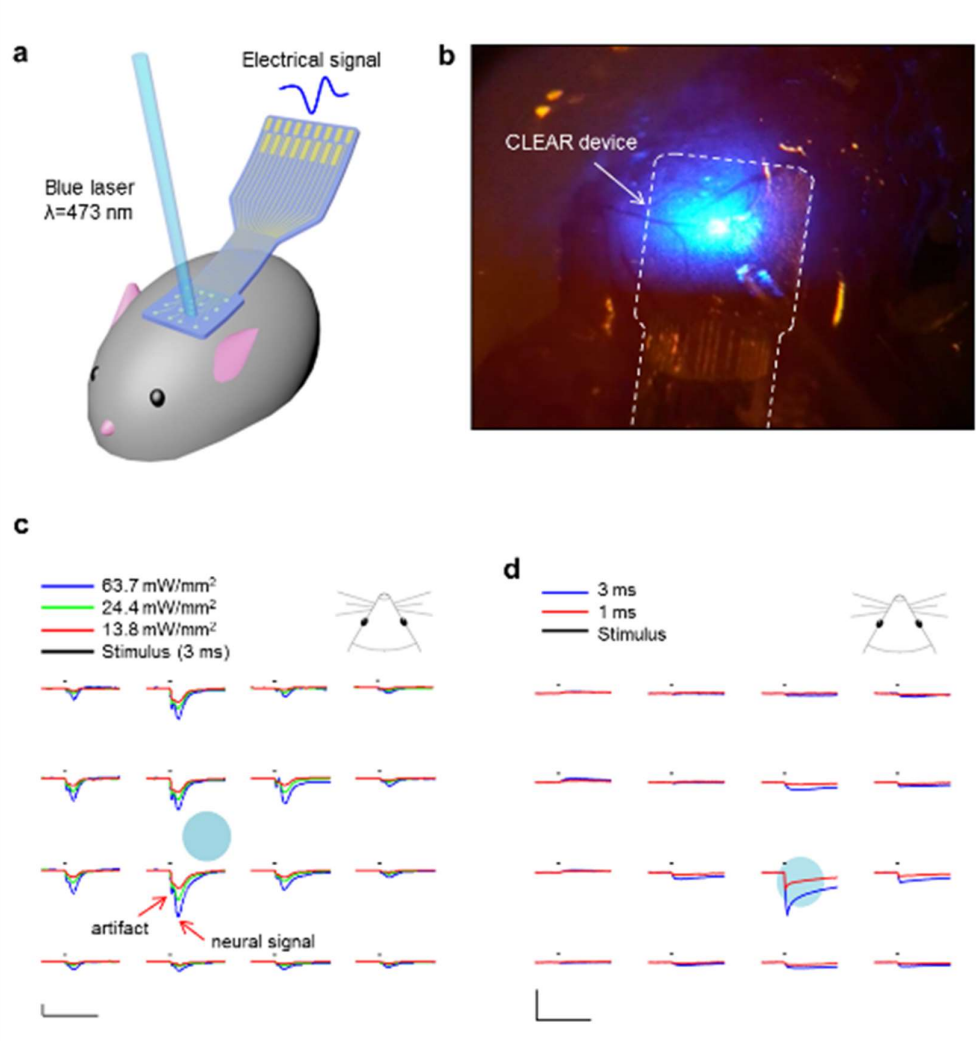

Figure 2.22 Optogenetic experimentation through the transparent CLEAR device. (a) Schematic drawing of opto-experimental setup, showing the CLEAR device implanted on the cerebral cortex of a mouse, with an optical fiber delivering blue light stimuli to the

neural cells. (b) Image of a blue light stimulus being delivered via an optical fiber, through the CLEAR device implanted on the cortex of a Thy1::ChR2 mouse. (c) Optical evoked potentials recorded by the CLEAR device. X-scale bars represent 50 ms, y-scale bars represent 100 μV. (d) Post-mortem control data with the laser set at 24.4 mW/mm^2 with the light impingent on electrode site 11 of the CLEAR device. X-scale bars represent 50 ms, y-scale bars represent 100μV.

Once experimentation was complete, the animals were euthanized and a control experiment was conducted with the CLEAR micro-ECoG array placed on the somatosensory cortex of the euthanized animal to verify that the signals recorded were from neurons affected by the light stimulation and not due to the artifact. From Figure 2.22(d) we can see that the signals obtained from the post-mortem control experiment are different from the signals recorded from the living animal both temporally and according to amplitude of the negative peaks. These results demonstrate that the signals in Figure 2.22(c) were evoked neural responses to the light stimulation.

A smaller diameter optical fiber than that of the electrode site can be used to stimulate the neurons directly below the transparent electrode site (Figure 2.23). Varying the amount of blue light stimulation can correspondingly vary the level of neuronal response to the stimulus. The transparent graphene electrode array may allow a larger amount of light through the site compared to other transparent conductive materials. When using opaque materials, only the tissue surrounding the electrode sites can be stimulated, limiting the ability to carry out high-resolution optogenetic experiments under the electrode. When a large-area full-field light is applied, the graphene electrode array can allow the highest and the most efficient light stimulus because the electrodes do not block as much light (~90 % light transmission). Thus the highly transparent graphene electrode array enables additional potential experiments to be performed.

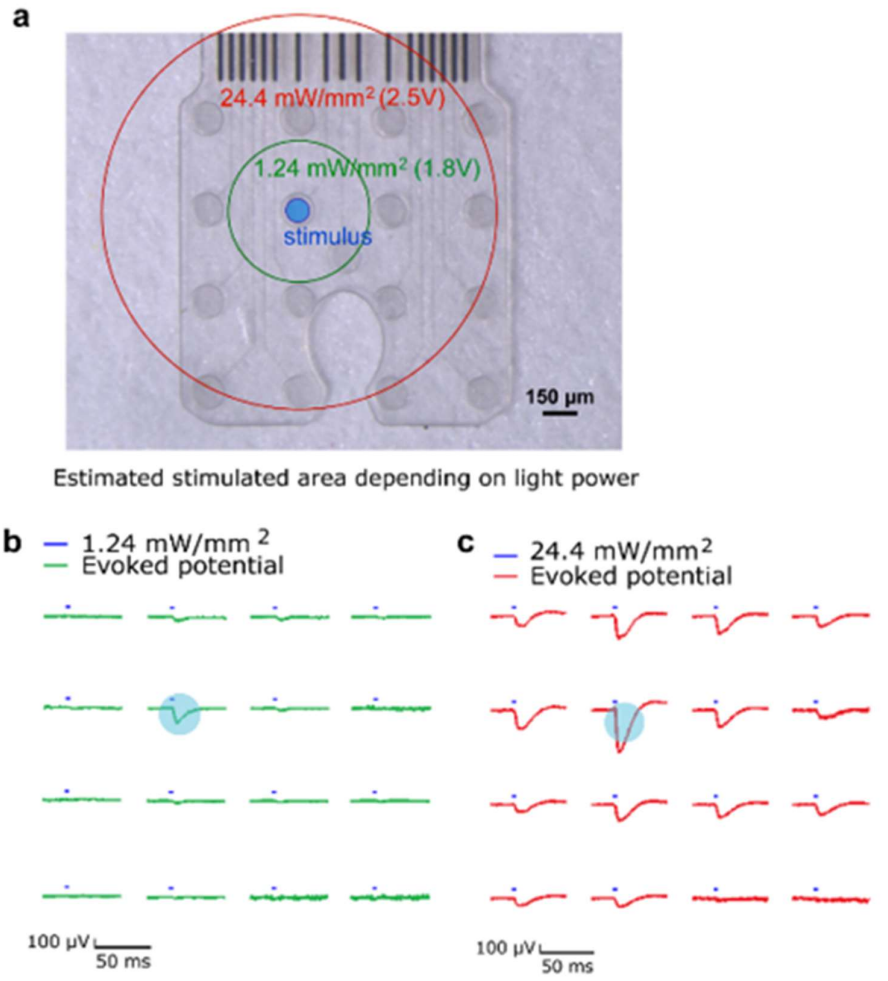

Figure 2.23 Optogenetic experiments in a Thy1::ChR2 mouse with varying optical stimulation power. (a) An optical fiber located above a transparent graphene electrode site produced a light stimulus and an estimation of corresponding stimulated neural tissue area beneath is shown dependent on incident light power (1.24 versus 24.4 mW/mm^2). (b) Evoked potentials from 1.24 mW/mm^2 light stimulus. The spatially localized and small evoked potential (~100 µV) is attributed to the relatively small stimulus activated neurons in a small spatial area. (c) Evoked potential from 24.4 mW/mm^2 light stimulus. The broader and larger evoked potential (~500 µV) is attributed to the neurons activated in a broader and deeper area (i.e. larger volume).

It should be noted that there are a number of potential sources of variability when stimulating ChR2 (or other optogenetic constructs) from the cortical surface. For example, in the experiment described in Figure 2.23, the ChR2 was expressed under the control of the Thy1

promoter, which is predominantly expressed in the layer 5 pyramidal cells in the cortex[83]. These cells have apical dendritic arbors that extend near the cortical surface, which are preferentially stimulated at low light levels, with deeper cell compartments recruited with increasing light levels[84]. Stimulation from the surface of the cortex, while fundamentally more convenient than stimulating with a penetrating fiber, does come with a number of caveats that should be considered when deciding whether it is a suitable for a given application. There are a number of studies that have both experimentally and theoretically addressed these issues and can be referenced for estimations of the effect of a number of different physical and biological parameters that may lead to variability in light stimulation levels in the cortex[83-85]. There are also some recent tools that have been developed to help estimate the effects of light propagation in the brain[86]. There is also a small amount of light loss through the graphene electrodes and traces (~10 %) which also should be factored into the overall estimation of optical activation needs of any particular experimental application.

2.7 Applications of CLEAR technology

The use of the transparent graphene neural electrode array is not limited to epidural or cortical placement. The CLEAR technology is amenable to fabrication and testing of a multitude of other electrode arrays used in biological research such as **penetrating neural electrode** arrays to study deep brain (Figure 2.24). An array can be placed anywhere within the brain when combined with insertion techniques such as pairing with an optical fiber or a releasable injection needle[87, 88]. Furthermore, applications of graphene technology are not only limited to the central nervous system (CNS), but could be easily translatable to any device interfacing with an electrical biological system, such as the peripheral nervous system (PNS), visual, muscular, or cardiovascular systems.

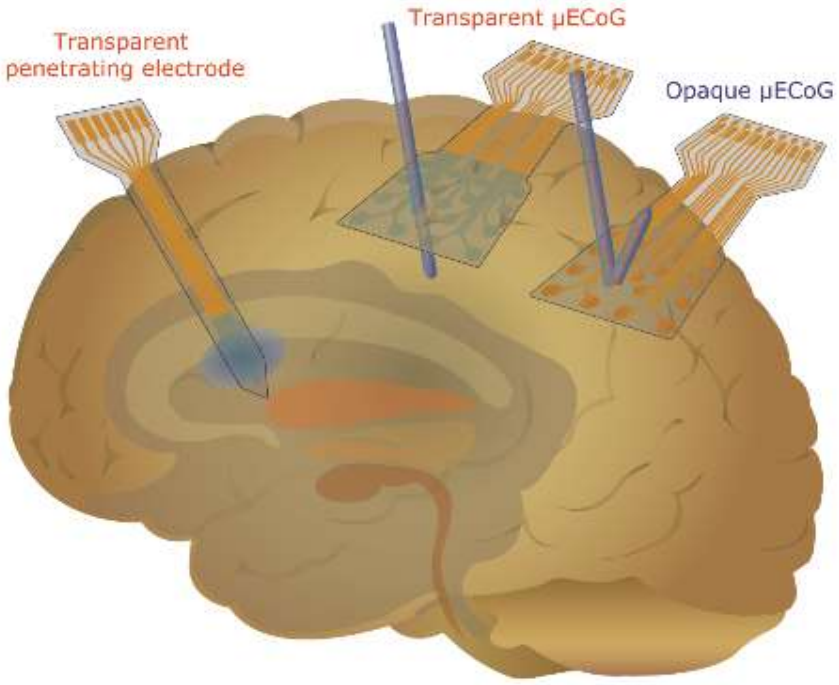

Figure 2.24 Utility of a transparent graphene neural electrode array. A transparent μECoG and an opaque μECoG are drawn showing the different light transmittance. A transparent penetrating electrode is drawn showing the full-field optical stimulation. e monitoring during optical or The graphene-based transparent electrodes can utilize see-through imaging which enables tissue responselectrical stimulation or electrical recording. Full-field optical stimulation is possible, providing possibilities for unique optogenetic experiments.

Basic biological work in the PNS could be done with transparent graphene electrodes, similarly to work being done in the brain. Simultaneous imaging of calcium signals and cells incorporated in the brain's immune responses could yield important information in the study of wound healing. The advent of neural prosthetic systems in the CNS or PNS may someday pair with optogenetics, and necessitate the need for conductive, yet transparent, electrode sites. For peripheral optogenetic systems, nerve cuff arrays may need to be patterned with graphene so that proximal nerve signals can be recorded and sent to a device for interpretation, and distal nerve sites stimulated either optically or electrically through the same site, creating a closed-loop system.

Graphene **multi-electrode electroretinogram (meERG)** is one example of how this technology can be used in the visual system. meERG arrays detect and record electrical responses from retinal cells[89-91]. The graphene-based transparent meERG may be able to record larger amplitude signals, due to the larger area of incident light stimulus compared with that of the opaque metal meERG that will block the light at each electrode site. The demonstration of graphene meERG is presented in chapter 4.

The utility of the transparent graphene electrode arrays may be further applied to muscle tissue for **electromyography (EMG)**, and to the heart for **electrocardiography (ECG)**. These devices would allow us to record the electrical activity of these organs while simultaneously performing imaging experiments. These and previously mentioned biological systems can be explored in depth with the clear graphene electrode such that a full-field view of the area can be reconstructed, versus missing important data points hidden behind opaque metal arrays.

Multi-electrode arrays (MEAs) built for in vitro testing, such as neural pathfinding in cell culture and neural tissue slice electrophysiology, can also be employed with the transparent graphene electrode array providing better visualization of cells during imaging and recording. Imaging becomes an important tool for visually inspecting the morphology, growth direction, and growth rate of cells, all of which are more easily visible through the graphene array versus other metal arrays.

Clinically implantable devices may also be improved by applying transparent graphene electrode technology. A transparent electrocorticography array would allow an unimpeded view of the brain below the electrodes, improving the ability of the implanting surgeon to identify anatomic landmarks needed for the accurate placement of the array, and also ensuring easy visualization of any injury to the cortical surface that may require treatment prior to final

implantation of the electrodes.

Carbon nanotube yarn depth electrodes have demonstrated markedly reduced magnetic resonance imaging (MRI) artifact over the traditional platinum-iridium (Pt-Ir) electrodes in vivo, suggesting that depth electrodes constructed using graphene may also significantly reduce MRI artifact[92]. The magnetic susceptibility difference between the carbon-based ultrathin graphene electrodes and the adjacent tissue would be less than the difference between metal electrodes and the adjacent tissue, likely resulting in less MRI artifact[93]. Decreased MRI artifact would be particularly useful for deep brain stimulation (DBS) electrode implantation, where sub-millimetric anatomic accuracy is required. Graphene electrodes would also likely have less imaging artifact on computerized axial tomography (CT) than metal electrodes, since higher atomic number materials, such as Pt-Ir, cause greater polychromatic x-ray beam hardening and scatter, and thus worse CT image artifact[94]. The theoretical MRI and CT imaging benefits of graphene electrodes versus metal electrodes remains to be confirmed experimentally.

Chapter 3. Evaluation of CLEAR electrodes for electrical stimulation

3.1 Introduction

Transparent graphene neural electrode arrays have shown their ability to electrophysiology, in vivo imaging, and optogenetic applications as described in chapter 2. However, electrical stimulation with the graphene electrodes requires additional impedance study and *in vivo* validations. Electrical stimulation can be another key usage of the graphene electrodes for the treatment of neuronal disorders such as Parkinson's disease. In order to understand the working mechanism of the graphene electrodes and expand their utility, the evaluation results of the graphene electrode arrays and its demonstration to the electrical stimulation in GCaMP6 mice are presented. In specific, electrochemical impedance spectroscopy (EIS) and cyclic voltammetry (CV) were studied for a number of graphene electrode sites with varying electrode dimensions. A representative equivalent circuit model and its parameters were extracted to show the charge carrying mechanism of graphene electrodes. Based on the evaluation, electrical stimulation was performed in GCaMP6 mice with fluorescence imaging and optical coherence tomography (OCT). It was observed that the graphene electrodes with the diameter between 100 and 200 μm (7854 and 31416 μm^2 in area) have average impedance between 286. 4 and 215.7 kΩ at 1 kHz. The main charge carrying mechanism of graphene electrode was found to be capacitive but it varied depending on frequency. In vitro and in vivo test results showed that the graphene electrode with a dimeter of 200 μm can allow the current up to 300 μA. Electrical stimulation in GCaMP6 mice provided real-time observation of the stimulated area directly underneath the transparent graphene electrode, including the spatial response to different electrical stimulation levels. The results

suggest that the transparent graphene electrode arrays can be utilized for electrical stimulation, providing the ability to correlate the stimulation and visual observation in vivo.

3.2 Electrochemical impedance spectroscopy (EIS)

Method

The EIS was performed with the transparent graphene electrode arrays with different electrode diameters of 100 μm, 150 μm, and 200 μm. The corresponding areas are 7854 μm^2, 17671 μm^2, and 31416 μm^2. The measurement was performed using three electrodes system: working electrode (WE), counter electrode (CE), and reference electrode (RE). The graphene electrodes, a large platinum electrode, and a silver/silver chloride (Ag/AgCl) were used as WE, CE, and RE, respectively. Input sine waves with 10 mV rms (root mean square) and varying frequencies from 1 to 100 kHz (26 steps) were applied using a potential/galvano stat (PGSTAT 128N, Autolab). Each electrode array was connected to the PGSTAT via a zero insertion force (ZIF) printed circuit board (PCB), a 32-channel passive Tucker-Davis Technologies (TDT) headstage, and a multiplexer. The recorded impedances were plotted in three formats: Nyquist plot (-X vs R), impedance versus frequency (Z vs f), and phase versus frequency (-Phase vs f). The impedance of each electrode channel at 1 kHz were plotted in an impedance versus electrode area graph. Equivalent circuit modeling was performed and the parameters of the circuits were extracted.

Measurement results

Figure 3.1 shows representative impedance plots for good and dead channels. Good channels normally have 100-500 kohm and dead channels have more than 2 Mohm at 1 kHz. The 1 kHz is known as a common benchmark frequency in the area of neural electrodes because the intensity of neural response (action potential) tends to be peaked in 1 msec after stimulus

[62, 63]. The impedance trend depending on the frequency can be explained by the equivalent circuit of the electrode in the measurement system. The equivalent circuit model is presented in figure 3.2 with four elements: constant phase element impedance (Z_{CPE}), charge transfer resistance (R_{CT}) (or polarization resistance (R_p)), solution resistance (R_S), and Warburg impedance (Z_W). The total impedance of the equivalent circuit can be calculated with the equation 3.1

$$Z(\omega) = R_S + \{Z_{C_d} || (R_p + Z_W)\} \quad \text{--------- equation 3.1}$$

Where $Z_{C_d} = \frac{1}{j\omega C_d}$, $Z_W = \left(\frac{2}{\omega}\right)^{\frac{1}{2}} \sigma$, and σ is Warburg coefficient

$$\sigma = \frac{RT}{\sqrt{2}n^2F^2A}\left(\frac{1}{D_O^{1/2}C_O(x,t)} + \frac{1}{D_R^{1/2}C_R(x,t)}\right)$$

Where A is the electrode area, Cs are concentrations of subscripted species at a distance x from the electrode surface, and t is time.

Equation 3.2 shows the total impedance expressed in real and imaginary terms.

$$Z(\omega) = R_s + \frac{R_p + \sigma\omega^{-1/2}}{\sigma\omega^{1/2}(C_d+1)^2 + \omega^2 C_d^2 (R_p + \sigma\omega^{-1/2})^2} + j\frac{[\omega C_d (R_p + \sigma\omega^{-1/2})^2 + \sigma\omega^{-1/2}(C_d\sigma\omega^{1/2}+1)]}{(C_d\sigma\omega^{1/2}+1)^2 + \omega^2 C_d^2 (R_p + \sigma\omega^{-1/2})^2}. \quad \text{--------- equation 3.2}$$

For simplicity, the Z_{CPE} was replaced to C_d which is known as double layer capacitance. The electrical double layer is formed at the electrode and electrolyte interface. When the ions in solution approach the electrode surface, charges in the electrode are separated from the charges of these ions by a monolayer of polarized solvent molecules. Ideally, the double layer

capacitance (C_d) is constant assuming that the surface under investigation is homogeneous. In reality, however, the homogeneity lacks in the electrode surface so the CPE reflects more accurate condition. The impedance of CPE ($Z_{CPE} = \frac{1}{Y_0(j\omega)^n}$) varies depending on various factors such as surface condition. Y_0 is the admittance of an ideal capacitance, n is an empirical constant. When n=1, the CPE behaves as a pure capacitance. When n=0, the CPE behaves as a pure resistor. When n=0.5, the CPE behaves as a Warburg element with a constant phase of 45°.

At high frequency the equation 3.2 can be simplified as the equation 3.3.

$$Z(\omega) = R_s + \frac{R_p}{1+\omega^2 R_p^2 C_d^2} - j\frac{\omega R_p^2 C_d}{1+\omega^2 R_p^2 C_d^2} = Z'(\omega) - jZ''(\omega),$$ ---------- equation 3.3

When omega (w) is infinite,

$$Z(w) = Rs$$ ---------- equation 3.4

At low frequency the equation 3.2 is simplified as the equation 3.5.

$$Z(\omega) = R_s + R_p + \sigma\omega^{-1/2} - j(\sigma\omega^{-1/2} + 2\sigma^2 C_d).$$ ---------- equation 3.5

When omega (w) is 0,

$$Z(w) = R_S + R_P$$ ---------- equation 3.6

As can be seen in the equation 3.4 and 3.6, the impedance is higher at low frequency and it decreases as the frequency increases.

The phase vs frequency, and Nyquist plots in figure 3.1 also show the difference between good and dead channels. Good channels are mainly capacitive with phase of larger than 60° under 1 kHz. Reactance and resistance are smaller in good channels.

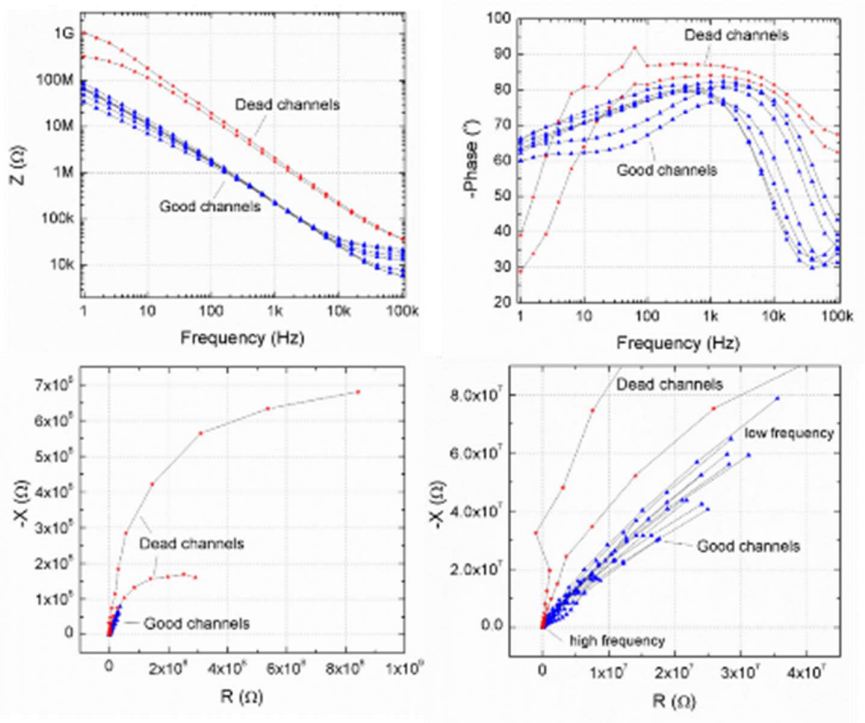

Figure 3.1 Representative impedance plots

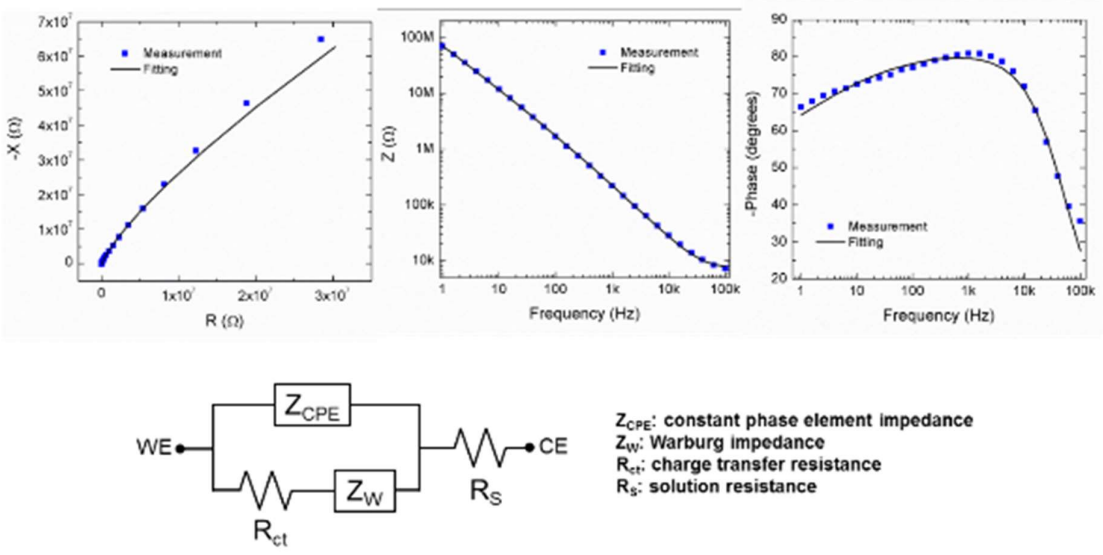

Figure 3.2 Equivalent circuit modeling of CLEAR device

Figure 3.2 shows the equivalent circuit modeling of CLEAR device. The modeling was performed using the NOVA software (Autolab). The measurement and fitting result

matches well with the four elements equivalent circuit, and the extracted parameters are presented below. It is shown that the CPE behaves more like capacitor as the n value of 0.918 is close to 1. The parameters of the graphene electrode have similar trends to the previously reported parameters of platinum electrodes considering their relative area differences. The results suggest that the charge carrying mechanism of graphene electrodes are similar to that of conventional metal electrodes.

	Q $[S \cdot s^n]$	**n**	R_{ct} $[\Omega]$	R_s $[\Omega]$	Z_w $[S \cdot s^{1/2}]$
Graphene (31416 um^2) [This work]	1.42×10^{-9}	0.918	1.07×10^{6}	5.92×10^{3}	2.97×10^{-9}
Pt (1 cm^2) [Franks et al.]	2.72×10^{-5}	0.92	4.48×10^{5}	28.0	-
Pt black (900 um^2) [Franks et al.]	0.86×10^{-9}	0.86	2.70×10^{9}	7.38×10^{3}	-

Figure 3.3 shows the impedance at 1 kHz for three different electrode areas. Most of the good channels have the impedance between 100 to 600 kohm and the dead channels have larger than 1 Mohm. Neural recording with the good channels brought smoother signals compared to the dead channels. The signal quality recorded with the 100-600 kohm channels were virtually identical, while the signals with larger than 1 Mohm channels were noisy. It is worth noting that the signal quality with 1-2 Mohm was somewhat tolerable so the channels could be used for some applications. The average impedance for 7854 μm^2, 17671 μm^2, and 31416 μm^2 were 286.4 kohm, 248.7 kohm, and 215.7 kohm, respectively. As the size of electrode increases the impedance value decreases slightly. However, the impedance deviation was not considerably different.

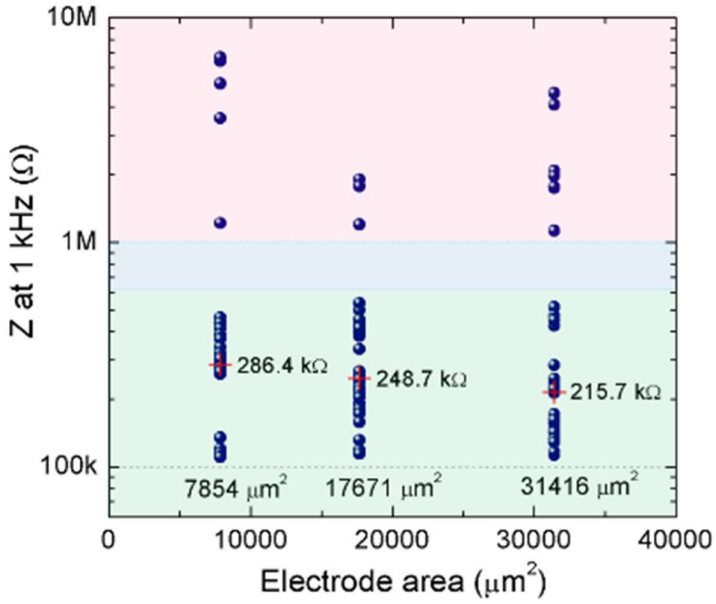

Figure 3.3 Impedance at 1 kHz versus electrode size

3.3 Cyclic voltammetry (CV)

Method

The CV was performed with the same PGSTAT 128N in the three electrodes system. The voltage was swept from -0.6 to 0.8 V with a scan rate of 1V/s. In order to get a stabilized CV, the voltage sweep was performed three times consecutively and the last sweep cycle was plotted in the graph. The scan rate dependency was studied varying the scan rate from 10 mV/s to 1 V/s.

Measurement results

Figure 3.4 shows the representative CV of good and dead graphene channels. Maximum amount of current flows normally when the voltage is minimum (-0.6 V). The maximum current level of good channels was above 1e-8 A and sometime more than 1e-7 A

for the low impedance channels. Dead channels usually have less than 1e-8 A or nearly zero.

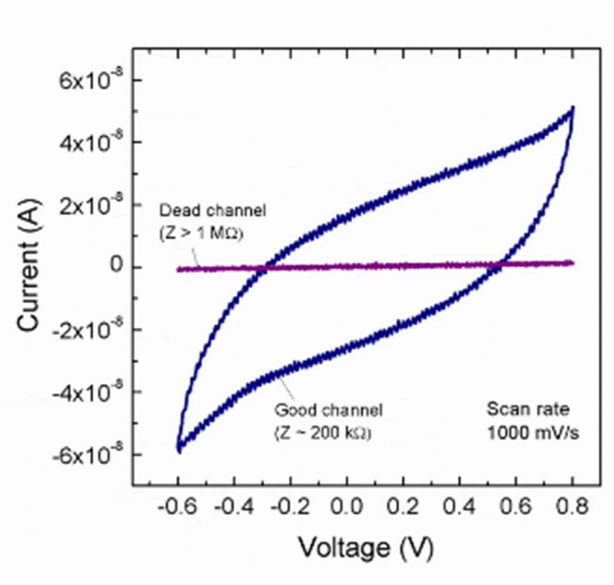

Figure 3.4 Representative CV of good and dead graphene channels

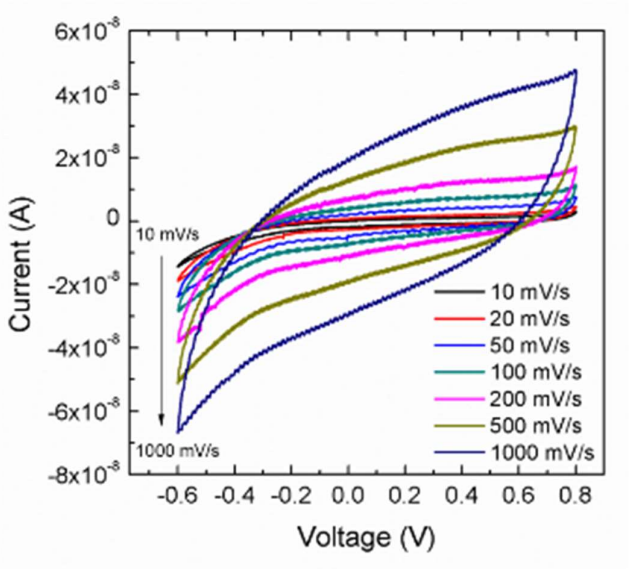

Figure 3.5 Scan rate dependency of CV

Figure 3.4 shows the scan rate dependency of CV. It is shown that the maximum current was higher in faster scan rate, which can be explained as follows: In a slow voltage scan the diffusion layer will grow much further from the electrode in comparison to a fast scan.

The flux to the electrode surface is considerably smaller at slow scan rates that makes the current flow smaller.

3.4 Electrical stimulation in GCaMP6f mouse

In vitro allowing current test

In order to estimate the maximum allowing current for CLEAR device, a test was performed in saline. Figure 3.6 shows the impedance change before and after the electrical stimulation in saline. All the channels with 10 μA and 50 μA didn't show any significant impedance change. However, some channels with 100 μA and 200 μA showed dramatic impedance increase after stimulation which indicates the damage on the channel. It is worth noting that some channels didn't show the impedance change meaning the graphene channels could allow 100 μA or 200 μA depending on the condition of electrodes. The initial condition would be related to the defect on the graphene. More studies on the origin of defect will be required in the future.

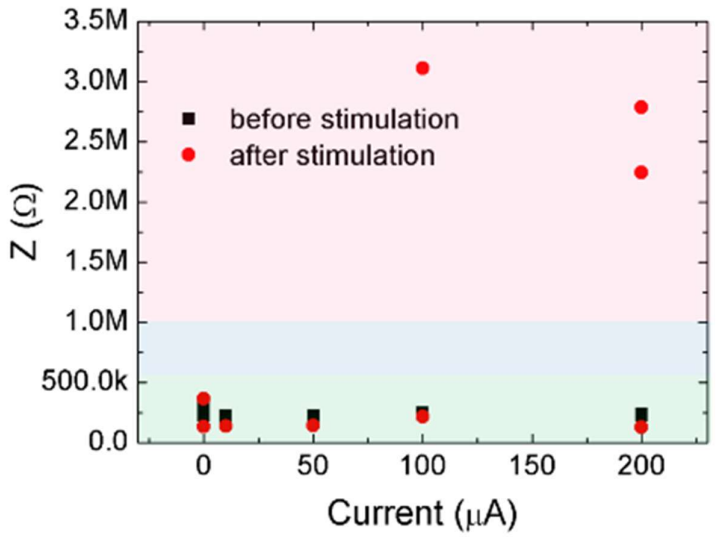

Figure 3.6 Impedance change before and after electrical stimulation in saline

Electrical stimulation in a GCaMP6f mouse

Based on the in vitro test above, in vivo electrical stimulation was performed in GCaMP6f mice. Figure 3.7 shows the implanted CLEAR and Pt device on GCaMP6f mice. The GCaMP6f proteins in the transgenic mice generate fluorescence when the modified cells get electrical stimulation. It is clear shown that the CLEAR device give much clearer images without significant visual loss. Simultaneous stimulation and observation was possible through the transparent graphene electrode. Various current level from 50 μA to 300 μA were applied through one electrode channel. The biphasic current was applied for 205 μsec for each current level. The interval of electrical stimulation was in-between 3 to 5 sec and it was applied randomly to avoid animal's adaptation to regular stimulus. The temporal response to 100 μA is shown in figure 3.7 with 200 msec interval. They show full-field images for the electrical stimulation which is promising for various future studies. For instance, studies of blood flow change and vasculature expansion with the electrical stimulation could be performed. The OCT images for different current level are also shown in figure 3.7. The spatial responses were seen with negligible artifact. It is worth noting that the graphene electrode allowed upto 300 μA for one-time stimulation. After the one-time stimulation the channel was dead. However, it is important to know that the graphene electrode could allow the electrical stimulation with 100-200 μA current level. This result corresponds to the in vitro test result in the previous section. It is expected that more interesting studies will follow using the uniqueness of the graphene electrodes.

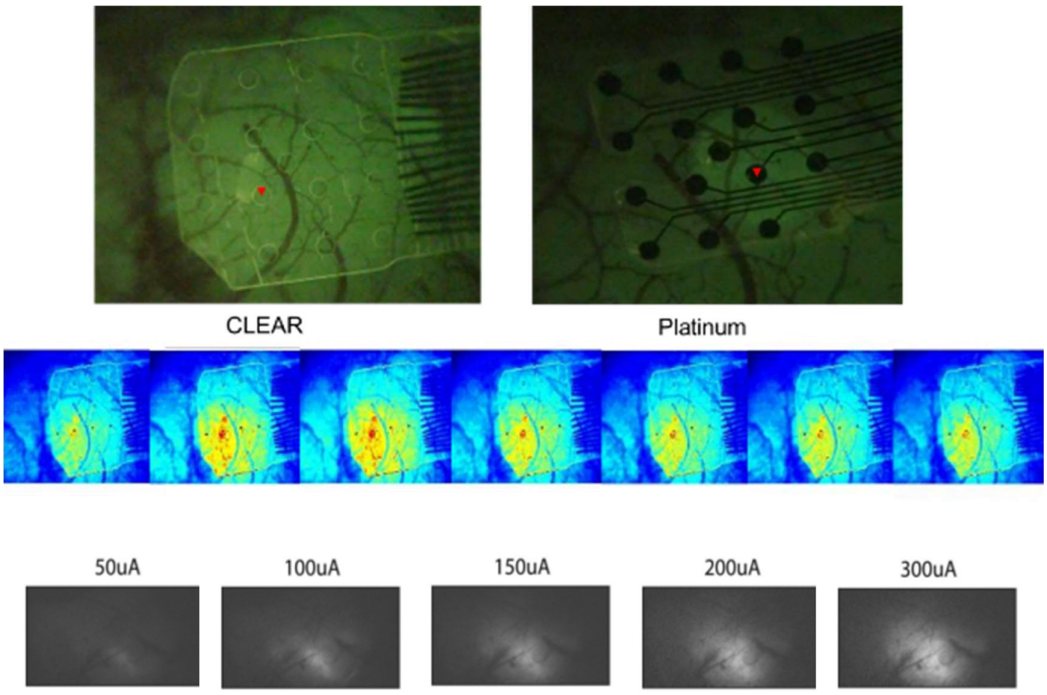

Figure 3.7 Electrical stimulation in a GCaMP6f mouse through CLEAR

Chapter 4. Transparent graphene contact lens electrode array for early diagnosis of eye disease: graphene multi-electrode electroretinography (meERG)

4.1 Introduction

Early diagnosis of eye diseases such as glaucoma and retinitis pigmentosa is critical to treat the diseases quickly and prevent the permanent damage of the retinal cells. The electrical signals from various cell types in retina responding to the light can be used to diagnose the condition of the retinal cells. Previously, metal-based eye sensors have been used to record the electrical signals but the sensing ability has been somewhat limited due to the opaqueness of metal. Graphene could provide unique opportunity to make transparent eye sensors. Recording better eye signals with transparent graphene eye sensors could lead improved ability of early diagnosis of eye diseases. Also, the transparent contact lens eye sensor would be desirable as a wearable device offering better vision. In this chapter, a transparent graphene contact lens array that can record high spatial resolution eye signals with increased intensity is presented. The graphene eye sensor has been successfully implanted in rodents and the signal quality has been systemically analyzed comparing with a conventional metal-based eye sensor. The graphene eye sensor showed better signal quality than the case of metal sensor due to the high transparency of graphene. This fully transparent, implantable graphene contact lens array would prove another promising biological application of graphene.

4.2 Multi-electrode electroretinography (meERG)

Electroretinography (ERG) is the practice which utilizes electrodes placed on the cornea to record the electrical signals from the cells in retina such as cone and rod

photoreceptors, and ganglion cell[95-99]. The ERG signal, the light-induced response of the retina, will be reduced as the retinal cells deteriorate due to a pathology, thus the signal change can be utilized for the early diagnosis. To date the ERG has been clinically performed using metal-based mono-electrode surrounding the edge of the contact-lens of the device (Burian-Allen ERG electrode, ERG-Jet electrode)[100, 101]. Due to the limited spatial resolution of the electrode, multifocal ERG (mfERG), which focuses on different area of the retina, has been required to diagnose localized areas of abnormality[102, 103]. However, the mfERG has some drawbacks such as uncertain correlation to the biological events in retina, relatively longer test time (about 8 minutes per eye), and interpretation required waveforms[102]. Therefore, multi-electrode ERG (meERG) has been proposed to overcome the problem of mfERG and to improve the spatial resolution of the ERG signal.

The first meERG was demonstrated by Sundmark in 1958, but the spatial resolution and reliable recording were limited by unstable fit of the device to the eyes[104, 105]. Recordable signal differences on different location of the cornea were reported by Hennessy and Vaegan in 1995[101]. In 2014, Krakova et al. reported repeatable and reliable meERG measured in rat showing the spatial differences of corneal potential[106]. In spite of the breakthrough of meERG, the material for the meERG electrode have been limited to opaque metals. Conventional neural electrode materials such as gold (Au), iridium (Ir), silicon (Si), and platinum (Pt) has inherent opaqueness which inhibit the light stimulus. The amount of light through the electrode array is important for meERG because the intensity and the resolution of the electrical response from the retinal cells are related to the light induced electrical activity within the retina. Since the meERG electrode array consists of multiple electrode sites and traces, the amplitude of the meERG signal will be reduced when the induced light is blocked by the opaque metal electrode sites and traces. This problem will be worsening when more

electrodes are integrated for better spatial resolution, as more electrode sites and traces will block more incident light. Hence, developing transparent meERG electrode array would solve the problems enabling precise early diagnosis of eye disease.

4.3 Fabrication of graphene meERG

Figure 4.1 shows the concept of graphene contact lens electrode array (or graphene meERG). When the retinal cells receive the light, they convert the optical signal to the electrical signal and deliver them to the brain through optic nerve. At the same time, the sum of the generated electrical signal can be detected from the cornea gathering the information of the functionality of the retinal cells. The cone and rod photoreceptors generate signals contributing to the initial sharp negative polarity as known as a-wave, and the ganglion cells generates signals contributing to the delayed positive polarity as known as b-wave[107, 108]. The spatial difference of the signals can be measured due to the conductance of the cornea (0.42 S/m at 100 Hz) preventing short circuit between electrodes[106].

As depicted in Figure 4.1, the transparent graphene meERG device on the cornea allows the optical stimulation through the transparent electrodes and the recording of meERG signals at the same time. The graphene meERG is composed of mainly two parts: the graphene electrode array on Parylene C substrate and the poly(methyl methacrylate) (PMMA) lens with 25 holes. The graphene array with 25 electrodes was fabricated on flexible and biocompatible Parylene C substrate and it was attached to the PMMA lens aligning each electrode sites and the holes in the PMMA. The holes in PMMA was filled with saline to have electrical continuity between cornea and graphene. The cross section of one graphene electrode site is shown in Figure 4.1. The detailed fabrication method of the graphene electrode array can be found in chapter 2.

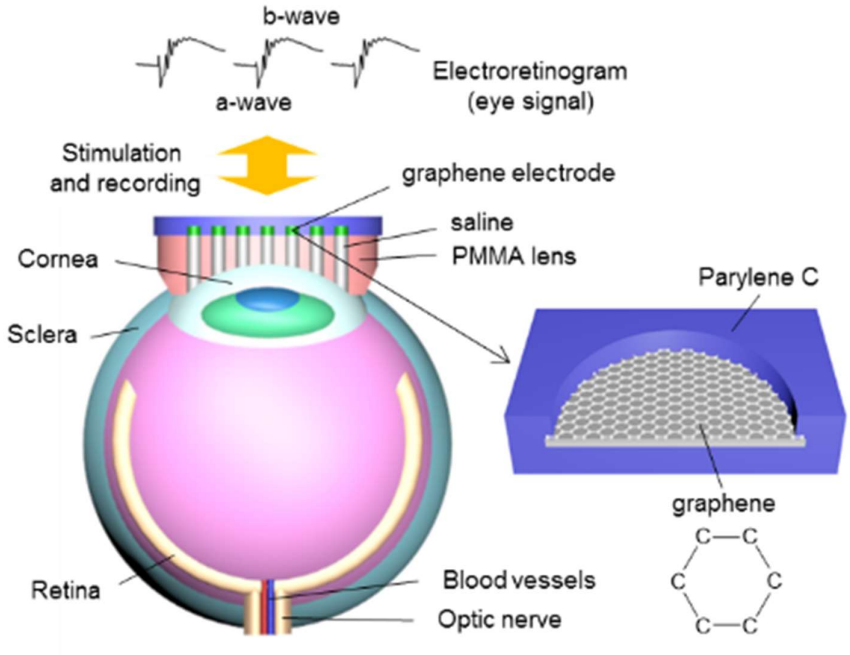

Figure 4.1 Concept of graphene meERG

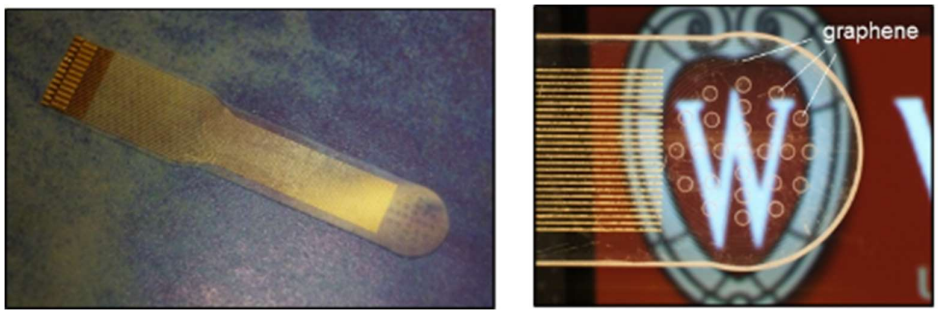

Figure 4.2 Fabricated graphene meERG before assembling with the PMMA lens

Figure 4.2 shows the transparent graphene electrode array before assembling it with the PMMA lens. The patterned graphene was connected to the chromium/gold traces. The metal traces and the pads ensure the connection to the cable and the printed circuit board (PCB) for reliable recording. The diameter of each electrode site is 400 μm. The assembled graphene electrode array and PMMA lens fits to the cornea of Long-Evans rats age-ranging 4-6 weeks.

4.4 Optical property of graphene meERG

Figure 4.3 shows the transmittance of the graphene electrode array and the Pt electrode array as a function of the wavelength. The transmittance was measured through the entire electrode array as shown in the inset of figure 4.3. The average transmittance in visible light range (λ = 390-700 nm) is 91.0 % for the graphene electrode array and 66.5 % for the Pt electrode array. The difference is similar in UV and IR range. This result indicates that the transparent graphene electrode array allows more light stimulation than the metal electrode array that could lead higher neural response from the retinal cells. Furthermore, the light stimulation would be more uniform with the graphene array since the transparent electrode sites and the traces will cause less diffraction compared to the metal array. As shown in figure 4.4, the metal electrode sites and traces occupy large portion of the stimulation area. The light blocking area will be increased as more number of electrodes are integrated for higher resolution in the future. In this case, the advantage of the transparent graphene array will be more prominent. Each electrode sites are named as A1-A12, B1-B8, C1-C4, and M depending on the location. The naming is the same for both graphene and Pt electrodes and will be used for the *in vivo* measurement analysis.

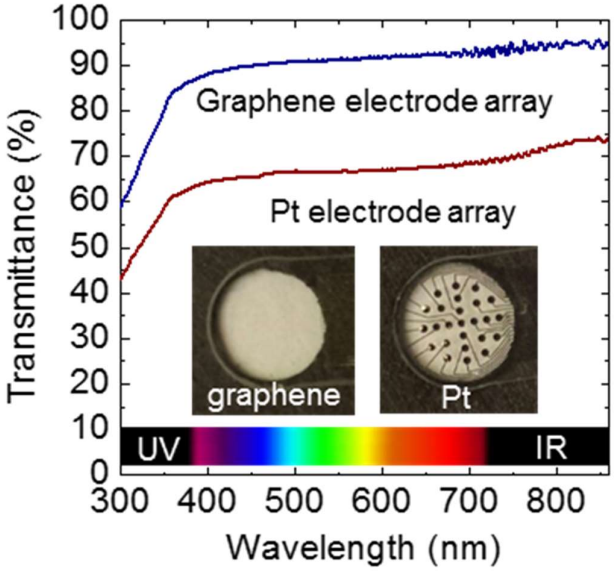

Figure 4.3 Transmittance comparison between graphene and Pt meERG

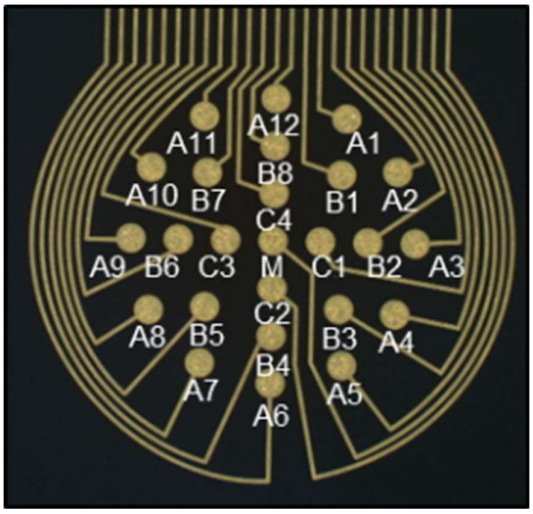

Figure 4.4 Metal meERG and electrode sites numbering

4.5 meERG signal recording

Figure 4.5 shows the first recorded meERG signal with the graphene sensor. The amplitude of the signals is higher than the signals recorded with platinum eye sensor. This is

attributed to the less blockage of the incident light through the graphene sensors. The larger amount of light through the graphene sensor could stimulate the photoreceptors better, which resulted in higher ERG signals. More signal analysis will be followed in the future.

The clear graphene sensor would be desirable for future clinical usage due to their less interference in vision. The device could be developed as wearable contact-lens biosensors with higher transparency.

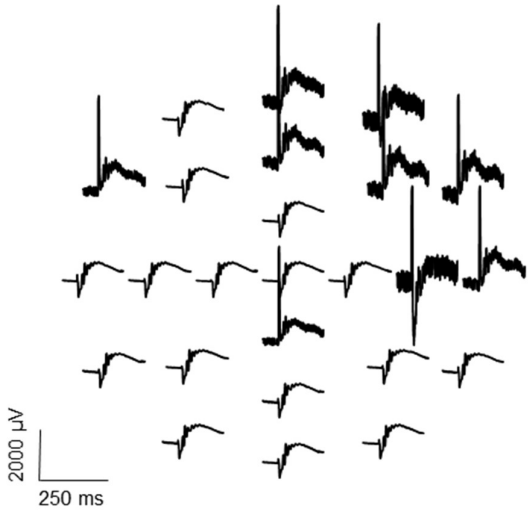

Figure 4.5 Recorded meERG signal with graphene eye sensor

Chapter 5. Graphene field-effect transistors (FETs) with a bottom-gate structure

5.1 Introduction

Bottom-gate graphene field-effect transistors (FETs) have been actively investigated in graphene electronics[109-111]. The bottom-gate structure can be fabricated using a relatively simple process on a highly-doped silicon substrate, which is suitable for fundamental research. Also, the bottom-gate can be made using patterned metal and employed for relatively complicated applications such as graphene RF transistors and circuits. The bottom-gate structure is further divided into two subtypes: bottom-gate coplanar and bottom-gate staggered. The former has graphene on top of the S/D electrodes (Figure 5.1(a)), and the latter has source and drain (S/D) electrodes on top of the graphene (Figure 5.1(b)). As of today, most of the bottom-gate graphene transistors utilize the staggered structure which allows for high performance due to the small contact resistance accomplished by direct metal deposition on the pre-transferred graphene.

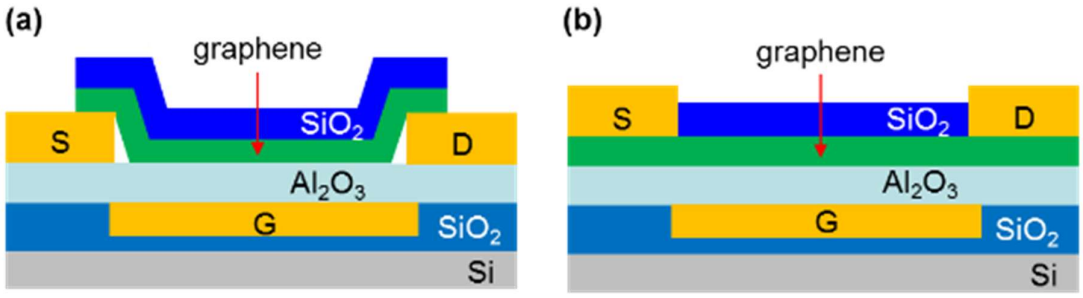

Figure 5.1 Structure of bottom-gate graphene transistors and graphene adhesion on ALD Al_2O_3 (a) Bottom-gate coplanar graphene transistor (b) Bottom-gate staggered graphene transistor

However, the bottom-gate coplanar structure has its own advantages and it can be used in unique applications which utilize the exposed graphene on S/D metal. Transferring graphene after making the bottom gate and source/drain (S/D) allows for the graphene to be subjected to fewer processing steps after it is being transferred onto a substrate. Also, since this structure is compatible to the graphene neural electrode arrays, the bottom-gate coplanar graphene transistors can be integrated in the neural electrode system. For some bio-sensing applications, the increased graphene surface area due to the three-dimensional graphene structure formed on vertical S/D metal and horizontal channel could lead to higher sensitivity[112].

In this chapter, bottom-gate coplanar graphene RF transistors for RF application and future bio application are studied. A method to enhance graphene adhesion on atomic layer deposition (ALD) aluminum oxide (Al_2O_3) in the bottom-gate structure is also presented. Finally, a thermal annealing method is introduced to improve the contact between graphene and S/D metal.

5.2 Graphene radio frequency (RF) transistors with a buried bottom gate structure

Advantages of buried bottom gate structure

As introduced in chapter 1, graphene is rather suited to radio frequency (RF) applications due to the high carrier transport property. Most of the RF transistors have top gate structure which is similar to the conventional silicon-based transistors. However, bottom gate structure is also one of promising candidates for graphene RF transistors. So far, most of bottom gates are used as common gate electrode made by highly doped silicon substrate, which is not appropriate for RF transistors. In this research, separately patterned and buried bottom gate is

used to implement RF transistors. By making buried bottom gate and source/drain (S/D) first followed by graphene stacking (i.e. graphene after source/drain structure), less damaged graphene is expected because graphene undergoes fewer process after being transferred on a substrate. In addition, by making buried gate, more planar surface for gate dielectric can be achieved which is better for step coverage and scaling down of gate dielectric. These advantages can benefit reliability and performance of the device.

Device structure and fabrication process

Scanning Electron Microscope (SEM) image of the fabricated graphene RF transistor is shown in figure 5.2(a) and the device structure is depicted in figure 5.2(b). The buried bottom gate RF transistor is fabricated on oxidized silicon substrate. In order to reduce parasitic capacitance originated from silicon substrate, low doped silicon is used. Buried bottom gate is made by dry etch followed by lift-off process, and e-beam lithography is used for patterning.

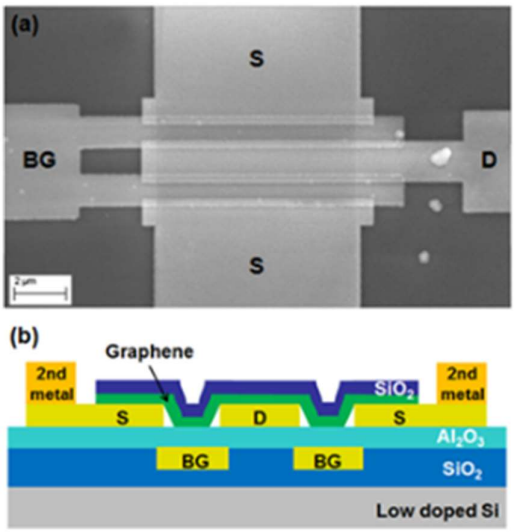

Figure 5.2 Device structure and fabricated graphene RF transistors (a) SEM image of fabricated graphene RF transistor. (b) Structure of buried bottom gate graphene RF transistor.

Atomic layer deposition (ALD) Al_2O_3 with a thickness of 30 nm is used as a gate dielectric. Because of the buried gate structure and conformal deposition property of ALD, the quality of gate dielectric can be as robust as that of conventional top gate structure. The high-k characteristic of Al_2O_3 also benefits the performance of the graphene RF transistors. The source/drain (S/D) electrodes are patterned by e-beam lithography and lift-off process. The Ti/Pd/Au (1/10/50 nm) metal is used for gate and S/D electrodes. Mono-layer graphene made by chemical vapor deposition (CVD) method is transferred to the pre-patterned substrate. According to our experiment, the contact between graphene and pre-patterned S/D electrodes is not strong enough right after transferring, which results in unstable and low drain current. For the purpose of better contact, annealing after graphene transfer is conducted at 300 °C for 15 minutes. The annealing process improves the on-current level and its stability due to the decreased contact resistance between graphene and electrodes. After graphene transfer, SiO_2 protection layer is deposited on graphene and active channel region is patterned by using e-beam lithography and dry etching. Finally, a second metal layer of Ti/Au is patterned by photo-lithography and lift-off for the purpose of reducing series resistance of gate and S/D and increasing RF performance. Typical RF transistor with two finger gate is fabricated. The gate length (Lg=1.1μm) is designed to be longer than the channel length (Lch=600nm) to cover whole channel area for better gate controllability.

DC measurement results

Figure 5.3(a) shows the transfer characteristics of a unit graphene transistor. The gate voltage sweeps from -20 V to 20 V, while the drain voltage is fixed to 0.1 V. The transistor shows PMOS behavior. The on-current, I_{on}/I_{off} ratio, and maximum transconductance (g_m) are 130 μA/μm, 5.31 and 6.85 μS/μm, respectively at V_D=0.1 V. Due to the graphene's zero band

gap nature, the transistor shows relatively high current level for both on and off state. The Ion/Ioff ratio of the device is also low compared to that of conventional silicon transistors, which is generally between 10^3 and 10^6. When the drain bias is increased, the on and off current level is increased, but the on/off current ratio shows similar result. According to our DC measurement results, the two unit transistors in one RF transistor show similar characteristic which is desirable in terms of current balance in a RF transistor. Figure 5.3(b) shows the output characteristics of a unit graphene that the drain current is not saturated well when the gate bias is larger than -10 V. However, as the gate bias is getting lower the drain current tends to be saturated more, which is beneficial for the RF performance, particularly maximum oscillation frequency (f_{max}). The drain current saturation is one of important factors to improve f_{max} because it can be increased by minimizing drain conductance (g_D) attained at channel saturation.

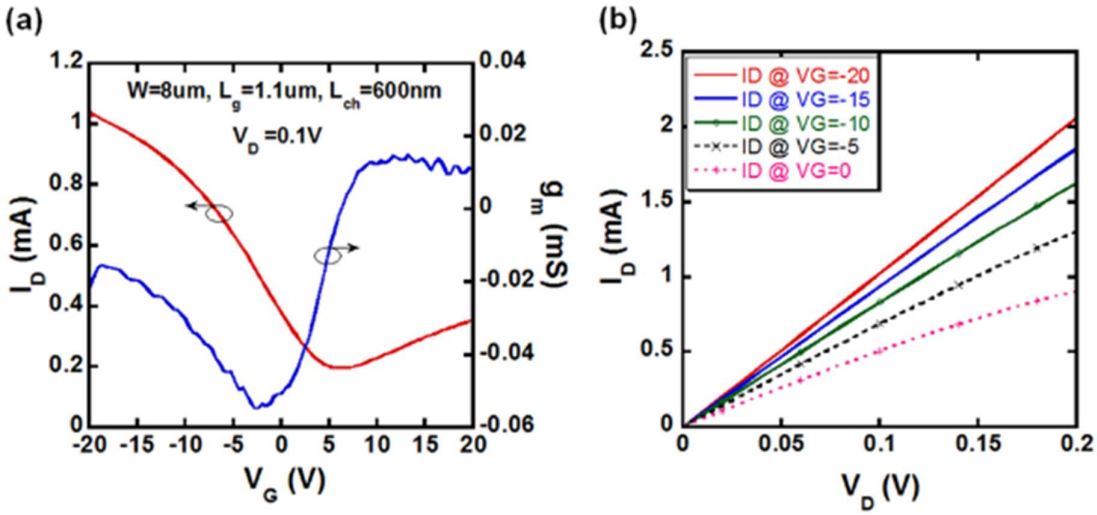

Figure 5.3 DC measurement results of a graphene RF transistor (a) Transfer characteristics and (b) output characteristics of a unit transistor. The on-current, I_{on}/I_{off} ratio, and maximum transconductance are 130 μA/μm, 5.31, and 6.85μS/μm, respectively at V_D = 0.1 V.

RF measurement results

Small-signal scattering (S) parameters were measured at room temperature after SOLT

calibration. The S-parameters were measured at up to 40 GHz using standard ground-signal-ground probes. The plots of magnitude of H_{21} and unilateral gain (U) as a function of frequencies are shown in figure 5.4. The RF transistor was measured at V_{GS} = 2.5 V and V_{DS} = 0.1 V, and the results are plotted after de-embedding to take account of parasitic effects. A cut-off frequency (f_T) of 2 GHz is extracted from the H_{21} plot. A maximum oscillation frequency (f_{max}) of 13 GHz is extracted from the U gain plot with a slope of -20 dB/dec. The higher f_{max} than f_T is attributed to the low source-drain resistance (R_{SD}) due to the fully covered and controllable channel by buried bottom gate. This can be explained by the following equations:

$$f_T = \frac{g_m}{2\pi C_G} \tag{1}$$

$$f_{max} = \frac{f_T}{2\sqrt{(g_D(R_G + R_{SD}) + 2\pi f_T R_G C_G)}} \tag{2}$$

Where C_G is the gate capacitance, g_D is the channel conductance, R_G is the gate resistance and R_{SD} is the source-drain resistance.

From the equation (2), reduced R_{SD} and R_G are beneficial for the higher f_{max}. Since the f_{max} evaluates d power, the larger f_{max} means that the graphene transistors can be used not only for RF switching applications but also for RF amplifiers. Although the RF performance of the fabricated transistor is not superior to up-to-date graphene RF transistors, there is much room for the performance improvement. One method is to scaling-down the channel length to raise drain current level. In this way, higher f_T and f_{max} can be obtained by simply increasing g_m value. Also, reducing gate to source/drain overlap capacitance (C_{gs}, C_{gd}) can help improve RF performance by degrading parasitic effects.

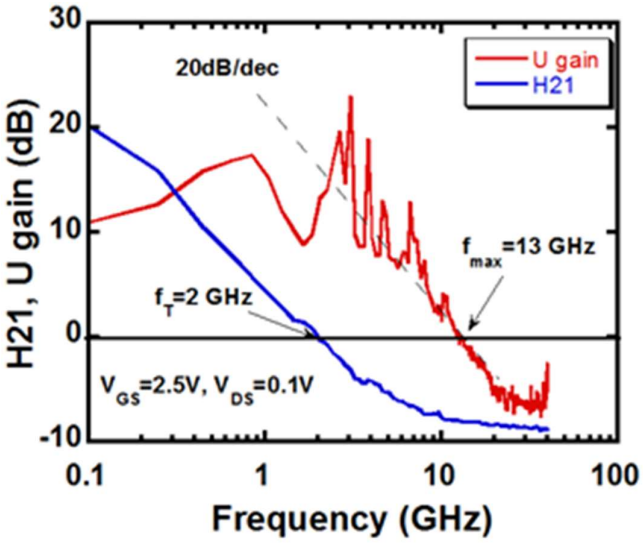

Figure 5.4 Plots of magnitude of H21 and unilateral gain (U) as a function of frequencies. Maximum oscillation frequency (f_{max}) of 13 GHz and cut-off frequency (f_T) of 2 GHz are obtained after de-embedding.

Conclusion

As graphene transistor is getting more interests, various device structures should be investigated for any possible applications. In this study, it is shown that the graphene transistors with buried bottom gate can be used for RF transistors. The RF performance with f_{max} of 13 GHz and f_T of 2 GHz is successfully demonstrated after evaluating DC characteristics. Particularly, the higher f_{max} than f_T, which attributes to reduced $R_{SD,}$ is an advantage of the proposed device structure. Therefore, the graphene RF transistors with buried bottom gate can be one of the promising candidates for both RF switching applications and RF amplifiers.

5.3 Study of graphene adhesion on atomic layer deposition (ALD) Al_2O_3 and its utility to the fabrication of graphene transistors

Motivation

ALD Al_2O_3 has been used as a promising gate dielectric material because of its relatively high dielectric constant (6.5-9, i.e. high-k)[113, 114]. Also, ALD Al_2O_3 is desirable for scaled-down graphene FETs due to its ability to conformally coat and precisely control the film thicknesses[115, 116]. In the top-gate graphene transistor structure, the gate dielectric is deposited on top of the graphene. On the contrary, in the bottom-gate graphene structure, the gate dielectric is located under the graphene which necessitates good adhesion between graphene and ALD Al_2O_3. According to previous studies, a hydrophobic surface is preferable for quality graphene adhesion because graphene itself is chemically inert and hydrophobic[113, 115]. Thus, for improved graphene adhesion on ALD Al_2O_3, a wetting property control method incorporated during ALD Al_2O_3 deposition is proposed and verified. Based on the wetting property control method, graphene transistors with a bottom-gate coplanar structure were fabricated and characterized. The bottom-gate was buried in silicon dioxide (SiO_2) to make a planar surface for the subsequent gate dielectric deposition.

Problem of graphene adhesion on ALD Al_2O_3

To investigate the graphene adhesion on ALD Al_2O_3, graphene on ALD Al_2O_3 was observed using a scanning electron microscopy (SEM, LEO 1530), and the wetting properties of ALD Al_2O_3 and graphene were studied using water contact angle measurement (Optical Contact Angle 15, Dataphysics). Figure 5.5 shows the representative images of poorly attached graphene on ALD Al_2O_3. The SEM image shows agglomerated graphene on the surface. The partially detached graphene is attributed to weak adhesion forces caused by the relatively hydrophilic surface of ALD Al_2O_3 with a water contact angle of 36.5º. It is widely known that pristine graphene is hydrophobic[113, 117-119]. The graphene used in this experiment also shows hydrophobic characteristics with a water contact angle of 68.8º. In general, two different materials that have similar wetting properties have similar surface energy, which is favorable

for mixtures and bonding[113]. The wetting properties of various films can be affected by many factors including growth or deposition conditions, surface treatment, and humidity. Here, a method to control the wetting property of ALD Al_2O_3 by controlling the ALD process condition as well as the time period after deposition has been investigated.

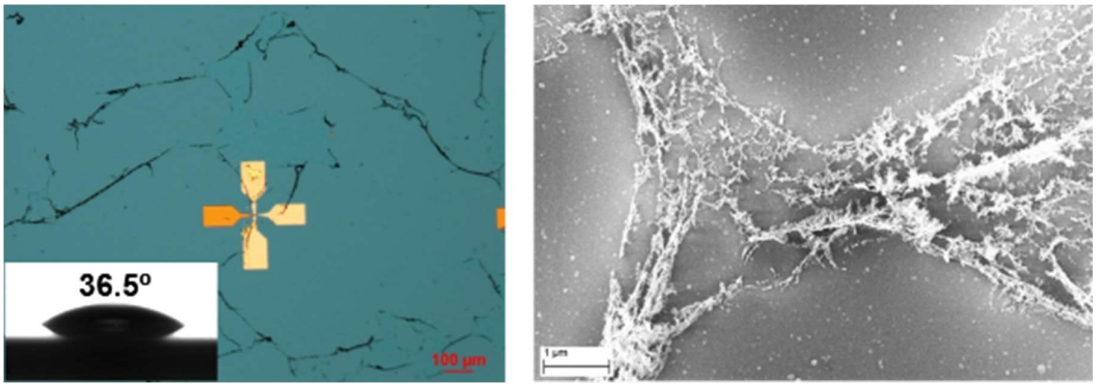

Figure 5.5 Microscope image of poor graphene adhesion on ALD Al_2O_3 (inset) contact angle of the ALD Al_2O_3. SEM image also shows poor graphene adhesion on ALD Al_2O_3

Mechanism of ALD process and a proposed method for wetting property change

The ALD process involves two main chemical reactions as shown in Figure 5.6. In the first reaction (step (A)), trimethylaluminum (TMA, $Al(CH_3)_3$) reacts with the hydroxyl (OH) group, depositing a monolayer of methyl-terminated aluminum[120, 121]. The reaction ceases after all the hydroxyl groups have reacted with the TMA. In the second reaction (step (B)), water vapor reacts with the $AlCH_3$ species, depositing a monolayer of OH groups. The second reaction is terminated after all the methyl groups have reacted with the H_2O. The film thickness is determined by the number of repeated cycles of the reactions. The surface reactions during ALD Al_2O_3 are explicitly written as follows:

(A) $Al\text{-}OH^* + Al(CH_3)_3 \rightarrow Al\text{-}O\text{-}Al(CH_3)_2^* + CH_4$

(B) $AlCH_3^* + H_2O \rightarrow Al\text{-}OH^* + CH_4$

(The asterisk represents the surface-active species.)

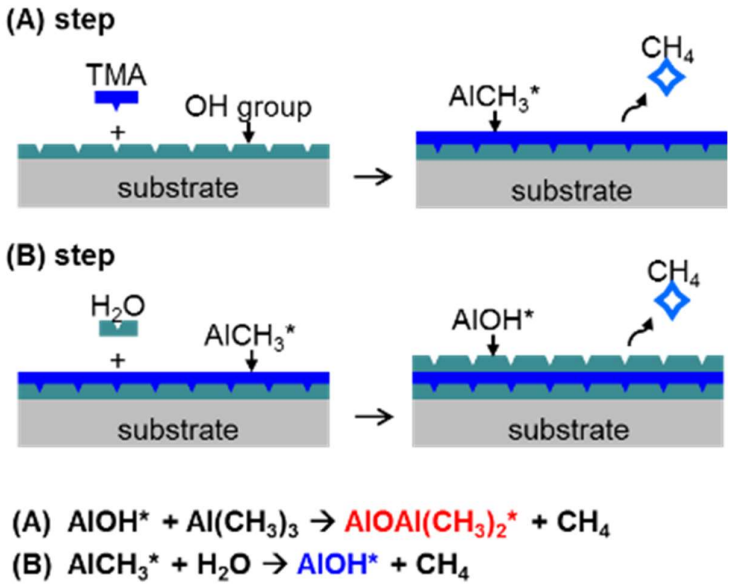

Figure 5.6 Diagram of chemical reactions of ALD Al_2O_3

According to the chemical equations, the final surface chemistry can be controlled by ending the ALD process at step (A) or step (B). If the ALD process stops at step (A), the Al_2O_3 surface is terminated with methyl (CH_3) groups, which makes the surface hydrophobic. On the other hand, if the process is terminated at step (B), the surface is covered with hydroxyl (OH) groups, resulting in a hydrophilic surface. To verify the assumption, two types of samples were prepared for comparison. One ends with five more (A) steps, which is designated as the "CH_3 terminated" sample. The other ends with five more (B) steps, which is designated as the "OH terminated" sample. Each process step was controlled using the software (Labview, National Instruments) in our ALD system. The five more steps for each sample were done to ensure that the surfaces were covered with only one type of species. For both types of ALD Al_2O_3 samples, a thickness of 5 nm was deposited and their contact angles were measured as a function of time

after deposition.

Contact angle measurement results over time

The water contact angles on Al_2O_3 at various times after the ALD process are shown in Figure 5.7. The initial values were measured within 30 minutes after deposition and the changes were monitored for 3 days.

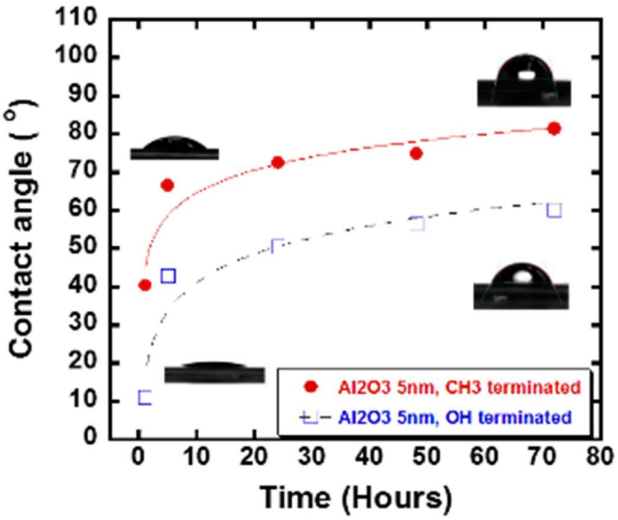

Figure 5.7 Contact angle of ALD Al_2O_3 as a function of time. The filled dots (red color) indicate the CH_3 terminated sample, and the unfilled squares (blue color) indicate OH terminated sample.

The samples were all stored in an ambient atmosphere. For the CH_3 terminated sample depicted by the filled-in dots, the initial contact angle was about 40º and changed to about 80º after three days. On the other side, the OH terminated sample depicted by unfilled squares had an initial contact angle of about 10º and changed to about 60º after three days. These results demonstrate that the wetting property of ALD Al_2O_3 can be controlled by the ALD process as

well as the post-deposition time. According to the results, CH_3 terminated ALD Al_2O_3 is desirable for better graphene adhesion. It is worth noting that both the CH_3 and OH terminated samples experienced a steep rise in contact angles within 5-hours post-deposition. This initial change suggests that waiting for a certain period of time after deposition can be helpful to achieve a relatively hydrophobic surface. The contact angle change may be attributed to the adsorption of contaminants on the surface or surface reorganization resulting from air exposure over time[122, 123].

Fabrication of bottom-gate coplanar graphene transistors

Based on the findings above, graphene transistors with the bottom-gate coplanar structure were fabricated as depicted in Figure 5.8. The patterned bottom-gate electrode was buried in an SiO_2 layer to make a planar surface for the following gate dielectric and graphene transfer processes (Figure 5.8(c))[33]. The CH_3 terminated ALD Al_2O_3 with a thickness of 25 nm was deposited and the source/drain (S/D) electrodes with titanium and gold (Ti/Au=1/60 nm) were formed using e-beam lithography and the lift-off process[33]. The monolayer graphene grown on a copper (Cu) foil via chemical vapor deposition (CVD) was coated with poly(methyl methacrylate) (PMMA) for protection and easy handling. To utilize the graphene on the top side of the Cu foil, graphene grown on the back side of the Cu foil as well as the Cu foil itself were removed using oxygen plasma and ferric chloride ($FeCl_3$), respectively. The PMMA/graphene sheet was transferred onto the pre-processed substrate and dried in nitrogen (N_2) ambient at room temperature (RT) for more than three hours. The sample was kept in a 125 ºC convection oven for 10 minutes to increase the adhesion between graphene and Al_2O_3. For the subsequent process, the PMMA coating was removed with acetone for 20 minutes and the sample was rinsed with DI water for 10 minutes. Finally, the SiO_2 passivation layer was deposited by using an e-beam evaporator and the graphene/SiO_2 active layer was patterned by

dry etching.

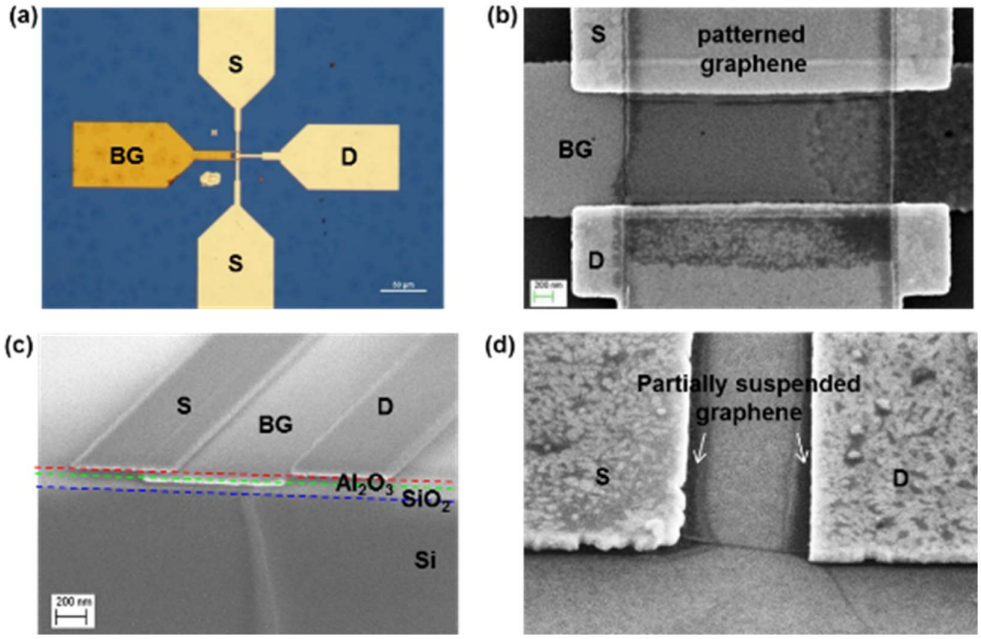

Figure 5.8 Bottom-gate coplanar graphene transistor on ALD Al_2O_3. (a) Microscope image of the graphene transistor after graphene transferred onto the CH_3 terminated ALD Al_2O_3 (b) SEM image after graphene transfer and patterning (c) Cross-section SEM image of the device before graphene transfer (d) SEM image of graphene on the pre-patterned S/D metal. Partially suspended graphene is seen between the channel and the S/D metal.

The detailed graphene transfer method and the characteristics of our CVD graphene including Raman spectrum, sheet resistance, and transparency were previously described in Chapter 2. In this bottom-gate coplanar graphene transistor, the graphene was well-attached onto the CH_3 terminated ALD Al_2O_3 surface (Figure 5.8(a)). Figure 5.8(b) shows the SEM image of the patterned graphene, and Figure 5.8(c) shows a SEM image of the cross-section of the device before the graphene was transferred. It is interesting to note that the graphene was partially suspended near the edge of S/D metal and channel due to the height difference between the channel and the S/D metal (Figure 5.8(d)). This implies that the graphene could be fully suspended if the channel length is scaled down and hence the gap between source and

drain metals is smaller. This may provide additional benefits for the bottom-gate coplanar structure since the suspended graphene may have a possible ballistic transport.[124, 125]

Measurement results

Figures 5.9(a) and (b) illustrate the transfer and output curves of the fabricated graphene transistor with W/L = 3 μm/1.2 μm, respectively. The electrical characteristics were measured using a semiconductor parameter analyzer (HP 4155). The transistor showed a PMOS (P-channel Metal-Oxide-Semiconductor) FET behavior similar to most of the published results on bottom-gate graphene transistors[33, 126, 127]. However, other published work used the staggered structure except Lv et al. who reported a bottom-gate coplanar graphene transistor using HfO_2 gate dielectric[127]. In the bottom-gate coplanar structure, the contact between graphene and pre-patterned S/D metal was not strong enough after graphene transfer resulting in an unstable and low drain current. To achieve better contact, annealing after graphene transfer was conducted at 300 °C for 15 minutes using rapid thermal annealing (RTA). The effect of improved contact was verified by measuring the contact resistance between the graphene and S/D metal using the transmission line method (TLM, also known as transfer length measurement). The TLM pattern with the graphene channel lengths ranging from 10 to 50 μm and the channel width of 100 μm was fabricated. For each length, six samples were measured before and after annealing, and the average values are plotted in Figure 5.9(c). The inset shows the fabricated TLM patterns. Using the TLM theory, the contact resistance (R_C) and sheet resistance (R_S) can be extracted from the total resistance (R_T) versus the channel length (L) plot and the following equation:

$$R_T = \frac{R_S}{W} \times L + 2R_C = slope \times L + 2R_C$$

Where R_T is the measured total resistance, R_C is the contact resistance, R_S is the sheet

resistance, L and W are the length and width of the TLM pattern, respectively.

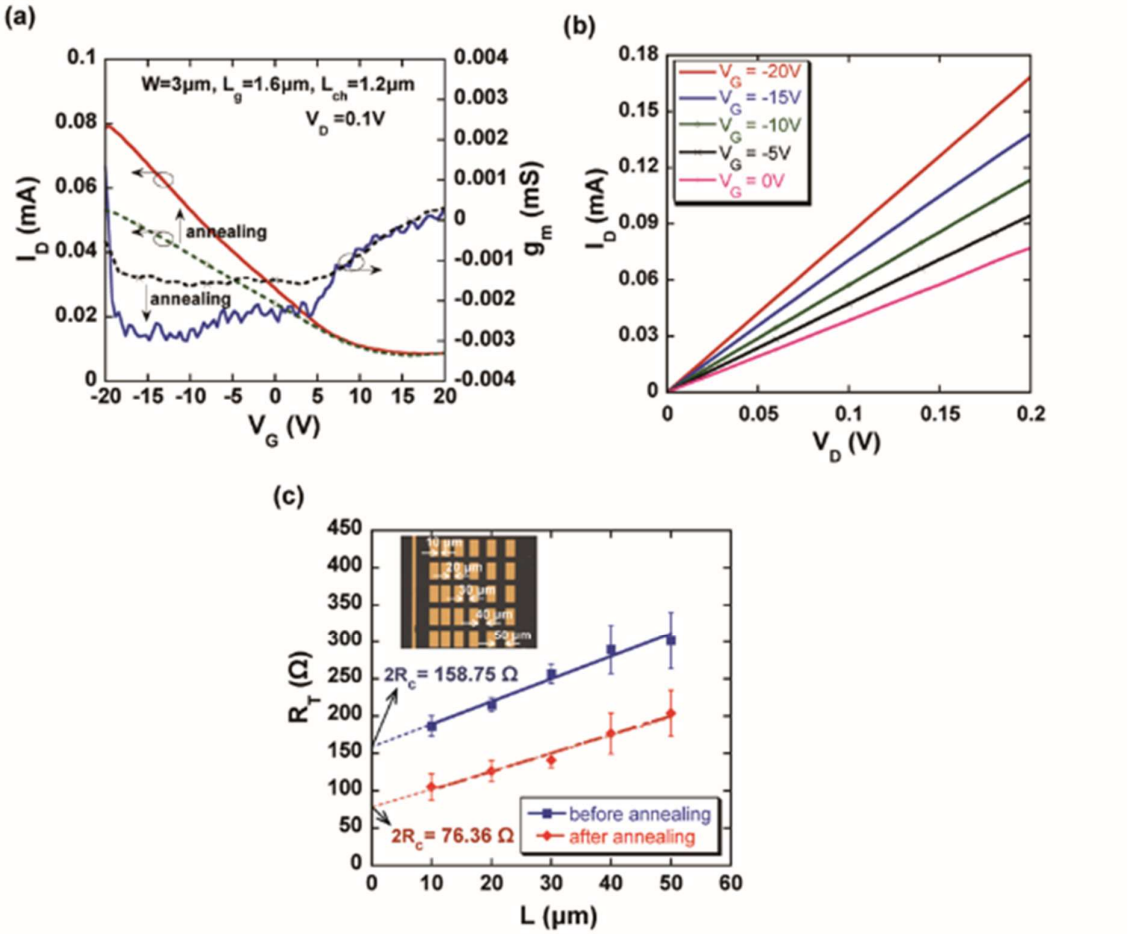

Figure 5.9 Characteristics of the bottom-gate coplanar graphene transistor (a) transfer curves before and after thermal annealing. Both drain current and transconductance are improved after the annealing, (b) output curves with various gate bias from 0 to 20 V. (c) The R_T versus channel length (L) plot measured using the TLM. The R_C is reduced around 48% after the thermal annealing. The inset shows the optical image of the fabricated TLM patterns

It is shown that the contact resistance before and after annealing was ~79.4 Ω and ~38.2 Ω, respectively. Therefore, the contact resistance was reduced around 48 % after the RTA annealing. The annealing process improved the on-current level and its stability due to the

decreased contact resistance between the graphene and the S/D metal. As shown in Figure 5.9(a), the on-current (I_{on}) and maximum transconductance ($g_{m,max}$) were increased 47% and 81%, respectively, after annealing. The average I_{on}/I_{off} ratio, $g_{m,\ max}$, and the field-effect mobility (μ_{FE}) of six devices were 4.04, 20.1 μS at V_D=0.1V, and 249.5 $cm^2/V{\cdot}s$, respectively.

Since graphene has zero band gap, the I_{on}/I_{off} ratio of the device was low compared to that of the conventional silicon transistors. The field-effect mobility was extracted from the equation, $\mu_{FE} = (L_{ch}\times g_m) / (W_{ch}\times C_g\times V_{DS})$. The relatively low mobility may be attributed to several factors including the quality of the as-grown graphene (e.g., the uniformity of the graphene) and process conditions (e.g., the annealing process and PMMA removal). Future efforts in improving the quality of the graphene as well as process optimization should enhance the mobility. The output curves showed conventional PMOS graphene transistor characteristics with limited saturation, which is attributed to zero band gap nature of graphene.[33, 126] The devices show a PMOS-like behavior indicating that the hole transport is more dominant than the electron transport.

Conclusion

The results of this study have demonstrated that the bottom-gate coplanar graphene transistors with ALD Al_2O_3 perform as well as those with a bottom-gate staggered structure. The fabrication method and electrical properties of the device is readily amenable to making RF transistors and biosensors such as pH and protein sensing graphene transistors and liquid-gated sensing applications. The ALD Al_2O_3 wetting property control method developed here can be applied for bottom-gate graphene transistors to improve the graphene adhesion. The bottom-gate coplanar graphene transistors with ALD Al_2O_3 may also be a promising candidate for biological applications by offering an increased graphene area due to its unique structure.

Chapter 6. Flexible graphene transistors on Parylene C substrate

6.1 Introduction

Flexible devices and systems are getting more attractive for various applications such as flexible displays[128-130], wearable electronics[131-133], and biomedical devices[52, 134, 135]. Among various flexible materials, Parylene C has been used as a substrate or a coating material in implantable biomedical devices due to its biostable and biocompatible characteristics[136-138]. Flexible graphene transistors on biocompatible Parylene C substrate would enable active circuitry in implantable biomedical devices. Although Parylene C is a promising flexible material, its vulnerability to high temperature (continuous service temperature: 80 °C) hinders its utility as a flexible substrate. Therefore, an annealing method to improve the performance of a flexible transistor not damaging the flexible substrate is desirable. In this chapter, a fabrication method of a flexible graphene transistor with a bottom-gate coplanar structure on a Parylene C substrate is presented. In addition, a current annealing method and its effect to the device performance have been studied. The localized heat generated by the current annealing method could improve the drain current which is attributed to the decreased contact resistance between graphene and S/D electrodes. A maximum current annealing power in the Parylene C-based graphene transistor has been extracted to provide a guideline for an appropriate current annealing. The low temperature process and the current annealing method presented here would be useful to fabricate two-dimensional materials-based flexible electronics.

6.2 Fabrication of flexible graphene transistors on Parylene C substrate

Figure 6.1 shows the illustration of fabrication process and microscope images of the

flexible graphene transistors. A 15 μm-thick Parylene C film was deposited on a silicon substrate with a size of 2×2 cm^2 using a chemical vapor deposition system (SCS Labcoater2). The silicon substrate was used as a handling substrate during the fabrication process. The size of the substrate can vary depending on the applications. A bottom-gate metal was formed by a lift-off process using photolithography and e-beam metal evaporation. Oxygen plasma treatment (O_2 50 sccm, 10 mTorr, 10 mW, 30 sec) was performed in-between the negative photoresist (PR) 5214 patterning and the e-beam metal evaporation in order to change the wetting property of the Parylene C film from hydrophobic to hydrophilic. The hydrophilic surface can lead stronger metal bonding to Parylene C[52, 139]. Titanium (Ti, 10 nm) and gold (Au, 60 nm) were used for the gate metal. A silicon dioxide (SiO_2) gate dielectric with a thickness of 100 nm was evaporated using an e-beam evaporator which is a low-temperature process. Source and drain electrodes were patterned on the SiO_2 gate dielectric using the same patterning method as the gate metal patterning. In this process, the O_2 plasma treatment was not performed because the S/D metal was deposited on the SiO_2 gate dielectric which was hydrophilic already. Mono-layer graphene synthesized by chemical vapor deposition (CVD) method was transferred onto the pre-patterned S/D metal using a wet transfer method. In specific, the CVD graphene grown on copper (Cu) foil was spin coated with Poly(methyl methacrylate) (PMMA) to protect the exposed graphene on Cu foil. After etching the Cu foil with 0.25 M ferric chloride ($FeCl_3$) and rinsing with deionized (DI) water, the graphene/PMMA film floating on DI water was transferred to the pre-patterned sample. The PMMA was removed by acetone after thoroughly drying out the water in nitrogen atmosphere. Only mono-layer graphene remained on the S/D metal and SiO_2 gate dielectric after this process. Prior to patterning the transferred graphene, a SiO_2 protection layer with a thickness of 30 nm was deposited using an e-beam evaporator. This SiO_2 layer protected the graphene during the

patterning and other post processes. The graphene/SiO_2 layer was patterned using photolithography and dry etching and the patterned graphene worked as a transistor channel. Finally, the graphene transistors on Parylene C was released from the silicon substrate after cutting the Parylene C on the edge of substrate. The Parylene C cutting or patterning can be performed using a cutter or O_2 dry etching. Information on the Parylene C patterning using PR 4620 photolithography and O_2 dry etching can be found in Appendix A1. Parylene C can be released from the silicon substrate in water. The hydrophobic property of the Parylene C makes the entire device be repelled from the water molecules penetrated in-between Parylene C and silicon.

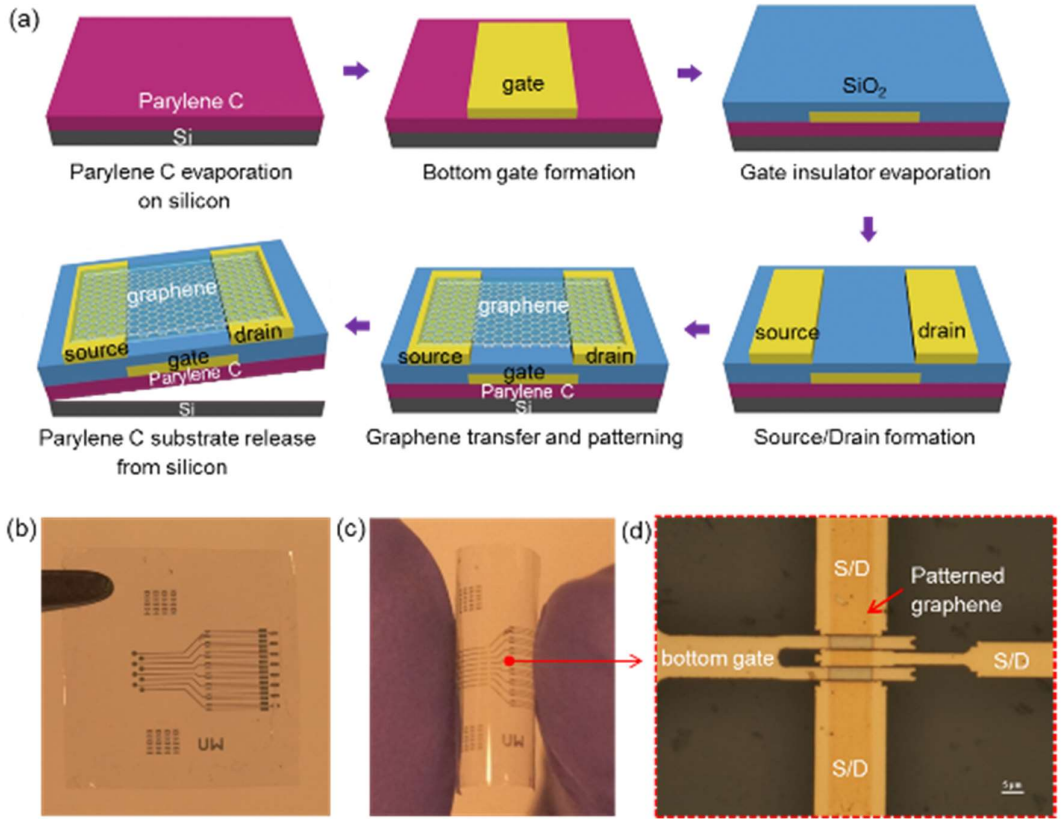

Figure 6.1 Fabrication method and fabricated flexible graphene transistors on Parylene C substrate (a) Schematic illustration of the fabrication process (b) Fabricated flexible graphene transistors on Parylene C substrate (c) Flexible graphene transistors after

bending (d) Microscope image of the flexible graphene transistors. Channel length and width are 3 μm and 10 μm, respectively.

Figure 6.1(b) and (c) show the fabricated flexible graphene transistors on Parylene C substrate. Figure 6.1(d) shows a microscope image of the graphene transistors with two finger gate structure. Patterned graphene is shown on the S/D electrodes and the bottom gate. The channel width (W) and length (L) are 10 μm and 3μm, respectively.

6.3 Performance improvement using a current annealing method

The effect of thermal annealing in graphene transistors has been reported in which the applied heat decreases the contact resistance between graphene and S/D electrodes and reduces the surface contamination of graphene, and thus increase the drain current[6, 59]. On Parylene C substrate, however, the thermal annealing around 100~250 °C could deform or melt the substrate due to the low glass transition temperature of Parylene C ranging from 35 °C to less than 100 °C[140-142]. As an alternative annealing method, a current annealing method was introduced to apply heat directly to the interface of S/D electrodes and graphene diminishing the heat applied to the Parylene C substrate. During the current annealing, electric current flows through the S/D electrodes and the graphene channel which generates Joule heating (Figure 6.2(a)). The generated heat is proportional to the square of the current as shown in the Joule's first law (equation 1).

$$H \propto I^2 \cdot R \cdot t \quad \text{---} \quad \text{equation 1}$$

H: Joule heating, I: current traveling through element, R: resistance of element, t: time

The current annealing method has advantages in terms of the localized heat generation and the controllable heating with an appropriate current level. The localized heat generation

would substantially reduce the heat damage to the Parylene C substrate compared to the thermal annealing that is applying the heat to the entire device.

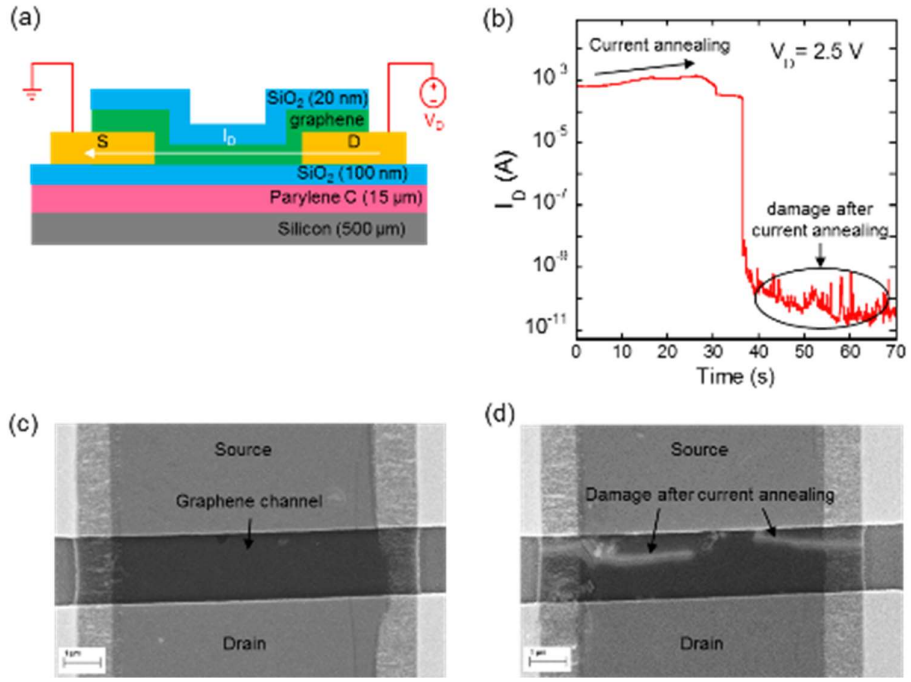

Figure 6.2 Current annealing method and results (a) Schematic illustration of the current annealing method. The annealing current is flowing through source/drain electrode and graphene channel reducing the direct heat to the Parylene C substrate. (b) Representative drain current change over time during the current annealing with the drain voltage of 2.5 V. The initial current increase is attributed to the decrease of contact resistance and the abrupt current drop is attributed to the damage to the graphene. (c) Scanning electron microscopy (SEM) image of the graphene before current annealing. (d) SEM image of the damaged graphene after current annealing.

The representative drain current (I_D) change during the current annealing with the drain voltage (V_D) of 2.5 V is shown in figure 6.2(b). The initial drain current of 0.59 mA was increased to 1.41 mA during the current annealing, which is attributed to the decreased contact resistance between the S/D electrodes and graphene. The drain current was abruptly decreased

after the peak and slight degradation, which may be attributed to the damage on the graphene. In order to investigate the physical damage on graphene, scanning electron microscope (SEM) images of the graphene on the S/D electrodes and the bottom gate were taken before and after the current annealing as shown in figure 6.2(c) and (d). Figure 6.2(d) shows the damaged graphene after the current annealing that could support the abruptly decreased drain current. Similar trends of the drain current and the damaged graphene were observed in other investigated samples as shown in figure 6.3 and 6.4. The detailed trend of drain current change was varying depending on the samples (Figure 6.3). The difference may be attributed to the different initial contact condition between S/D electrodes and graphene, and the different physical damage to the graphene as shown in the SEM images (Figure 6.4). However, all the samples showed the initial drain current increase which verifies the effect of the current annealing on the performance improvement.

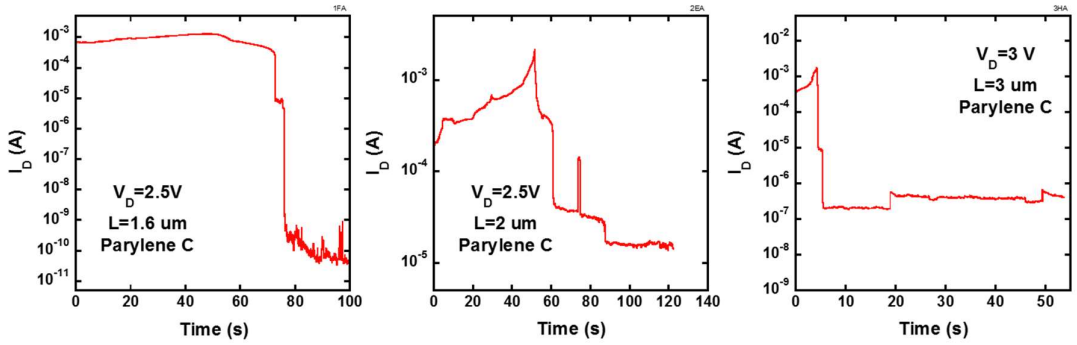

Figure 6.3 Various trends of drain current change during current annealing. The difference is attributed to the different initial contact between source/drain electrodes and graphene, and the different physical damage to the graphene during the annealing.

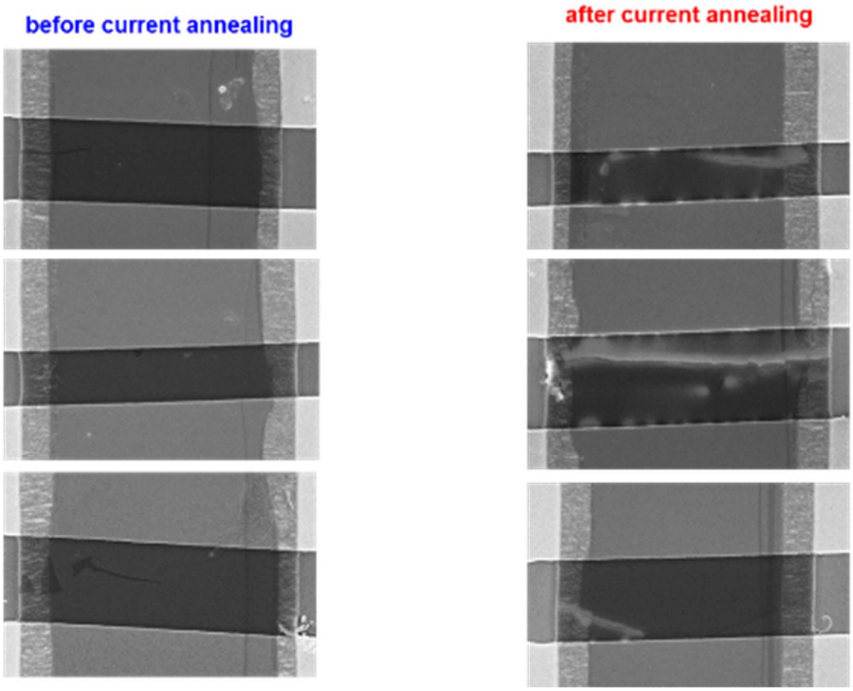

Figure 6.4 SEM images of graphene on channel before and after current annealing. The physical damage appeared to be different for every device. This difference verifies the different drain current changes in each device.

Maximum current annealing power

In order to investigate the optimal annealing current not destroying the device, a maximum current annealing power before the device breakage has been calculated using the equation 2 below.

$$P_{max} = V_D \times I_{D,peak} \quad \text{---} \quad \text{equation 2}$$

P_{max}: Maximum current annealing power, V_D: Drain voltage, $I_{D,peak}$: Peak drain current

Figure 6.5 shows the calculated maximum current annealing power for the device on Parylene C substrate and the device on silicon substrate. The fabrication process and the device dimension of the devices on silicon substrate were the same except the substrate. The maximum

current annealing power of the Parylene C device and the silicon device were calculated as 3.8±1.4 mW and 41.3±20.9 mW, respectively. The result indicates that the Parylene C substrate can allow around ten times smaller current annealing power compared to the silicon substrate in this device structure, which could be anticipated by the lower thermal conductivity of Parylene C than that of silicon[143, 144]. In practical research, the maximum current annealing power can be used to estimate the applying annealing voltage in a device. Typical annealing voltage in our Parylene C devices ranged in 2.5 to 3 V, and the voltage in the silicon devices ranged in 5.5 to 7 V. The calculated maximum current annealing power and the comparison between the two substrates would provide informative guidelines to make Parylene C-based flexible electronics.

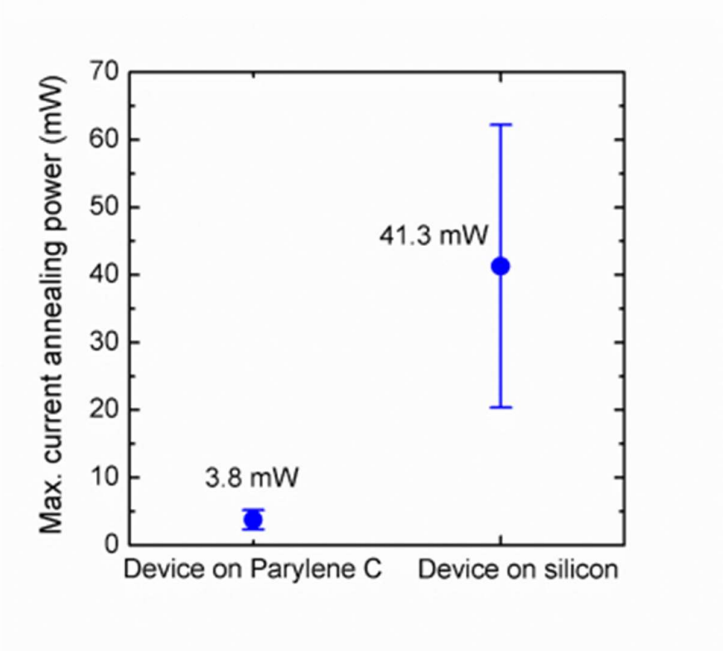

Figure 6.5 Maximum current annealing power allowed to the graphene transistors on Parylene C and silicon substrates. The device on Parylene C could allow around ten times smaller power than the device on silicon.

Measurement results

Figure 6.6(a), (b), and (c) illustrate the representative transfer curves (I_D-V_G), transconductance (g_m) curves, and output curves (I_D-V_D) of a fabricated flexible graphene transistor on Parylene C substrate, respectively. The transistor was annealed with a drain voltage of 2.5 V based on the study of the current annealing method. The electrical characteristics measurement and the current annealing were performed using a semiconductor parameter analyzer, HP 4155. In the transfer curves and the g_m curves, the gate voltage was swept from -4 V to 4 V while varying the drain voltage from 0.1 V to 0.9 V in step of 0.2 V. In general, the graphene transistor showed ambipolar characteristics with electron and hole current on either side of Dirac points around 1 V to 1.5 V. In specific, however, the transistor showed rather PMOS (p-type metal oxide semiconductor) characteristic with the electron-hole asymmetry in which the Dirac points are located at positive gate voltage. It is known that the PMOS-like characteristic is attributed to the adsorbates on graphene such as polymer residues or the oxygen doping during graphene growth and transfer process[145, 146]. The on-current (I_{on}) and the g_m were linearly increased as the drain voltage was increased from 0.1 V to 0.9 V. The $g_{m,max}$, I_{on}, and I_{on}/I_{off} ratio at V_D = 0.9 V were 58.1 μS, 0.165 mA, and 1.76, respectively. The field-effect mobility (μ_{FE}) calculated with the equation 3 was 533.5 $cm^2/V{\cdot}s$.

$$\mu_{FE} = \frac{L_{ch} \times g_{m,max}}{W_{ch} \times C_g \times V_D} \qquad \text{---} \qquad \text{equation 3}$$

μ_{FE}: Field-effect mobility, L_{ch}: Channel length, Wch: Channel width $g_{m,max}$: Maximum transconductance, C_g: gate dielectric capacitance, V_D: drain voltage

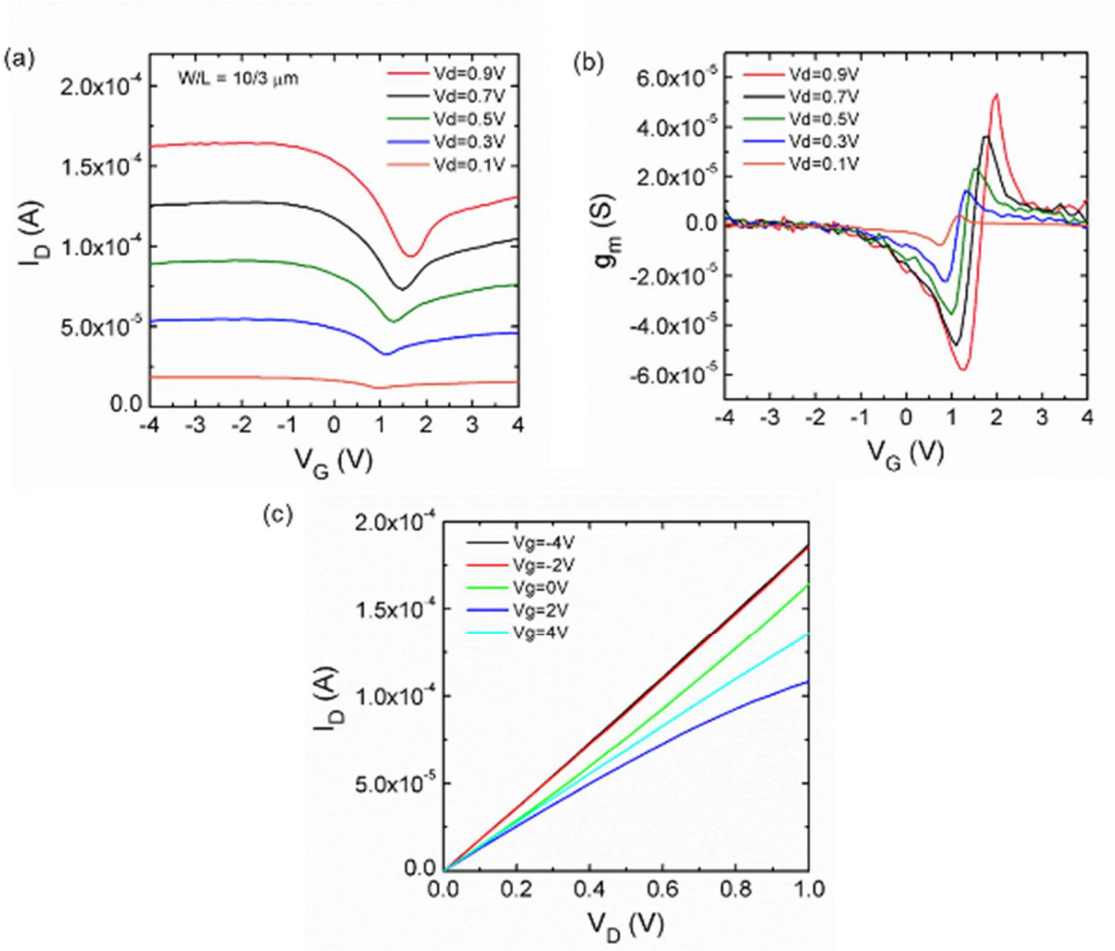

Figure 6.6 Representative electrical measurement results (a) Transfer curves (I_D-V_G) of a fabricated flexible graphene transistor on Parylene C substrate. (b) Transconductance (g_m) curves. The transistor shows PMOS-like behavior with the Dirac points located at positive gate voltage. (c) Output curves (I_D-V_D) with various gate bias from -4 V to 4 V.

For the output curves in figure 6.6(c), the drain voltage was swept from 0 V to 1.0 V while varying the gate voltage from -4 V to 4 V in step of 2 V. The drain current was not saturated well as previously reported in other graphene transistors. This is attributed to the zero bandgap nature of graphene, which results in no depletion regions in the channel. In the ambipolar graphene transistors, a different polarity charge is generated at the drain side rather

than forming a depletion region. The lack of depletion region means there is no decrease of carrier density in the channel near the drain side which leads the current saturation in field-effect transistors. We expect the limitation of non-saturated graphene transistors could be overcome by combining various approaches such as adding low-doped silicon underneath the graphene[147] or shifting Dirac points by drain bias induction[146].

Discussion

In summary, a flexible graphene transistor on Parylene C substrate that can be used as an active device in implantable biomedical devices has been demonstrated. We expect the flexible graphene transistors could be integrated in graphene-based implantable neural electrodes in a monolithic manner to integrate active circuitry into the device. The addition of circuitry would enable making amplified and multiplexed sensors[148]. In addition, the low temperature processes and the current annealing method introduced in this paper would be useful not only for the Parylene C-based graphene transistors but also other flexible devices such as transition metal dichalcogenide monolayers (TMDC)-based transistors[149, 150] and nanomembrane-based electronics[151, 152].

Chapter 7. Conclusions and Future Directions

A transparent, flexible, and implantable graphene neural electrode array and various graphene field-effect transistors have been demonstrated. It is suggested that graphene as an active material in transistors are rather suitable for RF and biological applications due to its zero bandgap nature. The *in vitro* and *in vivo* studies using the graphene neural electrode array showed promising results for various biological studies, including electrophysiology, *in vivo* imaging, optogenetics, and electrical stimulation. The key technical details required to use a graphene-based broad-wavelength transparent neural electrode array would be useful for not only further device development but also various unique *in vivo* studies. It is expected that the unique neural interface device will enable advanced experimentation, and potentially have clinical applications for human patients.

Research directions

Figure 7.1 shows an illustration of the research directions of the CLEAR technology. The research direction for the graphene-based biomedical device could be mainly divided into device development (X-axis) and neurological studies to further understand the underlying mechanism (Y-axis). From the view point of electronics, biomedical devices could be regarded as biocompatible flexible devices. Therefore, building biomedical devices with enhanced functionality in an integrated system on a biocompatible and flexible platform would be beneficial in terms of engineering. Some example functions within the CLEAR technology could be combining light emitting diodes (LEDs), integrating circuits such as amplifiers and RF power suppliers, and adding neurotransmitter sensors. The additional functions will improve the versatility of the CLEAR technology. On one hand, other novel nanomaterials could be employed in the device system. As the advent of graphene explosively expanded the

boundary of biological and electrical applications, other materials such as silicon, germanium nanomembranes, organic materials, and 2D materials (e.g. MoS_2, WSe_2) could be combined in electrodes or active circuitry.

Understanding the underlying mechanism of graphene electrodes would give the opportunity to improve the performance and development of next-generation CLEAR technologies. Further studies on the impedance and the impedance control would be desirable for recording and electrical stimulation. Long-term stability tests are also required both *in vitro* and *in vivo*. Accelerated soak tests in high-temperature saline solution would give long-term stability of the device. Long-term *in vivo* monitoring such as collagen formation in the vicinity of the implanted graphene electrodes and impedance changes would also be valuable. With respect to optical stimulation, in-depth studies of artifacts would be required to understand the origin of the artifact and develop its reduction methods.

The ultimate goal would be to go beyond the device level and conduct research with diverse *in vivo* studies. The CLEAR devices could be implanted in various subjects such as zebrafish, pigs, and non-human primates. Signal acquisition and imaging in different organs such as the eyes, heart, and muscles would be very interesting as well. With the transparent graphene electrodes, unique studies will be available for various neural diseases such as stroke, epilepsy, and Parkinson's disease. Magnetic resonance imaging (MRI) and functional MRI (fMRI) studies could be conducted using the MR transparent graphene electrodes. Correlating between MRI/fMRI and neural recording/stimulation with significantly less artifacts would give researchers more opportunities to understand brain functioning.

Among the abovementioned research directions, some studies have already been conducted. Figure 7.2 shows the concept of LED integration in a CLEAR device. In order to realize the fully integrated transparent GaN LED in the future, commercial LED integration in

Parylene C substrates are being performed. Figure 7.3 shows monkey-sized CLEAR device with larger transparent area (~15 mm in diameter) and dense electrode channels (244 channels). More interesting *in vitro* and *in vivo* studies are expected with CLEAR technology and post-CLEAR technology.

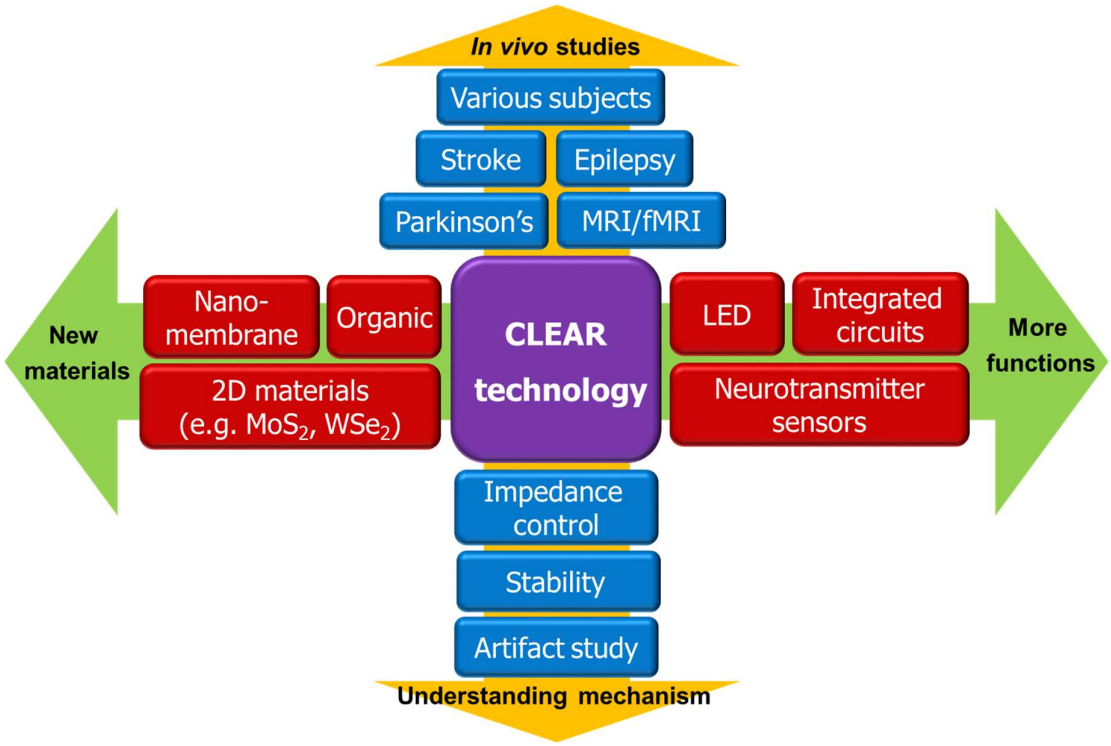

Figure 7.1 Future research directions related to CLEAR technology

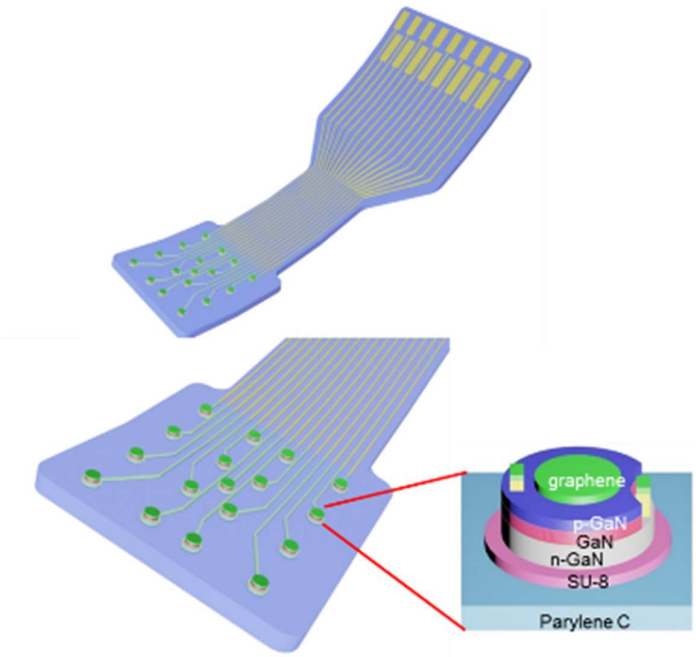

Figure 7.2 Concept of LED integration in CLEAR device

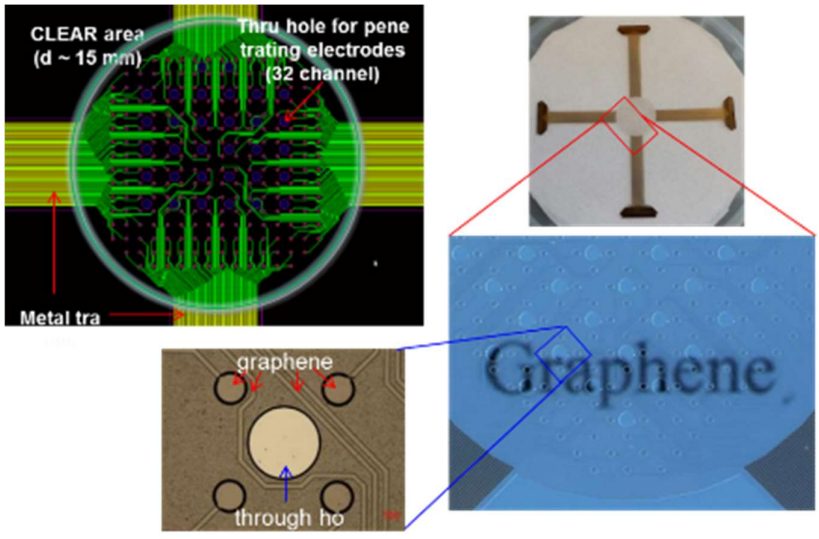

Figure 7.3 Design and fabrication of monkey-size CLEAR μECoG

Appendix

A1. Carbon Layered Electrode Array (CLEAR) device fabrication protocol

A1-1 Materials

REAGENTS

General reagents for multiple parts of the procedure
• Isopropyl alcohol (IPA) (KMG, cat. no. 200440) ! CAUTION IPA is flammable.
• Acetone (KMG, cat. no. 200406) ! CAUTION Acetone is flammable.
• De-ionized (DI) water (Sigma Aldrich cat. no. 38796-1L)
• Wiper (Fisher Scientific, ITW Texwipe, cat. no.18330A)

Fabrication of graphene neural electrode array
• Negative and positive masks appropriate for the desired electrode array (printed film masks (Fineline Imaging, Inc.) attached on glass substrates (Telic Company)
• Silicon wafer for handling substrate (UniversityWafer, any doping type/resistance, 500 μm thick, single side polished)
• Parylene C dimer (Specialty Coating Systems, SCS DPX-C dichloro-di-para-xylylene)
• Mono-layer graphene synthesized by chemical vapor deposition (CVD) method (Commercial graphene is available.)
• AZ 4620 photoresist (AZ Electronic materials)
• AZ-400K developer (AZ Electronic materials)
• S 1813 photoresist (Shipley)
• MIF-321 developer (AZ Electronic materials)
• Gold, Chromium, Titanium (Kurt J. Lesker Company)
• 1:6 Buffered oxide etchant (BOE) (J.T.Baker, cat. no. 1198) ! CAUTION BOE is extremely corrosive. Wear gloves and use eye protection when using BOE.
• 175 μm-thick polyimide (PI) film with adhesive (Dupont, Pryalux LF)
• Board-to-board connector (Hirose, DF30)
• Zero insertion force (ZIF) connector (Hirose, FH26)
• Printed circuit board (PCB) with connectors (Imagineering, Inc. Illinois).

Preparation of CVD graphene
• Copper (Cu) foil (Alfa Aesar, cat. no. 13382)
• Ferric chloride ($FeCl_3$) for Cu foil etch (Fisher Scientific, cat. no. SI115-1)
• Methane (CH_4) (Airgas, cat. no. ME R300DS)
• Hydrogen (H_2) (Airgas, cat. no. HY R300)
• Argon (Ar) (Airgas, cat. no. AR HP300)
• Polymethyl methacrylate (PMMA) (MicroChem)
• Hydrofluoric acid (HF) 49 % for graphene cleaning (J.T.Baker, cat. no. 5824) ! CAUTION HF is extremely corrosive. Wear gloves and use eye protection when using HF.

EQUIPMENT

Fabrication of graphene neural electrode array
• SCS Labcoter 2 Parylene deposition system (Specialty Coating Systems)
• E-beam metal evaporator (CHA Industries, CHA-600) for Cr (chromium), Au (gold), Ti (titanium), etc.
• E-beam dielectric evaporator (Telemark) for silicon dioxide (SiO_2)

• Mask aligner (Karl Suss, MA6/BA6)
• Reactive ion etcher (RIE, Unaxis 790) for oxygen plasma treatment, and Parylene C and graphene etching
• Graphene chemical vapor deposition system (customized system, commercial graphene CVD system is available.)
• Nitrogen (N_2) gun (International Polymer Solutions)
• Ultrasonic cleaning bath (Bransonic, cat. no. CPX5800H)
• Strain meter (Omega engineering, cat. no. DP25-S)
• Digital hot plate (PMC, Dataplate 732 series)

In vitro testing of graphene electrode array

• Raman spectrometer (Horiba LabRAM ARAMIS) for graphene Raman spectroscopy
• Lambda 19 Spectrometer (PerkinElmer) for transmittance measurement

A1-2. Fabrication protocols

Fabrication of graphene neural electrode array ● TIMING 2-3 weeks

1. Clean a 4-inch silicon wafer with Acetone (50 ml) and IPA (50 ml), and dry with nitrogen (N_2) gun for 2 minutes.

▲ **CRITICAL STEP** Depending on the device size and the mask design, wafer size can vary.

2. Deposit the first layer of Parylene C on the wafer (thickness of 15 μm) using a SCS PDS 2010 Labcoater with 25 g of Parylene C dimer.

▲ **CRITICAL STEP** Exact amount of Parylene C dimer should be loaded into the SCS PDS 2010 Labcoater as it determines the thickness of Parylene C film. The thickness of Parylene C can vary depending on the application.

3. Spin coat positive photoresist S 1813 at 4000 rpm for 30 seconds and soft bake the wafer on a hot plate at 115°C for 1 minute.

4. Expose the wafer under i-line UV light (365 nm @ 10 mW) for 12 seconds to form electrode trace and contact pad patterns. Use the negative mask with the electrode trace and pad patterns to mask the UV light when exposing the wafer.

5. Develop the wafer with MIF-321 developer for 1 minute, rinse with DI water for 1 minute, and dry with N_2 gun.

6. Perform oxygen plasma treatment right before metal evaporation for better metal adhesion to Parylene C (O_2 50 sccm, 50 mTorr, 30 W, 30 seconds)

▲ **CRITICAL STEP** The inherent hydrophobic surface of Parylene C needs to be modified to have hydrophilic surface by adding hydroxyl (OH) group. Check the wetting property of the surface by measuring water contact angle if necessary.

7. Evaporate 30 nm of Chromium (Cr) or Titanium (Ti), and 200 nm of Gold (Au) on the patterned wafer with an E-beam evaporator.

▲ **CRITICAL STEP** The deposition should be carried out at vacuum levels of ~10^{-6} Torr or less.

8. Soak the wafer in acetone and sonicate for 5-10 minutes for the metal lift-off process. Rinse with

DI water.

▲ **CRITICAL STEP** Sonicate power should be moderate (~50 W) to prevent the detachment of the metal layers.

9. Perform oxygen (O_2) plasma treatment (O_2 10 sccm, 10 mTorr, 50 W, 30 seconds) to change the entire Parylene C surface from hydrophobic to hydrophilic for a better graphene wet transfer condition.

▲ **CRITICAL STEP** In the graphene wet transfer process, the hydrophilic surfaces allow the graphene sheet to be easily transferred and located at a desirable location on the wafer before the water is dried out. However, note that graphene adhesion is stronger on hydrophobic surfaces because the graphene itself is hydrophobic.

10. ***Wet mono layer graphene transfer*** Synthesize graphene using CVD method. Spin coat PMMA at 4000 rpm for 30 seconds onto graphene on top side of Cu foil to protect the graphene. Soft bake the PMMA/graphene/Cu foil sample on a hot plate at 150 °C for 3 minutes.

11. Etch graphene grown on back side of Cu foil to utilize graphene on top side of Cu foil only. Etch graphene with O_2 10 sccm, 10 mTorr, 50 W for 60 seconds.

12. Etch Cu foil in 0.25 M of $FeCl_3$ solution for 3 hours and rinse the remaining PMMA/graphene stack in deionized (DI) water for 1 hour.

13. (Optional) Put the PMMA/graphene stack in 1:10 HF solution for 1 hour to remove the copper composite residues on the graphene. Rinse the sample in DI water for 1 hour. This step improves the cleanness of CVD grown graphene.

14. Transfer the PMMA/graphene stack to a metal-patterned substrate. The PMMA/graphene should cover the metal traces. Thoroughly dry the sample in N_2 ambient.

▲ **CRITICAL STEP** The location of graphene should be precisely controlled to cover the electrode sites area.

15. Remove PMMA putting the dried sample in acetone and rinse it in DI water.

▲ **CRITICAL STEP** To simply verify the existence of graphene, pour water on the wafer and check the water repellent of graphene as the graphene is hydrophobic.

16. Repeat steps 10-15 to stack 3 more MLG on the wafer (total 4-layer of graphene). Thoroughly dry graphene in N_2 atmosphere for at least 1 hour after stacking each layer to enhance the bonding between graphene layers.

▲ **CRITICAL STEP** The number of graphene layers can be varied. An increase in the number of graphene layers results in lower sheet resistance and lower optical transmittance. The location of graphene should be precisely controlled to overlap the previous graphene layer.

17. Deposit a 30-nm thick layer of SiO_2 using e-beam evaporator to protect graphene.

▲ **CRITICAL STEP** The thickness of SiO_2 can vary but it should ensure graphene is protected and should be enough to withstand the following oxygen plasma etch of Parylene C. Minimum suggested thickness of SiO_2 is 20 nm.

18. Form the entire electrode array patterns (electrode sites, traces, and pads) for SiO_2/graphene etching mask using photolithography. Use the positive mask with the electrode site, trace, and pad patterns to mask UV light when exposing the wafer. The diameter of the electrode sites practically ranges from 100 to 200 μm. Follow steps 3-5 described above for patterning.

19. Etch SiO_2/graphene layers using dry etcher: Etch 30 nm SiO_2 first with CF_4 45 sccm, O_2 5 sccm, 40 mT, 100 W, for 90 seconds. Consecutively, etch graphene with O_2 10 sccm, 10 mTorr, 50 W for 120 seconds. After etching, remove photoresist with acetone, IPA, and N_2 gun.

▲ **CRITICAL STEP** Each SiO_2 and graphene layer should be completely etched to avoid short circuit between electrodes. After step 19, graphene and SiO_2 should remain on the electrode sites, traces, and pads only. The specific etching required will depend on the pattern used.

20. Deposit the second layer of Parylene C (10 μm) by SCS PDS 2010 Labcoater using 16.67 g of Parylene C dimers.

▲ **CRITICAL STEP** It is important that a precise amount of Parylene C dimer is loaded as it determines the thickness of Parylene C film. The thickness of Parylene C can be varied depending on the applications.

21. Spin coat positive photoresist AZ 4620 at 2500 rpm for 30 seconds and soft bake the wafer on a hot plate at 110°C for 3 minutes and 10 seconds. Slowly cool down (around -30 ºC/min) the wafer to ~20 ºC by holding it on a few centimeters above the hot plate for 2 minutes. Repeat the same spin coating procedures to form a 20-μm-thick photoresist.

▲ **CRITICAL STEP** Cooling down slowly can prevent pin holes in the photoresist. Measure the PR thickness to verify if necessary.

22. Expose the wafer under i-line UV light (365 nm @ 10 mW) for 180 seconds to form the etching mask. Only the outline of the device should be patterned. Use the positive mask with the outline patterns to mask the UV light when exposing the wafer.

23. Develop the wafer with AZ-400k developer: H_2O = 1:2 for 1 minute and 30 seconds. Stir well the developer when developing the wafer. Rinse the wafer with DI water for 1 minute, and dry with N_2 gun. Hard bake the wafer on a hot plate at 110°C for 3 minutes.

24. Dry etch half of Parylene C (~13 μm) using O_2 plasma for 48 minutes (O_2 80 sccm, 150 mTorr, 200 W). After etching, remove photoresist with acetone, IPA, and N_2 gun.

▲ **CRITICAL STEP** The etching time can vary depending on the thickness of Parylene C. Longer and stronger etching might cause photoresist and Parylene C overetching.

25. Spin coat positive photoresist AZ 4620 again for the second Parylene C dry etching. Repeat step 21 for the spin coating.

26. Expose the wafer under i-line UV light (365 nm @ 10 mW) for 180 seconds to form the second Parylene C etching mask. The electrode outline, the pads, and the electrode sites should be patterned. Use the positive mask with the outline, site, and pad patterns to mask the UV light when exposing the wafer.

27. Develop the wafer with AZ-400k developer: H_2O = 1:2 for 1 minute and 30 seconds. Stir well the developer when developing the wafer. Rinse the wafer with DI water for 1 minute, and dry with N_2 gun. Hard bake the wafer on a hot plate at 110°C for 3 minutes.

28. Dry-etch the rest of Parylene C using O_2 plasma for 48 minutes (O_2 80 sccm, 150 mTorr, 200 W).

Etch the Parylene C outside of the outline all the way down to the silicon substrate. Etch Parylene C on the electrode sites and pads all the way down to the SiO_2 protection layer. After etching, remove photoresist with acetone, IPA, and N_2 gun.

▲ **CRITICAL STEP** The etching time can vary depending on the thickness of Parylene C. Longer and stronger etching might cause photoresist and Parylene C overetching. Shorter and weaker etching might cause underetching on the pads and electrode sites. Overetching causes an uneven surface of Parylene C which degrades the transparency. Underetching remains residues of Parylene C which can be detected with a microscope image or an increased impedance.

29. Release the device from the silicon wafer by immersing the wafer into water. The hydrophobic bottom surface of Parylene C which repels water molecules helps this releasing process. Dry well with a wiper and N_2 gun.

▲ **CRITICAL STEP** The releasing process could be difficult depending on various situations (sample size, adhesion promotor, etc.). Triggering the releasing process with a tweezer tip from a corner of the device may help.

30. Etch the 30-nm thick SiO_2 protection layer by immersing the device in 6:1 buffered oxide etch (BOE) to expose the stacked graphene. Rinse the device in DI water and dry with N_2 gun.

▲ **CRITICAL STEP** Gently carry the device while wet etching, rinsing, and drying to avoid graphene damage. The wet etching provides good selectivity for the SiO_2 and the graphene.

31. Take Raman spectroscopy on the electrode sites to check the property of graphene. Check the G peak near 1560 cm^{-1} and the 2D peak near 2640 cm^{-1} to verify the quality of graphene.

▲ **CRITICAL STEP** If the quality of the graphene is not adequate, check for the graphene synthesis and each process in steps 10-30.

Assembly of ZIF PCB and the graphene neural electrode, and in vitro testing ● TIMING 1 d

32. Cut a polyimide (PI, 175 μm thick) film with a fine pair of scissors to cover the electrode pad area. Attach the precut PI film to the electrode pad area to secure the connection between the electrode array and the ZIF PCB. The adhesive backing of the PI film should face the electrode pads. Use pressure (235 kPa) and heat (180℃) for 1 hour with a strain meter and a digital hot plate.

33. Insert the graphene electrode array to a ZIF PCB and clip the ZIF PCB to make an electrical contact.

34. Assemble a head cap on the PCB and connect a ground wire and a reference wire to the PCB using a soldering machine.

35. For bilateral study, insert another electrode array to the opposite side of PCB.

36. Seal the connection part of the electrode arrays and ZIF PCB to prevent liquid penetrating. Apply UV curable dental acrylic and cure with UV.

▲ **CRITICAL STEP** Seal the connection part thoroughly. Saline, moisture, or any penetrating liquid or gas could result in short circuit between electrodes. Impedance could be degraded due to the possible erosion for long-term study.

37. Connect the electrode arrays in the ZIF PCB to a potentiostat with a passive connector

38. Perform electrochemical impedance spectroscopy (EIS) and cyclic voltammetry (CV) using the potentiostat[45, 60, 153]. Monitor the EIS and CV changes after implantation.

▲ **CRITICAL STEP** A channel with impedance less than 600 kΩ at 1 kHz is regarded as a live channel. Dramatic changes of EIS (> 2 Mohm) and CV (> -1×10^{-9} A of peak negative current) after implantation might be attributed to the device failure during implantation. An initial impedance increase is attributed to the biological tissue response to the electrodes. The initial increase occurs mostly within the first 7 days of implantation[62].

A2. Neural electrode array implantation surgery protocol

The protocols in appendix A2 is written by Sarah K Brodnick to help the readers understand and utilize the implantation method.

A2-1 Materials

Animals
• Rats (Sprague-Dawley, 8-16 weeks old, Charles River) or mice (Thy1::ChR2/H134R-YFP, 6-16 weeks old, Jackson Lab)

Surgical implantation of graphene electrode array
• Isoflurane (5% induction and 1.5–2.0% in oxygen for maintanence) (Piramal) ! CAUTION Ensure that proper ventilation and gas scavenging methods are in place to prevent potential inhalation of excess isoflurane.
• Povidone iodine scrub (BD E-Z Scrub 205)
• 0.9% Sodium Chloride injection (Hospira)
• Lactated Ringers Injection (Abbott Laboratories)
• Scalpel and #10 scalpel blade (HMD Healthcare)
• Elevator/Double ended micro spatula (Fine Science Tools cat. no. 10091-12)
• Elevator/Combination probe and spatula (Fine Science Tools cat. no. 10090-13)
• Teflon coated Dumont #5 forceps (Fine Science Tools, cat. no. 11626-11)
• Dumont #2 laminectomy forceps (Fine Science Tools, cat. no. 11223-20)
• Rongeurs (Fine Science Tools, cat. no. 16220-14)
• Backhaus towel forceps (Fine Science Tools, cat. no. No. 11095-09)
• Mayo scissors (Fine Science Tools, cat. no. 14010-15
• Iris scissors (Fine Science Tools cat. no. 14090-09)
• Seni-touch sterile gloves (Ansell)
• Sterile surgical gown and towel (Kimberly Clark)
• Surgical drape (Covidien)
• 2×2 gauze (Dynarex)
• Cotton tipped applicators (Dukal Corporation)
• Cellulose eye spears (BVI Ultracell cat. no. 40410)
• Electrocautery (ProAdvantage by NDC)
• Midazolam ! CAUTION Controlled substance, need to obtain DEA and applicable State license before ordering and using.
• Furosemide (Salix, Intervet, INC)
•Buprenorphine hydrochloride (Reckitt Benckiser Healthcare Ltd.) ! CAUTION Controlled substance, need to obtain DEA and applicable State license before ordering and using.

• Dexamethasone (Bimeda-MTC, Animal Health INC)
• Ampicillin (Aurobindo Pharma Limited)
• Antibiotic ointment (Neosporin; Johnson & Johnson)
• Gel-Foam (Pfizer Injectables)
• 3-0 vicryl suture (Ethicon Inc, Johnson & Johnson)
• Fusio and Flow-It dental acrylic (Pentron Clinical, cat. no. N21SB)
• Artificial Tears lubricant ophthalmic ointment (Akorn Animal Health)
• Surgical lubricant (First Priority Inc)
• Lidocaine gel (Akorn Inc)
• Ground and mechanical stability screws and nuts (stainless steel, 0–80 × 1/8 in.) (McMaster Carr cat. no. 91771A052 and 91841A115, respectively)
• #0 tipped autoclavable phillips head screw driver (Steritool cat. no. 11221)
• Drill burr (#105, #106, #107 Dremel, Mount Prospect, IL)
• Round glass coverslips (5mm diameter, 0.15 mm thick rat, 3 mm mouse) (Warner Instruments, Hamden, CT)
• 175 μm-thick polyimide (PI) film with adhesive (Dupont, Pryalux LF) or other plastic sheet with similar thickness
• 50 % dextrose (AgriLabs)
• Fatal PLUS pentobarbitol solution (Vortech Pharmaceuticals) ! CAUTION Controlled substance, need to obtain DEA and applicable State license before ordering and using.
• Masking tape ½" (Scotch)

Equipment

Sterile preparation for implant surgery
• Autoclave
• Bead sterilizer (Steri 250, Inotech)
• Autoclave/Gas sterilization packs (ProAdvantage by NDC)
• Weigh dish (Fisher Scientific cat. no. 08-732-114) and mounting putty (Duck) or ½" masking tape (Scotch) for securing electrode array during sterilization
• Ethylene oxide gas sterilizer ! CAUTION Ethylene oxide sterilizer should vent for an extra 12 hour cycle if contents include plastic that will be implanted within the body

Implantation of graphene electrode array
• Stereotaxic frame and micromanipulator (Leica Biosystems)
• UV Curing light for dental acrylic and safety glasses for UV wavelengths (Radii-cal, SDI)
• Surgical loupes (Orascoptic)
• Hand drill and #56 drill bit (27pc Micro Drill Set with Driver, Titan Tools, ToolDiscounter cat. no. 11003)
• Surgical drill (Micromotor Drill, Leica, Wetzlar, Germany)
• Physiosuite with MouseSTAT and RightTemp pulse oximeter, heart rate monitor and infrared warming pad (Kent Scientific Corporation)
• Surgical microscope (SuperLux 300, Zeiss)
• Isoflurane vaporizer and oxygen flow meter (Smiths Medical, Surgivet)
• F-air isoflurane scavenging canister (Bickford)
• Medical grade oxygen tank and corresponding regulator (Airgas)

A2-2. Device implantation protocols

Sterilize all devices, instruments, and supplies ● TIMING 2 d

1. Secure the graphene electrode array with tape or putty inside two plastic weighing boats with holes, or another gas permeable container to prevent movement of the device which could cause damage to the array.

   ▲ **CRITICAL STEP** Holes should be punched into both top and bottom weigh boats to let gas permeate during ethylene oxide sterilization and for venting of toxic gas at end of sterilization cycle.

2. Pack into secondary pack or drape which can be opened by non-sterile helper during surgery.

3. Run the ethylene oxide sterilizer for a standard 12-hour cycle (plus two hour venting) to allow for enough time for plastic to vent the toxic gas.

4. Sterilize all other supplies and tools that cannot be autoclaved with ethylene oxide gas.

5. Pack into secondary pack or drape that can be opened by non-sterile helper during surgery and autoclave all supplies and tools that can withstand high pressure and heat.

   ▲ **CRITICAL STEP** Everything that will be used in the sterile field of the animal must undergo proper sterilization by autoclave, ethylene oxide gas or bead sterilizer in order to kill any possible pathogen and prevent infection.

CLEAR device implantation surgery (chronic and acute) ● TIMING 2 h

▲ **CRITICAL STEP** **Acute implantation** surgeries under 6 hours do not need to be sterile and Antibiotic (ampicillin) does not need to be given.

6. Weigh animal for drug dosing calculations and place into induction chamber.

7. Turn on isoflurane with attached charcoal scavenger to 5 % for induction. When animal is in a stable surgical anesthetic plane (stage III plane 2), remove from induction chamber and place on a Bain circuit at 2 % isoflurane with 0.8 liters per minute oxygen flow for rats, 0.4 liters per minute oxygen flow for mice**.** The animal is in a stable anesthetic plane when muscle tone is mostly diminished and the pedal and palpebral reflexes are lost. If the animal is not in a deep enough anesthetic plane, the concentration of anesthetic should be increased.

8. Apply eye lubrication ointment to keep eyes from drying.

9. Clip hair in area between ears and from nose to 5 mm behind ears with an electric clipper.

10. Give subcutaneous (SC) injections of dexamethasone (2 mg kg^{-1} for rats, 1 mg kg^{-1} SC for mice), plasmalyte (8 mg kg^{-1} for rats and mice), buprenorphine (0.05 mg kg^{-1} for rats and mice), and ampicillin (50 mg kg^{-1} for rats, 100 mg kg^{-1} SC for mice).

11. Apply lidocaine gel to ear canal with cotton swab and increase isoflurane levels to 2.5 % to prepare for ear bar insertion.

12. Place animal in stereotaxic frame on top of the Physiosuite infrared heat pad set to 38 degrees Celsius. Insert rectal thermometer probe to create closed loop temperature monitoring system and tape to base of tail.

13. Insert ear bars into the ear canals. The animal's head should be secure, and will be able to move up and down, but not side to side. Secure teeth in bite bar. Alternatively, a custom head holder device may be used to immobilize head during drilling in mice.

▲ **CRITICAL STEP** Be very careful not to push too hard and puncture the ear drum. Do apply enough pressure to allow for stable drilling.

14. Turn isoflurane levels down to 1.75 %-2 %, and adjust throughout surgery depending on vital signs such as heart and respiratory rate, and response to reflex tests. If the animal exhibits sign of being in any anesthetic plane lighter than stage III plane 2, such as a positive response to pedal reflex testing (pinching the foot) or palpebral reflex testing (touching the medial or lateral canthus of the eye), isoflurane should be titrated up by 0.5% every few minutes until the animal reaches a stable anesthetic plane. If signs of voluntary movement occur, check tubing connections for leaks and increase isoflurane concentration immediately to 4% until animal is in a stable plane (usually approximately 30 seconds), and then lower to maintenance concentration. If the animal exhibits sign of being in an anesthetic plane deeper than stage III plane 2, such as severely decreased heart and respiratory rate, titrate the concentration of the isoflurane down by increments of 0.5% every few minutes until animal is in a stable plane.

15. Apply Physiosuite pulse ox sensor for SpO2 and heart rate maintenance.

16. Perform surgical scrub of clipped area of the animal's head by alternating IPA and povidone iodine scrub soaked gauze three times in a spiral motion, starting in the center and moving outward.

17. Put on a surgical cap/bouffant and surgical mask. Scrub hands, wrists and forearms with povidone iodine scrub. Put on sterile gloves and gown and prepare drape and surgical supplies

18. Cut a hole in the drape just larger than the intended incision area over the head and apply three towel clamps to adhere drape to skin.

19. Perform a toe pinch to confirm adequate anesthetic plane before incision.

20. Remove top portion of scalp with a scalpel in an ellipse shape using two curvilinear anterior to posterior incisions.

21. Scrape and remove connective tissue and periosteum in areas where acrylic will need to adhere to the skull. If bleeding occurs and does not stop quickly on its own, then apply gentle pressure with a cotton swab or gauze. If bleeding continues apply saline soaked gelfoam with gentle pressure, and perform monopolar or bipolar electrocautery as a final option. If the bone remains moist, apply cautery until dry for proper adhesion of dental acrylic.

22. If space is needed for acrylic placement peripheral to the craniotomies and/or screws, the temporalis and trapezius muscles may need to be elevated or partially resected. Carefully resect the muscle from bone over the lateral ridge and remove approximately 2-3 mm of muscle tissue by cutting with a scalpel blade or using monopolar cautery. Ensure hemostasis by using electrocautery and saline soaked gelfoam.

    ▲ **CRITICAL STEP** Dry the portion of bone over the lateral ridge by applying quick light amounts of monopolar cautery over the entire area. The bone is moist here and will not dry otherwise enough for adhesion of dental acrylic.

23. If the procedure is an acute non-survival, acrylic does not need to be used on the skull as an anchoring point for the devices and ground screws. Instead, the array can be secured by masking tape and positioned by a micromanipulator over the craniotomy.

    ▲ **CRITICAL STEP** If acrylic is not used, the CLEAR device can be recycled for reuse after rinsing with IPA and enzymatic cleaner for acute device implantation, or after the sterilization process described in step 1-5 for chronic device implantation. The array should be retested prior

to reuse to ensure both mechanical and electrical integrity.

24. Implant graphene electrode array in a rat (option A) or a mouse (options B).

(A) Implantation of graphene electrode array in a rat

(i) After skull has been cleared, use a hand drill and #56 drill bit to carefully drill holes in the quadrants anterior to bregma, and posterior to lambda for at least one ground screw, one reference screw, and a third for mechanical stability. Four screws would be recommended for a bilateral implant for stability of the implant. Drill slowly and by half turns until the bit catches, which means you are at the final cortical bone layer. After the bit catches turn one more half turn and pull vertically up and off. A clean hole and visualization of the pulsating dura should remain.

(ii) Place a 0-80 screw into each drilled hole by holding threads with a mosquito hemostat and using a screwdriver with a #0 tip that has been autoclaved.

(iii) Place Fusio dental acrylic on the entirety of the exposed and cleaned skull, leaving areas open for craniotomies and avoiding screws. Let sit for 10 seconds on skull to bond, and apply UV light source for 20 seconds

▲ **CAUTION** Use UV blocking safety glasses to protect eyes from UV light exposure. Test areas of acrylic by poking with pointed forceps and making sure it has a strong bond to the skull. Prolonged exposure of the cortex to UV light can be damaging, and low levels of blue lights may also have differing biological effects[154].

(iv) Using a #105 or #106 drill burr (#105 having a smaller diameter burr), create a ring around the desired unilateral or bilateral craniotomy location through the cancellous (spongy) bone to the inner table of cortical bone where the bone becomes translucent and very thin (approximately 40-80 microns). Often a #106 drill burr can be used to start with, and then switch to #105 with a smaller burr to create deeper ring edges for more precise removal of bone flap. Alternatively use a #107 (larger diameter) drill burr to thin areas where craniotomies will be made down to cortical layer. The advantage of this method is easier removal of a thin layer of bone from the skull that will peel off, and increased visualization of the vasculature and guidance of tool usage.

▲ **CRITICAL STEP** Craniotomy can be made anywhere on the cortex depending on the experiment. Do not drill over the sagittal (midline) suture because of close proximity to the superior sagittal sinus, injury of which could be fatal.

(v) Using rongeurs or laminectomy forceps, remove piece of skull by inserting under the skull and gently elevating. If dural adhesions are present scrape off of bone with elevator or forceps.

(vi) Tape graphene electrode array connector to a micromanipulator and position directly above craniotomy. For placement of array, carefully lift up array with Teflon coated forceps while lowering array onto the dura.

(vii) Place a saline soaked piece of gelfoam on the dura to keep moist.

(viii) Place 5 mm round glass window with pre-applied acrylic on top of graphene array

which is resting on the dural surface. Cover any exposed dura with tiny pieces of saline soaked gelfoam.

(ix) With laminectomy forceps, wrap ground wire around two 0-80 screws and reference wire around third screw (contralateral hemisphere if unilateral so evoked signals are not subtracted during common averaged referencing). Cover screws with dental acrylic**.**

(x) Connect edge of acrylic ridge on window to skull with additional dental acrylic.

▲ **CRITICAL STEP** Do not let dental acrylic seep onto the window since it will occlude imaging area. Also, take care to not let any dental acrylic seep between the window and skull and onto the dural surface.

(xi) Finish by placing acrylic up the array neck. Smooth any rough acrylic edges.

(xii) Two small bolts may be embedded into the acrylic and a piece of polyimide screwed into them to protect the glass window. This will protect the window from damage from animal grooming over it, and helps to keep it clean. This step is optional.

(xiii) Place a purse string suture with 3-0 vicryl in the skin surrounding implant.

(B) Implantation of graphene electrode array in a mouse

(i) If using earbars, follow steps 11-13 for proper lidocaine application and ear bar placement. If using custom head holding device instead of earbars apply superglue or dental acrylic to the bottom of the titanium piece used to secure the head. Be careful not to cover the screw holes, lay on the skull avoiding areas you will be using for craniotomies and the thinned skull ground. Super glue will dry within 5 minutes. If using Fusio dental acrylic, let sit for 10 seconds on skull to bond, and apply UV light source for 20 seconds.

▲ **CAUTION** Use UV blocking safety glasses to protect eyes from UV light exposure. Prolonged exposure of the cortex to UV light can be damaging, and low levels of blue lights may also have differing biological effects[154].

(ii) Once the titanium piece is secure, screw into head holder with two 0-80 screws**.**

(iii) Follow steps in 24(A) describing implantation in rat, but with the following changes.

(iv) Use #105 drill burr instead of #106 and #107 during craniotomy.

(v) Using a #106 drill burr, thin down a portion of skull away from the craniotomies for the ground screw to be placed on.

▲ **CRITICAL STEP** Do not drill too far, as screw may break through skull.

(vi) Place 3 mm round glass window with pre-applied acrylic on top of graphene array that is resting on the dural surface.

(vii) Place ground screw on thinned skull area atop one piece of gelfoam, and cover with small pieces of gel foam.

25. If performing an acute study after experimentation, euthanize the animal at the end by induction with 5 % isoflurane in oxygen and by injection with IC, or IV Fatal-Plus Pentobarbitol (>120 mg kg^{-1}**)** until death is verified by loss of respirations and heartbeat. If performing chronic studies

continue to recover the animal.

26. During the last 5-10 minutes of procedure slowly start turning isoflurane percentage down by 0.25 % every minute until it is at 0 %.

▲ CRITICAL STEP Turning isoflurane off suddenly can cause a rapid change in blood pressure and can cause blood clots to suddenly burst open.

27. Continue to give animal supplemental O_2 at 0.6 L/min through the Bain circuit or 4 L/min into cage until awake and behaving normally (walking around cage, drinking water, grooming).

28. During recovery, place small drops of 50 % dextrose on the gums or tongue to help regulate blood sugar loss during surgery and help speed recovery. Also, give one additional injection of SC plasmalyte for fluids replacement because animals usually will not want to drink water for up to one-hour post-surgery.

29. Offer water first, and slowly introduce food when animal is drinking normally (usually a few hours post-surgery). Smear peanut butter thinly on the cage wall to supplement the diet during the post-surgical period. Make sure animal has accessible water supply.

30. Administer post-surgical medications. Regimen consists of SC injections of buprenorphine (0.05 mg kg^{-1} given 8-12 hours after pre-surgical dose, a half dose (0.025 mg kg^{-1}) 8-12 hours later, and a fourth dose (0.012 mg kg^{-1}) 8-12 hours thereafter), ampicillin SC injections (50 mg kg^{-1} for rats, 100 mg kg^{-1} SC for mice) twice daily for 7 days and topical antibiotic ointment applied to the wound edge twice daily for 7 days.

Bibliography

1. Zhang, Y., et al., *Experimental observation of the quantum Hall effect and Berry's phase in graphene.* Nature, 2005. **438**(7065): p. 201-204.
2. Li, X., et al., *Large-area synthesis of high-quality and uniform graphene films on copper foils.* Science, 2009. **324**(5932): p. 1312-1314.
3. Kim, K.S., et al., *Large-scale pattern growth of graphene films for stretchable transparent electrodes.* Nature, 2009. **457**(7230): p. 706-710.
4. Geim, A.K. and K.S. Novoselov, *The rise of graphene.* Nature materials, 2007. **6**(3): p. 183-191.
5. Bae, S., et al., *Roll-to-roll production of 30-inch graphene films for transparent electrodes.* Nature nanotechnology, 2010. **5**(8): p. 574-578.
6. Cheng, Z., et al., *Toward Intrinsic Graphene Surfaces: A Systematic Study on Thermal Annealing and Wet-Chemical Treatment of SiO2-Supported Graphene Devices.* Nano Letters, 2011. **11**(2): p. 767-771.
7. Novoselov, K., et al., *Two-dimensional gas of massless Dirac fermions in graphene.* nature, 2005. **438**(7065): p. 197-200.
8. Xu, G., et al., *Electrophoretic and field-effect graphene for all-electrical DNA array technology.* Nat Commun, 2014. **5**.
9. Ang, P.K., et al., *Flow sensing of single cell by graphene transistor in a microfluidic channel.* Nano letters, 2011. **11**(12): p. 5240-5246.
10. Hess, L.H., et al., *Graphene transistor arrays for recording action potentials from electrogenic cells.* Advanced Materials, 2011. **23**(43): p. 5045-5049.
11. Kuila, T., et al., *Recent advances in graphene-based biosensors.* Biosensors and Bioelectronics, 2011. **26**(12): p. 4637-4648.
12. Rumyantsev, S., et al., *Selective gas sensing with a single pristine graphene transistor.* Nano letters, 2012. **12**(5): p. 2294-2298.
13. Cooper, D.R., et al., *Experimental review of graphene.* ISRN Condensed Matter Physics, 2012. **2012**.
14. Chen, J.-H., et al., *Intrinsic and extrinsic performance limits of graphene devices on SiO2.* Nature nanotechnology, 2008. **3**(4): p. 206-209.
15. Cai, W., et al., *Thermal transport in suspended and supported monolayer graphene grown by chemical vapor deposition.* Nano letters, 2010. **10**(5): p. 1645-1651.
16. Faugeras, C., et al., *Thermal conductivity of graphene in corbino membrane geometry.* ACS nano, 2010. **4**(4): p. 1889-1892.
17. Xu, X., et al., *Length-dependent thermal conductivity in suspended single-layer graphene.* Nature communications, 2014. **5**.
18. Seol, J.H., et al., *Two-dimensional phonon transport in supported graphene.* Science, 2010.

328(5975): p. 213-216.

19. Wu, J., et al., *Organic solar cells with solution-processed graphene transparent electrodes.* Applied Physics Letters, 2008. **92**(26): p. 263302.
20. Hong, W., et al., *Transparent graphene/PEDOT–PSS composite films as counter electrodes of dye-sensitized solar cells.* Electrochemistry Communications, 2008. **10**(10): p. 1555-1558.
21. Wang, X., L. Zhi, and K. Müllen, *Transparent, conductive graphene electrodes for dye-sensitized solar cells.* Nano letters, 2008. **8**(1): p. 323-327.
22. Liu, Q., et al., *Polymer photovoltaic cells based on solution-processable graphene and P3HT.* Advanced Functional Materials, 2009. **19**(6): p. 894-904.
23. Granqvist, C.G. and A. Hultåker, *Transparent and conducting ITO films: new developments and applications.* Thin solid films, 2002. **411**(1): p. 1-5.
24. Guillen, C. and J. Herrero, *Comparison study of ITO thin films deposited by sputtering at room temperature onto polymer and glass substrates.* Thin solid films, 2005. **480**: p. 129-132.
25. Kwon, K.Y., et al., *Opto-μECoG array: A hybrid neural interface with transparent μECoG electrode array and integrated LEDs for optogenetics.* IEEE transactions on biomedical circuits and systems, 2013. **7**(5): p. 593-600.
26. Ledochowitsch, P., et al. *A transparent μECoG array for simultaneous recording and optogenetic stimulation*. in *2011 Annual International Conference of the IEEE Engineering in Medicine and Biology Society*. 2011. IEEE.
27. Klauk, H., et al., *Ion-beam-deposited ultrathin transparent metal contacts.* Thin Solid Films, 2000. **366**(1): p. 272-278.
28. O'Connor, B., et al., *Transparent and conductive electrodes based on unpatterned, thin metal films.* Applied Physics Letters, 2008. **93**(22): p. 223304.
29. Paetzold, R., et al., *Performance of flexible polymeric light-emitting diodes under bending conditions.* Applied physics letters, 2003. **82**(19): p. 3342-3344.
30. Minami, T., *Substitution of transparent conducting oxide thin films for indium tin oxide transparent electrode applications.* Thin Solid Films, 2008. **516**(7): p. 1314-1321.
31. Noh, H.-s., et al., *Wafer bonding using microwave heating of parylene intermediate layers.* Journal of micromechanics and microengineering, 2004. **14**(4): p. 625.
32. Badmaev, A., et al., *Self-aligned fabrication of graphene RF transistors with T-shaped gate.* ACS nano, 2012. **6**(4): p. 3371-3376.
33. Park, D.-W., et al. *Graphene RF transistors with buried bottom gate*. in *Silicon Monolithic Integrated Circuits in RF Systems (SiRF), 2013 IEEE 13th Topical Meeting on*. 2013.
34. Moon, J., et al., *Epitaxial-graphene RF field-effect transistors on Si-face 6H-SiC substrates.* IEEE Electron Device Letters, 2009. **30**(6): p. 650-652.
35. Lin, Y.-M., et al., *100-GHz transistors from wafer-scale epitaxial graphene.* Science, 2010. **327**(5966): p. 662-662.

36. Wu, Y., et al., *High-frequency, scaled graphene transistors on diamond-like carbon.* Nature, 2011. **472**(7341): p. 74-78.
37. Thongpang, S., et al., *A micro-electrocorticography platform and deployment strategies for chronic BCI applications.* Clinical EEG and neuroscience, 2011. **42**(4): p. 259-265.
38. Williams, J.J., et al., *Differentiating closed-loop cortical intention from rest: building an asynchronous electrocorticographic BCI.* Journal of neural engineering, 2013. **10**(4): p. 046001.
39. Schalk, G., et al., *BCI2000: a general-purpose brain-computer interface (BCI) system.* IEEE Transactions on biomedical engineering, 2004. **51**(6): p. 1034-1043.
40. Millan, J.R. and J. Mouriño, *Asynchronous BCI and local neural classifiers: an overview of the adaptive brain interface project.* IEEE Transactions on Neural Systems and Rehabilitation Engineering, 2003. **11**(2): p. 159-161.
41. Schendel, A.A., et al., *A cranial window imaging method for monitoring vascular growth around chronically implanted micro-ECoG devices.* Journal of neuroscience methods, 2013. **218**(1): p. 121-130.
42. Richner, T.J., et al., *Patterned optogenetic modulation of neurovascular and metabolic signals.* Journal of Cerebral Blood Flow & Metabolism, 2015. **35**(1): p. 140-147.
43. Negi, S., et al., *In vitro comparison of sputtered iridium oxide and platinum-coated neural implantable microelectrode arrays.* Biomedical materials, 2010. **5**(1): p. 015007.
44. Weremfo, A., et al., *Investigating the interfacial properties of electrochemically roughened platinum electrodes for neural stimulation.* Langmuir, 2015. **31**(8): p. 2593-2599.
45. Cogan, S.F., *Neural stimulation and recording electrodes.* Annu. Rev. Biomed. Eng., 2008. **10**: p. 275-309.
46. Polikov, V.S., P.A. Tresco, and W.M. Reichert, *Response of brain tissue to chronically implanted neural electrodes.* Journal of neuroscience methods, 2005. **148**(1): p. 1-18.
47. Ludwig, K.A., et al., *Poly (3, 4-ethylenedioxythiophene)(PEDOT) polymer coatings facilitate smaller neural recording electrodes.* Journal of neural engineering, 2011. **8**(1): p. 014001.
48. Wilks, S.J., et al., *Poly (3, 4-ethylene dioxythiophene)(PEDOT) as a micro-neural interface material for electrostimulation.* Frontiers in neuroengineering, 2009. **2**: p. 7.
49. Ludwig, K.A., et al., *Chronic neural recordings using silicon microelectrode arrays electrochemically deposited with a poly (3, 4-ethylenedioxythiophene)(PEDOT) filmThis work was supported by the Center for Wireless Integrated Microsystems NSF EEC-9986866 and the Whitaker Foundation.* Journal of neural engineering, 2006. **3**(1): p. 59.
50. Lee, C., et al., *Measurement of the elastic properties and intrinsic strength of monolayer graphene.* science, 2008. **321**(5887): p. 385-388.
51. Nair, R.R., et al., *Fine structure constant defines visual transparency of graphene.* Science, 2008. **320**(5881): p. 1308-1308.
52. Park, D.-W., et al., *Graphene-based carbon-layered electrode array technology for neural*

imaging and optogenetic applications. Nature communications, 2014. **5**.

53. Dresselhaus, M.S., et al., *Perspectives on carbon nanotubes and graphene Raman spectroscopy.* Nano letters, 2010. **10**(3): p. 751-758.
54. Malard, L., et al., *Raman spectroscopy in graphene.* Physics Reports, 2009. **473**(5): p. 51-87.
55. Ferrari, A.C., *Raman spectroscopy of graphene and graphite: disorder, electron–phonon coupling, doping and nonadiabatic effects.* Solid state communications, 2007. **143**(1): p. 47-57.
56. Ni, Z.H., et al., *Uniaxial strain on graphene: Raman spectroscopy study and band-gap opening.* ACS nano, 2008. **2**(11): p. 2301-2305.
57. Jakabovič, J., et al., *Preparation and properties of thin parylene layers as the gate dielectrics for organic field effect transistors.* Microelectronics Journal, 2009. **40**(3): p. 595-597.
58. Ferrari, A., et al., *Raman spectrum of graphene and graphene layers.* Physical review letters, 2006. **97**(18): p. 187401.
59. Park, D.-W., et al., *Bottom-gate coplanar graphene transistors with enhanced graphene adhesion on atomic layer deposition Al2O3.* Applied Physics Letters, 2015. **106**(10): p. 102106.
60. Chang, B.-Y. and S.-M. Park, *Electrochemical impedance spectroscopy.* Annual Review of Analytical Chemistry, 2010. **3**: p. 207-229.
61. Yoo, J.-M., et al., *Hybrid laser and reactive ion etching of Parylene-C for deinsulation of a Utah electrode array.* Journal of Micromechanics and Microengineering, 2012. **22**(10): p. 105036.
62. Williams, J.C., et al., *Complex impedance spectroscopy for monitoring tissue responses to inserted neural implants.* Journal of neural engineering, 2007. **4**(4): p. 410.
63. Norlin, P., et al., *A 32-site neural recording probe fabricated by DRIE of SOI substrates.* Journal of Micromechanics and Microengineering, 2002. **12**(4): p. 414.
64. Wilks, S.J., et al., *Voltage biasing, cyclic voltammetry, & electrical impedance spectroscopy for neural interfaces.* JoVE (Journal of Visualized Experiments), 2012(60): p. e3566-e3566.
65. Otto, K.J., M.D. Johnson, and D.R. Kipke, *Voltage pulses change neural interface properties and improve unit recordings with chronically implanted microelectrodes.* IEEE transactions on biomedical engineering, 2006. **53**(2): p. 333-340.
66. Gross, G.W., *Simultaneous single unit recording in vitro with a photoetched laser deinsulated gold multimicroelectrode surface.* IEEE Transactions on Biomedical Engineering, 1979(5): p. 273-279.
67. Yuen, T. and W. Agnew, *Histological evaluation of polyesterimide-insulated gold wires in brain.* Biomaterials, 1995. **16**(12): p. 951-956.
68. Grätzel, M., *Photoelectrochemical cells.* Nature, 2001. **414**(6861): p. 338-344.
69. Honda, K., *Dawn of the evolution of photoelectrochemistry.* Journal of Photochemistry and Photobiology A: Chemistry, 2004. **166**(1): p. 63-68.

70. Han, X., *In vivo application of optogenetics for neural circuit analysis.* ACS chemical neuroscience, 2012. **3**(8): p. 577-584.
71. Cardin, J.A., et al., *Targeted optogenetic stimulation and recording of neurons in vivo using cell-type-specific expression of Channelrhodopsin-2.* Nature protocols, 2010. **5**(2): p. 247-254.
72. Wagenaar, D.A. and S.M. Potter, *Real-time multi-channel stimulus artifact suppression by local curve fitting.* Journal of neuroscience methods, 2002. **120**(2): p. 113-120.
73. Leuthardt, E.C., et al., *A brain–computer interface using electrocorticographic signals in humansThe authors declare that they have no competing financial interests.* Journal of neural engineering, 2004. **1**(2): p. 63.
74. Wilson, J.A., et al., *ECoG factors underlying multimodal control of a brain-computer interface.* IEEE transactions on neural systems and rehabilitation engineering, 2006. **14**(2): p. 246-250.
75. Atry, F., et al., *Monitoring cerebral hemodynamics following optogenetic stimulation via optical coherence tomography.* IEEE Transactions on Biomedical Engineering, 2015. **62**(2): p. 766-773.
76. Makita, S., et al., *Optical coherence angiography.* Optics Express, 2006. **14**(17): p. 7821-7840.
77. Srinivasan, V.J., et al., *Rapid volumetric angiography of cortical microvasculature with optical coherence tomography.* Optics letters, 2010. **35**(1): p. 43-45.
78. Wang, R.K., et al., *Three dimensional optical angiography.* Optics express, 2007. **15**(7): p. 4083-4097.
79. Wang, R.K. and L. An, *Doppler optical micro-angiography for volumetric imaging of vascular perfusion in vivo.* Optics express, 2009. **17**(11): p. 8926-8940.
80. Chen, Z., et al., *Optical Doppler tomographic imaging of fluid flow velocity in highly scattering media.* Optics letters, 1997. **22**(1): p. 64-66.
81. Izatt, J.A., et al., *In vivo bidirectional color Doppler flow imaging of picoliter blood volumes using optical coherence tomography.* Optics letters, 1997. **22**(18): p. 1439-1441.
82. Wojtkowski, M., et al., *In vivo human retinal imaging by Fourier domain optical coherence tomography.* Journal of biomedical optics, 2002. **7**(3): p. 457-463.
83. Wang, H., et al., *High-speed mapping of synaptic connectivity using photostimulation in Channelrhodopsin-2 transgenic mice.* Proceedings of the National Academy of Sciences, 2007. **104**(19): p. 8143-8148.
84. Foutz, T.J., R.L. Arlow, and C.C. McIntyre, *Theoretical principles underlying optical stimulation of a channelrhodopsin-2 positive pyramidal neuron.* Journal of neurophysiology, 2012. **107**(12): p. 3235-3245.
85. Azimipour, M., F. Atry, and R. Pashaie, *Effect of blood vessels on light distribution in optogenetic stimulation of cortex.* Optics letters, 2015. **40**(10): p. 2173-2176.
86. Liu, Y., et al., *OptogenSIM: a 3D Monte Carlo simulation platform for light delivery design in optogenetics.* Biomedical optics express, 2015. **6**(12): p. 4859-4870.

87. Kim, T.-i., et al., *Injectable, cellular-scale optoelectronics with applications for wireless optogenetics.* Science, 2013. **340**(6129): p. 211-216.
88. McCall, J.G., et al., *Fabrication and application of flexible, multimodal light-emitting devices for wireless optogenetics.* Nature protocols, 2013. **8**(12): p. 2413-2428.
89. Sundmark, E., *Recording of the human electroretinogram with the contact glass.* Acta ophthalmologica, 1958. **36**(5): p. 917-928.
90. Steinberg, R.H., *Relation between ganglion cell activity and the local electroretinogram of cat retina.* 1967.
91. Krakova, Y., et al., *Spatial differences in corneal electroretinogram potentials measured in rat with a contact lens electrode array.* Documenta Ophthalmologica, 2014. **129**(3): p. 151-166.
92. Jiang, C., H. Hao, and L. Li, *Artifact properties of carbon nanotube yarn electrode in magnetic resonance imaging.* Journal of neural engineering, 2013. **10**(2): p. 026013.
93. Koch, K., et al., *Magnetic resonance imaging near metal implants.* Journal of Magnetic Resonance Imaging, 2010. **32**(4): p. 773-787.
94. Boas, F.E. and D. Fleischmann, *CT artifacts: causes and reduction techniques.* Imaging in Medicine, 2012. **4**(2): p. 229-240.
95. Steinberg, R.H., *Relation between Ganglion Cell Activity and the Local Electroretinogram of Cat Retina.* Nature, 1967. **216**(5119): p. 1008-1010.
96. Steinberg, R.H., R. Schmidt, and K.T. Brown, *Intracellular Responses to Light from Cat Pigment Epithelium: Origin of the Electroretinogram c-Wave.* Nature, 1970. **227**(5259): p. 728-730.
97. Marmor, M.F., et al., *ISCEV Standard for full-field clinical electroretinography (2008 update).* Documenta Ophthalmologica, 2009. **118**(1): p. 69-77.
98. Rager, G., *The cellular origin of the b-wave in the electroretinogram—a developmental approach.* Journal of Comparative Neurology, 1979. **188**(2): p. 225-244.
99. Selner, A.N., et al. *Novel contact lens electrode array for multi-electrode electroretinography (meERG)*. in *Bioengineering Conference (NEBEC), 2011 IEEE 37th Annual Northeast*. 2011.
100. Esakowitz, L., A. Kriss, and F. Shawkat, *A comparison of flash electroretinograms recorded from Burian Allen, JET, C-glide, gold foil, DTL and skin electrodes.* Eye, 1993. **7**(1): p. 169-171.
101. Hennessy, M. and Vaegan, *Amplitude scaling relationships of Burian-Allen, gold foil and Dawson, Trick and Litzkow electrodes.* Documenta Ophthalmologica, 1995. **89**(3): p. 235-248.
102. Hood, D.C., et al., *ISCEV standard for clinical multifocal electroretinography (mfERG)(2011 edition).* Documenta Ophthalmologica, 2012. **124**(1): p. 1-13.
103. Seeliger, M., et al., *Multifocal electroretinography in retinitis pigmentosa.* American journal of ophthalmology, 1998. **125**(2): p. 214-226.
104. Sundmark, E., *RECORDING OF THE HUMAN ELECTRORETINOGRAM WITH THE CONTACT GLASS.* Acta Ophthalmologica, 1958. **36**(2): p. 273-280.
105. Sundmark, E., *RECORDING OF THE HUMAN ELECTRORETINOGRAM WITH THE CONTACT*

GLASS. Acta Ophthalmologica, 1959. **37**(2): p. 164-171.

106. Krakova, Y., et al., *Spatial differences in corneal electroretinogram potentials measured in rat with a contact lens electrode array.* Documenta Ophthalmologica, 2014. **129**(3): p. 151-166.
107. Hood, D.C. and D.G. Birch, *A quantitative measure of the electrical activity of human rod photoreceptors using electroretinography.* Visual neuroscience, 1990. **5**(04): p. 379-387.
108. Hood, D. and D. Birch, *The a-wave of the human electroretinogram and rod receptor function.* Investigative ophthalmology & visual science, 1990. **31**(10): p. 2070-2081.
109. Park, J., et al., *Single-Gate Bandgap Opening of Bilayer Graphene by Dual Molecular Doping.* Advanced materials, 2012. **24**(3): p. 407-411.
110. Kim, M., et al., *Light-driven reversible modulation of doping in graphene.* Nano letters, 2011. **12**(1): p. 182-187.
111. Lee, J., et al., *Embedded-gate graphene transistors for high-mobility detachable flexible nanoelectronics.* Applied physics letters, 2012. **100**(15): p. 152104.
112. Chen, S., et al., *A graphene field-effect capacitor sensor in electrolyte.* Applied Physics Letters, 2012. **101**(15): p. 154106.
113. Song, S.M. and B.J. Cho, *Investigation of interaction between graphene and dielectrics.* Nanotechnology, 2010. **21**(33): p. 335706.
114. Liao, L., et al., *Single-layer graphene on Al2O3/Si substrate: better contrast and higher performance of graphene transistors.* Nanotechnology, 2009. **21**(1): p. 015705.
115. Lee, B., et al., *Conformal Al2O3 dielectric layer deposited by atomic layer deposition for graphene-based nanoelectronics.* Applied Physics Letters, 2008. **92**(20): p. 203102.
116. Finch, D.S., et al., *Biocompatibility of atomic layer-deposited alumina thin films.* Journal of Biomedical Materials Research Part A, 2008. **87**(1): p. 100-106.
117. Yu, Q., et al., *Graphene segregated on Ni surfaces and transferred to insulators.* Applied Physics Letters, 2008. **93**(11): p. -.
118. Kim, S., et al., *Realization of a high mobility dual-gated graphene field-effect transistor with Al2O3 dielectric.* Applied Physics Letters, 2009. **94**(6): p. -.
119. Lee, B., et al., *Conformal Al[sub 2]O[sub 3] dielectric layer deposited by atomic layer deposition for graphene-based nanoelectronics.* Applied Physics Letters, 2008. **92**(20): p. 203102.
120. George, S.M., *Atomic layer deposition: an overview.* Chemical reviews, 2009. **110**(1): p. 111-131.
121. Herrmann, C.F., et al., *Conformal hydrophobic coatings prepared using atomic layer deposition seed layers and non-chlorinated hydrophobic precursors.* Journal of Micromechanics and Microengineering, 2005. **15**(5): p. 984.
122. Evans, S.D., R. Sharma, and A. Ulman, *Contact angle stability: Reorganization of monolayer surfaces?* Langmuir, 1991. **7**(1): p. 156-161.
123. Lee, K., et al., *Mechanisms for hydrophilic/hydrophobic wetting transitions on cellulose*

cotton fibers coated using Al2O3 atomic layer deposition. Journal of Vacuum Science & Technology A, 2012. **30**(1): p. -.

124. Du, X., et al., *Approaching ballistic transport in suspended graphene.* Nat Nanotechnol, 2008. **3**(8): p. 491-5.
125. Bolotin, K.I., et al., *Temperature-Dependent Transport in Suspended Graphene.* Physical Review Letters, 2008. **101**(9).
126. Lee, J., et al., *Embedded-gate graphene transistors for high-mobility detachable flexible nanoelectronics.* Applied Physics Letters, 2012. **100**(15): p. -.
127. Lv, H., et al., *Inverted process for graphene integrated circuits fabrication.* Nanoscale, 2014. **6**(11): p. 5826-30.
128. Kim, S., et al., *Low-Power Flexible Organic Light-Emitting Diode Display Device.* Advanced Materials, 2011. **23**(31): p. 3511-3516.
129. Mach, P., et al., *Monolithically integrated, flexible display of polymer-dispersed liquid crystal driven by rubber-stamped organic thin-film transistors.* Applied Physics Letters, 2001. **78**(23): p. 3592-3594.
130. Zhou, L., et al., *All-organic active matrix flexible display.* Applied Physics Letters, 2006. **88**(8): p. 083502.
131. Leonov, V. and R.J.M. Vullers, *Wearable electronics self-powered by using human body heat: The state of the art and the perspective.* Journal of Renewable and Sustainable Energy, 2009. **1**(6): p. 062701.
132. Stoppa, M. and A. Chiolerio, *Wearable electronics and smart textiles: a critical review.* Sensors, 2014. **14**(7): p. 11957-11992.
133. Zeng, W., et al., *Fiber-Based Wearable Electronics: A Review of Materials, Fabrication, Devices, and Applications.* Advanced Materials, 2014. **26**(31): p. 5310-5336.
134. Stieglitz, T., M. Schuetter, and K.P. Koch, *Implantable biomedical microsystems for neural prostheses.* IEEE Engineering in Medicine and Biology Magazine, 2005. **24**(5): p. 58-65.
135. Stieglitz, T., *Flexible biomedical microdevices with double-sided electrode arrangements for neural applications.* Sensors and Actuators A: Physical, 2001. **90**(3): p. 203-211.
136. Chang, T.Y., et al., *Cell and protein compatibility of parylene-C surfaces.* Langmuir, 2007. **23**(23): p. 11718-11725.
137. Hsu, J.-M., et al., *Encapsulation of an integrated neural interface device with Parylene C.* Biomedical Engineering, IEEE Transactions on, 2009. **56**(1): p. 23-29.
138. Liu, X., et al., *Metamaterials on parylene thin film substrates: Design, fabrication, and characterization at terahertz frequency.* Applied Physics Letters, 2010. **96**(1): p. 011906.
139. Trantidou, T., T. Prodromakis, and C. Toumazou, *Oxygen plasma induced hydrophilicity of Parylene-C thin films.* Applied Surface Science, 2012. **261**: p. 43-51.
140. Kahouli, A., et al., *Structural and dielectric study of parylene C thin films.* Applied Physics Letters, 2009. **94**(15): p. 152901.

141. Kim, B.J., et al., *Formation of three-dimensional Parylene C structures via thermoforming.* Journal of Micromechanics and Microengineering, 2014. **24**(6): p. 065003.
142. Kahouli, A., et al., *Ac-conductivity and dielectric relaxations above glass transition temperature for parylene-C thin films.* Applied Physics A, 2012. **106**(4): p. 909-913.
143. Noh, H.-s., P.J. Hesketh, and G.C. Frye-Mason, *Parylene gas chromatographic column for rapid thermal cycling.* Journal of Microelectromechanical Systems, 2002. **11**(6): p. 718-725.
144. Shin, Y.S., et al., *PDMS-based micro PCR chip with parylene coating.* Journal of Micromechanics and Microengineering, 2003. **13**(5): p. 768.
145. Wang, X., et al., *N-doping of graphene through electrothermal reactions with ammonia.* Science, 2009. **324**(5928): p. 768-771.
146. Bai, J., et al., *Top-gated CVD Graphene Transistors with Current Saturation.* Nano letters, 2011. **11**(6): p. 2555-2559.
147. Song, S.M., et al., *Improved Drain Current Saturation and Voltage Gain in Graphene–on–Silicon Field Effect Transistors.* Scientific Reports, 2016. **6**: p. 25392.
148. Viventi, J., et al., *Flexible, foldable, actively multiplexed, high-density electrode array for mapping brain activity in vivo.* Nat Neurosci, 2011. **14**(12): p. 1599-1605.
149. Wang, Q.H., et al., *Electronics and optoelectronics of two-dimensional transition metal dichalcogenides.* Nat Nano, 2012. **7**(11): p. 699-712.
150. Lee, G.-H., et al., *Flexible and transparent MoS2 field-effect transistors on hexagonal boron nitride-graphene heterostructures.* ACS nano, 2013. **7**(9): p. 7931-7936.
151. Jung, Y.H., et al., *High-performance green flexible electronics based on biodegradable cellulose nanofibril paper.* Nat Commun, 2015. **6**.
152. Cho, M., et al., *Capacitance-voltage characteristics of Si and Ge nanomembrane based flexible metal-oxide-semiconductor devices under bending conditions.* Applied Physics Letters, 2016. **108**(23): p. 233505.
153. Park, D.-W., et al., *Graphene-based carbon-layered electrode array technology for neural imaging and optogenetic applications.* Nat Commun, 2014. **5**.
154. Cheng, K.P., et al., *Blue Light Modulates Murine Microglial Gene Expression in the Absence of Optogenetic Protein Expression.* Scientific Reports, 2016. **6**: p. 21172.